Laser-plasma interactions from thin tapes for high-energy electron accelerators and seeding compact FELs

by

Brian Henry Shaw

A dissertation submitted in partial satisfaction of the

requirements for the degree of

Doctor of Philosophy

in

Applied Science and Technology

in the

Graduate Division

of the

University of California, Berkeley

Committee in charge:

Dr. Wim P. Leemans, Co-chair
Professor David Attwood, Co-chair
Professor Jonathan Wurtele
Professor Joel Fajans

Fall 2015

Laser-plasma interactions from thin tapes for high-energy electron accelerators and seeding compact FELs

Abstract

Laser-plasma interactions from thin tapes for high-energy electron accelerators and seeding compact FELs

by

Brian Henry Shaw

Doctor of Philosophy in Applied Science and Technology

University of California, Berkeley

Dr. Wim P. Leemans, Co-chair

Professor David Attwood, Co-chair

For over 10 years, laser plasma acceleration (LPA) has been a rapidly growing technology used to create electron beams on length-scales much smaller than that of a conventional RF-accelerator [1]. As electron beam properties improve, research for LPAs is expanding to take advantage of the creation and accessibility of high-quality electron beams from plasma targets. Two applications which are currently being explored are a multi-stage plasma accelerator to reach energies greater than those a single-stage accelerator can achieve and exploring the possibility of an LPA based free-electron laser (FEL) light source. Research supporting both of these efforts has been performed on the 50 TW TREX laser system at the BELLA Center at the Lawrence Berkeley National Lab, and the results of these efforts are described in this dissertation.

Using chirped-pulsed amplification to produce high-quality laser pulses up to petawatt levels, experimental results have yielded laser driven electron beam energies up to 4.25 GeV [2]. By tuning the density of the target, the accelerating gradients sustained by the plasma can grow beyond 100 GeV/m [3] (10^3 times larger than that of a conventional RF accelerator). However, limiting factors such as dephasing of the electron beam from the plasma wake, defocusing of a laser pulse, and energy depletion of the laser into the plasma limit the maximum sensible length of a plasma accelerator. Staging the LPA with two or more accelerating modules could be the next step towards producing beams with energies greater than those possible with a single stage.

One requirement for staged acceleration is that the laser pulse used to drive the first accelerating stage must be coupled out of the beamline, and a fresh laser pulse must be coupled in for the second stage to post accelerate the electrons. To do this while maintaining a short scale length between the two stages requires an optic to be placed near the final focus of the second laser pulse. Because damage will occur when the laser pulse interacts with a steering optic near focus, the coupling optic must be capable of replacing the surface following damage on each successive shot. This thesis comprises a detailed investigation of

the physics of using a plasma mirror (PM) from a tape by reflecting ultrashort pulses from a laser-triggered surface plasma. The tapes used in the characterization of the PM are VHS and computer data storage tape. The tapes are 6.6 μm (computer storage tape) and 15 μm (VHS) thick. Each tape is 0.5 inches wide, and 10s of meters of tape are spooled using a tape drive; providing thousands of shots on a single reel of tape. The amount of reflected energy of the PM was studied for different input intensities. The fluence was varied by translating the focus of the laser upstream and downstream of the tape, which changed the spot size on the tape surface and hence changed the fluence. This study measured reflectances from both sides of the two tapes, and for input light of both s and p-polarizations. Lastly, an analytic model was developed to understand the reflectance as a function of fluence for each tape material and polarization.

Another application that benefits from the advancements of LPA technology is an LPA-based FEL. By sending a high quality electron bunch through an undulator (a periodic structure of positive and negative magnetic poles), the electrons oscillate transversely to the propagation axis and produce radiation. The 1.5 m THUNDER undulator [4] at the BELLA Center has been commissioned using electron beams of 400MeV beams with broad energy spread (35%) [5]. To produce a coherent LPA-based FEL, the beam quality would need to improve to sub-percent level energy spread. A seed source could be used to help induce bunching of the electron beam within the undulator.

This thesis described the experimental investigation of the physics of using solid-based surface high-harmonic generation (SHHG) from a thin tape as a possible seed source for an FEL. A thin tape placed within centimeters of the undulator's entrance could act as a harmonic generating source, while simultaneously transmitting an electron beam. This removes the need for transport optics for the XUV photons and the need for additional optics to overlap the seed beam with the electron beam at the undulator entrance.

By operating at sub-relativistic laser strengths, harmonics up to the 17^{th} order of 800 nm light are produced using an SHHG technique known as coherent wake emission (CWE). CWE pulse properties such as divergence, energy, conversion efficiency, and spectrum are measured for a wide range of tape materials and drive laser conditions. A clear correlation between surface roughness and harmonic beam divergence is found. The measured pulse properties for the 15^{th} harmonic from VHS tape (conversion efficiency $\sim 6.5 \times 10^{-7}$ and an rms divergence of 12 mrad), the 100 mJ-level, 40-50 fs-class drive laser, produces peak powers of several MW's of XUV pulses. The results of a 1D model indicate that these CWE pulses with MW level powers are sufficient for seed-induced FEL gain.

To my family (past, present, and future). Thank you for the endless love and support. My confidence, character and work ethic has come from those family members I've been with up until now, and my motivation to succeed stem from the future family members I will grow old with. My wife **Krystal Shaw**, your support has kept me going. Without you I could not have achieved so much. My most important roles in this world, are the role I took on July 22, 2011 and August 4, 2014, and I will keep them as my top priority the rest of my life.

Also **to all the teachers** (especially those who have taught me along the way) who have gone the extra mile to educate and encourage the imagination and creativity of their students. Without teachers, no white-collar jobs would exist. This can't be said for any other profession, and teachers are too often taken for granted for the amazing work they do.

Lastly, to my hero, **to my grandfather,** Lawrence Worth Shaw. Few kids have a legendary community member as a grandparent. My brother and I were fortunate enough to have that privileged.

"If it were easy, everyone would be doing it."

I'm so happy you were here to see me start my Ph.D. at Cal. I miss you.

Contents

List of Figures

List of Tables

Acknowledgments

To acknowledge everyone who I would like to would fill the 100+ pages of my thesis. So I apologize ahead of time to those who have help in my success, but may have been left out of this section. Thank you for your help, and I am grateful for the positive effects you've had on my life.

Krystal: You will never understand how much you mean to me. Without your love and support, I couldn't have made it through my time at Cal. You are an amazing wife, an incredible mother, and I hope I make you as happy as you make me. Everything I do is for you and Peyton (and any future children). Nothing is more motivating than knowing I have someone like you in my corner through thick and thin, for better or worse, for richer or poorer, as long as we both shall live.

My family: Anyone who knows me well knows I would do anything for my family. I have a large family and look forward to any event with the Shaw or Cesa or Coupe family members in attendance. I thank everyone in these bloodlines for helping shape my childhood and young adult life. My parents have given me everything. From giving me life, to supporting me as a child, an athlete and a student, I now know (being a parent myself) how great of a job my parents did. I hope that I can give my children as much love and support as you gave me. Thank you both so much! My grandfather was, still is, and always will be my hero, and I'm grateful for every minute I spent with him, and every phone conversation we shared. Nearly every time I've faced a monumental task in my life, I've thought of my grandfather and did what I thought he would do, and did what I thought would make him proud. Until my daughter was born, my wedding day was the best day of my life, and I will always remember that event began with my grandpa and grandma walking down the isle; two people who I love and respect more than anything. My best man that day was my brother, and I've always been my brothers biggest fan. Being the best man at his wedding was one of the greatest honors I've been given. And having Clark, Lauren and Autumn at my Cal commencement meant a lot to me. Also having Krystal's parent's in attendance meant a lot to me. Bill and Kim have done so much for me; they've accepted me into their family, encouraged me, and have given me the most amazing wife in the world. I'm lucky and grateful to have these people in my life.

Wim: First and foremost, the ability to do research at the Lawrence Berkeley National Lab, and to stay close to the family and friends was made possible by Wim Leemans. Whatever Wim saw in me in our first meeting, call it potential, call it ambition, or maybe just a 6' 6" lab hand to reach into the hard to reach spaces; none of this would have been possible without the financial support and advisement of Wim. Wim has taught me many things about work in a laboratory, we have shared many very honest and open discussions during my time in graduate school, and I have learned a tremendous amount in my time under his advisement.

Jeroen: Jereon was the man behind the scenes who dealt with me for 5 years. The man who took on an ambition young Ph.D. student, and helped mold a first class AS&T graduate. The man who thought it was a good idea to take me half way around the world with him,

to study harmonics and sip wine next to the setting sun behind the Eiffel Tower. Frankly, Jeroen is the reason I know what I know about lasers, electron beams, and plasma physics; and deciding to learn under Jeroen's daily advisement, is unquestionably the best decision I've made in my time as a graduate student. Never have I met someone who has stayed calm when the situation called for anything but calmness. He stayed positive when nothing was going right. If I had done everything the way I watched Jeroen do things, I could have saved myself a lot of time and hassle. Thank you Jeroen for everything you've done for me. Christina, Noémi, and Chloe are very lucky to have you as their husband/father. I learned more from you than you even know.

Sven: Sven came along half way through my time in Berkeley. Joined the group and joined the staging team. Once I was placed on the staging team, our professional and person relationship grew quickly. Sven has a deep understanding for the things he knows, and has a very strong desire to know more. I hope his pursuit of ion acceleration becomes a reality and he takes on grad students to learn under him. Those students will get an amazing mixture of incredible stories, a strong understanding for the physics of the problem at hand, and a really enjoyable person to work under. I'm grateful for the time he has spent working and all the help he has given me.

John Crane: The four summers I spent as a summer student at the Lawrence Livermore National Lab really helped me realized that I was pursuing a field that I cared about. John Crane gave me my first opportunity in research in the summer of 2006, hiring me as one of his two summer students, and I will always be grateful for him giving me this opportunity. I had an idea of what I wanted to do, but the opportunities that John gave me helped me ensure I was making the correct choice. I hope to stay in the research world, and if given the opportunity I hope to give future students the opportunities you gave me. Thank you John for giving me my first break.

Graduate Student Experience: I struggled in my first few years of the program. During this time there were a few key people who were very helpful in my success on campus. Professor David Attwood is the first person I want to thank. I learned a lot from him and enjoyed our meetings very much. He is a professor who has students' interests as a top priority and someone who I will try to emulate as I begin a career in sciences. Professor Jonathan Wurtele is another professor who went out of his way to help me during my time at Cal. His advice on grad school and looking beyond graduation has been very helpful, and I hold his opinion in very high regards. While taking courses Genia Vogman was always someone I looked forward to seeing and discussing school, work, and the headaches that come with both. I saw Genia as someone who was going through the same struggles I was, and having someone to talk to and work with was a huge help and I know she played a big role in my years on campus. In my later years of grad school I took a more active role in my graduate group AS&T. Crystal, Kenny, Brandon, and Kasra are all great students, and I'm very confident in the years to come for the AS&T group because of their help in getting AS&T back to a community. Lastly, Tobirus Newby helped me as a counselor in ways I did not expect. My discussions with Tobirus changed my entire experience as a graduate student. After my first discussion with Tobirus I knew I had found an amazing

resource and someone who was there to listen when I needed him. When I look back at my experiences at Cal, Tobirus will always stand out as the person who got me through my toughest times. I recommend him to all the young graduate students whom I see are stressed out and overwhelmed.

My friends: My friends have always been very important to me. During my time at grad school it was hard to find time to meet up as much as I would have hoped to, but it was always refreshing to get together and it felt like we didn't miss a beat. Having gotten married in my first summer of grad school was a great day (top 2 days of my life) and sharing this experience with them was amazing. Since then, celebrating their weddings, birthdays and other great times together helped me relax and they here always supportive of my efforts and hard work. In order to not leave someone out (and have it in print forever) I'll skip listing my friends, but if you were invited to bachelor party, my wedding, baby showers, Peyton's birthdays, pumpkin parties, fight nights.... Thank you for your friendship and support.

My colleagues: The science being done at the BELLA Center is truly world class, and our recent milestones are proof of this. But the people at the BELLA Center made my time in the group special. I feel like I made a connection with nearly everyone who had a spot in building 71, and I hope I made a positive impact on their time at BELLA. I always tried to cheer people up, make people laugh and put smiles on peoples faces. I hope I will be remembered as a friend and good student, because I have many memories of personal interactions at the BELLA Center that I learned from, or laugh at looking back. It truly is a great group of scientists and support personnel, and I will miss daily interactions with the members of the BELLA Center.

This work was supported by the National Science Foundation (NSF) under contracts 0917687 and 0935197, the United States Department of Energy under Contract No. DE-AC02-05CH11231, United States Defense Threat Reduction Agency (DTRA), and the Lawrence Berkeley National Labs Laboratory Directed Research and Development (LDRD) support.

Previously published work has is been published in Journal of Applied Physics (114, no. 4 (2013): 043106-043106) and Advanced Accelerator Concepts Proceedings (15th Advanced Accelerator Concepts Workshop, vol. 1507, no. 1, pp. 310-314. AIP Publishing, 2012).

Chapter 1

General Introduction

1.1 Conventional versus plasma-based acceleration

In order to feed a synchrotron with protons or electrons, the particles begin the acceleration process in a linear accelerator which accelerates particles from rest to high energies by interacting the charged particles with a series of oscillating electric potentials along a linear beamline. A linear accelerator is ideal for relativistic acceleration of electrons, because fast electrons traveling in an arc will lose energy through synchrotron radiation; limiting the maximum power provided to electrons in a synchrotron of given size.

Examples of proposed relativistic linear accelerators are: (1) the International Linear Collider (ILC) and (2) Compact Linear Collider (CLIC). These proposed projects plan to accelerate electrons and positrons up to energies of 500 GeV (ILC) and 3 TeV (CLIC) [6, 7, 8, 9, 10, 11]. Using conventional radio-frequency (RF) accelerating technology with acceleration gradients of 35-60 MeV/m, the projects are estimated to be 30-50 km in length to overlap (and interact) the electron beamline and positron beamlines. The large size of conventional accelerators is due to the magnitude of the accelerating gradients that can be achieved using RF electric fields inside metallic cavities [as shown in Fig. 1.1(a)]. As the electrons propagate down the accelerator, the RF electric fields oscillate from positive to negative fields (and negative to positive) in phase with the electron beam's propagation through the accelerator. This oscillation of electric field produces a positive accelerating field during the entire propagation down the accelerating structure.

Other technologies are being investigated as ways to accelerate particles on shorter length scales. Laser plasma accelerators make use of higher accelerating gradients compared to RF-accelerators, accelerating particles to GeV levels in centimeters rather than 10's or 100's of meters. The maximum accelerating gradients using RF technology are on the order of 100 MeV/m [3] due to the breakdown within the walls of the RF-accelerator cavities at higher fields. By eliminating the need for metallic cavities to sustain the RF fields, the acceleration gradients for LPAs are determined by the magnitude of the electric field gradient which can be established in the plasma. Electric field gradients within a plasma can reach two

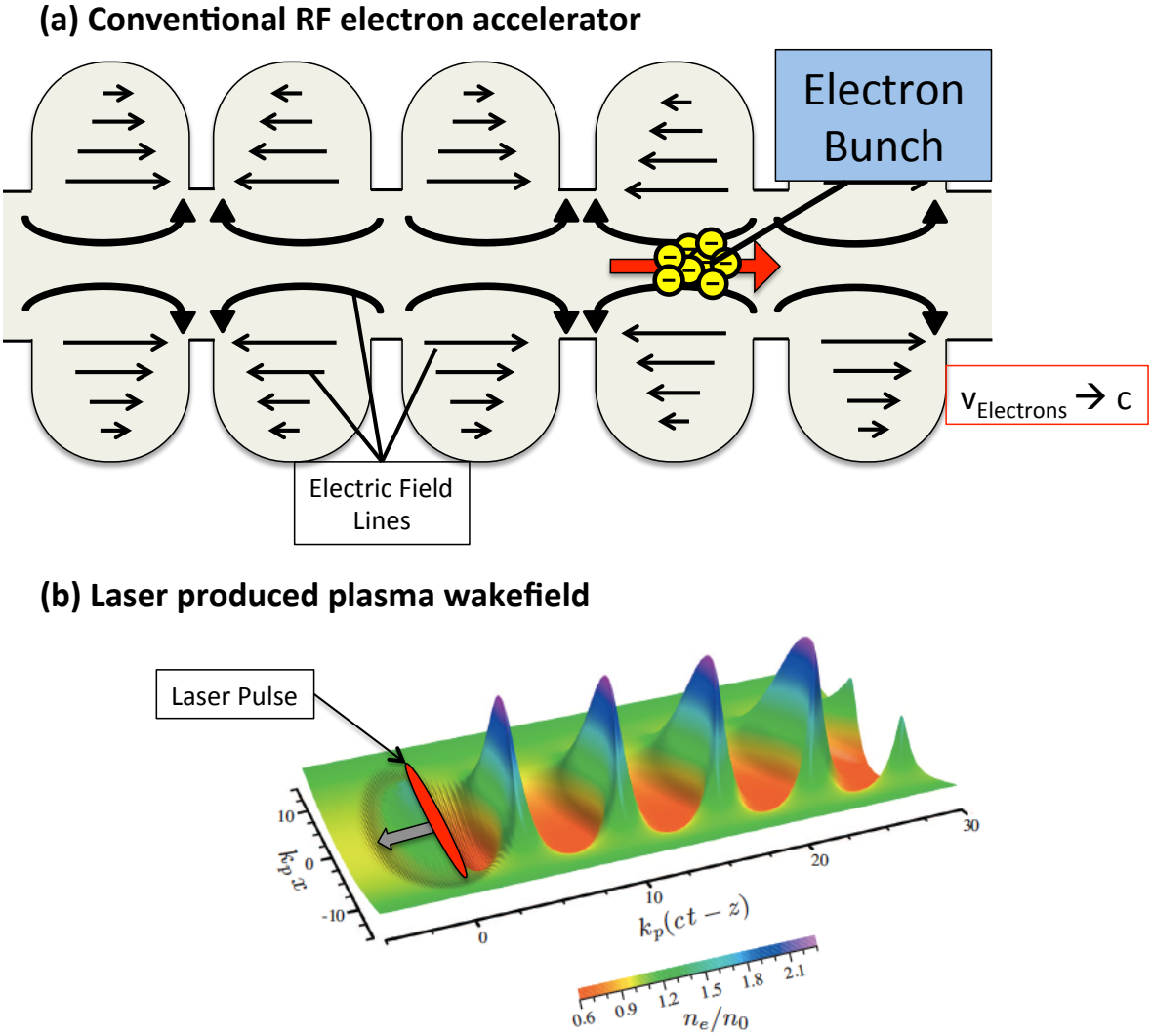

Figure 1.1: Schematics of accelerating structures for both conventional and plasma-based accelerators. (a) Conventional accelerator RF cavities where accelerating fields are sustained by charged metallic cavities. The RF electric fields oscillate from positive to negative fields in phase with the electron beam's propagation down the accelerator; creating a positive accelerating field during the entire propagation. (b) Plasma density perturbation excited by Gaussian laser pulse traveling to the left. LPA accelerating fields are produced by the electric fields created from localized electron density modulations. LPAs can support accelerating gradients 100-1000 times greater than those found in conventional RF-accelerators. Fig. (b) from Ref. [3].

to three orders of magnitude higher than those sustained in metallic cavities of an RF-accelerator. Therefore, with LPA electric field gradients 100-1000 times larger then those in RF-accelerators, the length of an LPA can be 100-1000 times smaller than an RF-accelerator to produce particles of the same energy.

Many state-of-the-art plasma accelerators operate at 1-10 Hz or lower [12, 13, 14]. This

is currently due to the need for a powerful laser to drive LPAs. As laser technology advances towards higher repetition rate for high peak power lasers, the appearance of higher repetition LPAs could soon follow.

1.2 Laser-plasma interactions

The motion of a single electron caused by an electromagnetic field E and B in vacuum is described by the Lorentz equation [15]:

$$\frac{d\mathbf{p}}{dt} = \frac{d\left(\gamma m_e \mathbf{v}\right)}{dt} = -e\left(\mathbf{E} + \mathbf{v} \times \mathbf{B}\right). \tag{1.1}$$

For non-relativistic electrons (v/c<<1) and the ($\mathbf{v} \times \mathbf{B}$)-term can be neglected and the maximum oscillation velocity of the electron $v_\perp$ is used to define the normalized potential for a laser pulse which interacts with an electron as a_0, given by

$$a_0 = \frac{p_\perp}{m_e c} = \frac{v_\perp}{c}. \tag{1.2}$$

Where $p_\perp$ is the transverse momentum of the electron interacting with the light wave, and m_e is the rest mass of an electron $m_e = 9.1 \times 10^{-31}$ kg.

As the velocity of the electron approaches the speed of light, the electron motion becomes relativistic and assumptions used for Eq. 1.2 break down. As the transverse velocity approaches c, $p_\perp = \gamma m_e v_\perp$. Now, a_0 takes the more general form,

$$a_0 = \frac{eE_0}{m_e \omega c}, \tag{1.3}$$

which can be rewritten as

$$a_0^2 = 7.3 \times 10^{-19}[\lambda(\mu m)^2 I_0(W/cm^2)], \tag{1.4}$$

with λ the wavelength and I_0 the intensity [3].

The normalized laser potential, a_0, the electric field potential of the laser on an electron normalized to the rest energy of an electron. For $a_0 < 1$ the interactions are treated non-relativistically. For $a_0 \sim 1$ the interaction will be weakly relativistic. For $a_0 >> 1$ the interaction will be strongly relativistic.

A plasma, which is a electrically neutral medium of unbound positive and negative particles, can undergo collective effects which don't appear for single particle motion. The particles which make up the plasma are electrons which are assumed to move freely, and ions which are more massive than electrons and are assumed to by stationary. One example of the collective effects of a plasma is the plasma's ability to rearrange and screen an electric potential, known as Debye shielding [16]. If an electric potential in introduced within a

plasma, the plasma electrons react to the potential and a change in the localized density is seen. The characteristic length of a plasma to screen a charge is known as the Debye length,

$$\lambda_D = \sqrt{\frac{\epsilon_o k_B T_e}{n_e e^2}}, \tag{1.5}$$

where k_B is the Boltzmann constant, T_e is the electron temperature, and n_e is the electron density. The Debye length determines how far electrostatic effects can be felt within a plasma when a charge is present. A Debye sphere is a volume whose radius is the Debye length, in which there is a sphere of influence, and outside of which charges are electrically screened.For typical plasmas used in LPA target in this thesis, $n_e \sim 10^{18}$ cm^{-3}, and $T_e \sim 10$ eV, giving $\lambda_D \sim 24$ nm.

Another characteristic of a plasma, which is determined by the density of the plasma, is the plasma frequency, ω_p. When a laser pulse interacts with a plasma, electrons will be slightly displaced and ions remain at rest causing a localized charge separation. This charge separation creates an uniform electric field, which produces a restoring force. The resonance of the resulting oscillation is known as the plasma frequency

$$\omega_p = (n_0 e^2/\epsilon_0 m_e)^{1/2}, \tag{1.6}$$

here n_0 is the plasma density, the permittivity of free space is $\epsilon_0 = 8.85 \times 10^{-12}$ F/m and the charge of an electron $e = 1.6 \times 10^{-19}$ C. For a typical LPA plasma density, $n_0 \simeq 10^{18}$ cm^{-3}, the plasma frequency $\omega_p = 5.7 \times 10^{13}$ Hz.

The density of the plasma that interacts with the laser pulse also determines the propagation conditions of the light. There is a critical plasma density, called n_{crit}, which is seen for a plasma with its plasma frequency equals the frequency of the interacting light. The critical density is given by

$$n_{crit} = \frac{\epsilon_o m_e \omega_{Laser}^2}{e^2}. \tag{1.7}$$

A laser pulse with a wavelength $\lambda = 800$ nm has a critical density of $n_{crit} = 1.7 \times 10^{21}$ cm^{-3}.

When a laser pulse interacts with a plasma with a density higher than that of the critical density (over-critical), the light can't propagate through the plasma. This is seen in the derivation of the index of refraction within a plasma. The dispersion relation for electromagnetic waves in plasma is given by

$$\omega^2 = \omega_p^2 + c^2 k^2, \tag{1.8}$$

c is the speed of light and k is the wave number of the light. Using the relationship between the wave number and the index of refraction

$$k = \frac{2\pi}{\lambda} = \frac{\omega}{v_{Phase}} = \frac{\omega n_{Ref}}{c} \tag{1.9}$$

we can solve for the index of refraction, n_{Ref} in terms of the the plasma frequency

$$\omega^2 = \omega_p^2 + c^2 k^2 = \omega_p^2 + \omega^2 n_{Ref}^2 \rightarrow n_{Ref} = \sqrt{1 - \frac{\omega_p^2}{\omega^2}} \tag{1.10}$$

and plugging in for ω_p and the laser frequency $\omega = \omega_L$, n_{Ref} in terms of the critical density is given by

$$n_{Ref} = \sqrt{1 - \frac{\omega_p^2}{\omega^2}} = \sqrt{1 - \frac{n_p}{n_{crit}}}. \tag{1.11}$$

Therefore, it becomes obvious that n_{crit} divides the properties of the plasma into transparent (underdense) if $\omega_p < \omega_L$ ($n_p < n_{crit}$) and opaque (overdense) if $\omega_P > \omega_L$ ($n_p > n_{crit}$). The wave vector k becomes imaginary if $\frac{n_p}{n_{crit}} > 1$ and hence electric and magnetic field decay exponentially. An evanescent field can penetrate into the overdense region up to a characteristic length, the collisionless skin depth, l_s, given by

$$l_s = \frac{c}{\omega_p}. \tag{1.12}$$

1.3 Staged acceleration

While the main advantage of LPAs is the significant size difference between an LPA and a conventional accelerator, a major hurdle for LPAs is the upper limit of energy achievable with a single staged accelerator. The current world record for electron energy achieved from an LPA is 4.25 GeV [2] produced at the BELLA Center at the Lawrence Berkeley National Laboratory using a peak power of 300TW (16 J, 40 fs) and a 9-cm-long capillary discharge waveguide with a plasma density of $\simeq 7 \times 10^{17}$ cm^{-3}. In order to reach electron energies higher than 10's of GeV, a multiple staged accelerator could be used to overcome some of the technical challenges associated with of LPAs.

The biggest challenge for a single staged LPA system is the required energy depletion from the laser to the plasma [3, 17]. The key to this staged acceleration technique is to couple the electron beam from the first stage into a second stage which is controlled independently of the first stage to trap the electrons into the accelerating phase of a new, independent plasma wakefield.

In order to couple out the laser pulse from the first accelerating stage and couple in the second laser pulse for the post accelerating stage, timing between the two laser pulses must be tuned to femtosecond precision. The optic which couples the pulses in (and out) of the beamline must be able to overcome the damage created when reflecting the second laser pulse within centimeters of focus (Peak intensity at focus = 2×10^{18} W/cm^2). A tape-based plasma mirror has been fully characterized and commissioned as the optic between accelerating structures for the two-staged accelerator experiment. A schematic of the two target accelerator is given in Fig. 1.2, and a CAD drawing of the two accelerating stages and the plasma mirror is shown in Fig. 1.3.

1.3.1 Plasma mirror

During the interaction between a laser pulse and a solid surface, an ultra-fast formation of a surface plasma can occur. A plasma mirror relies on a self triggering mechanism which

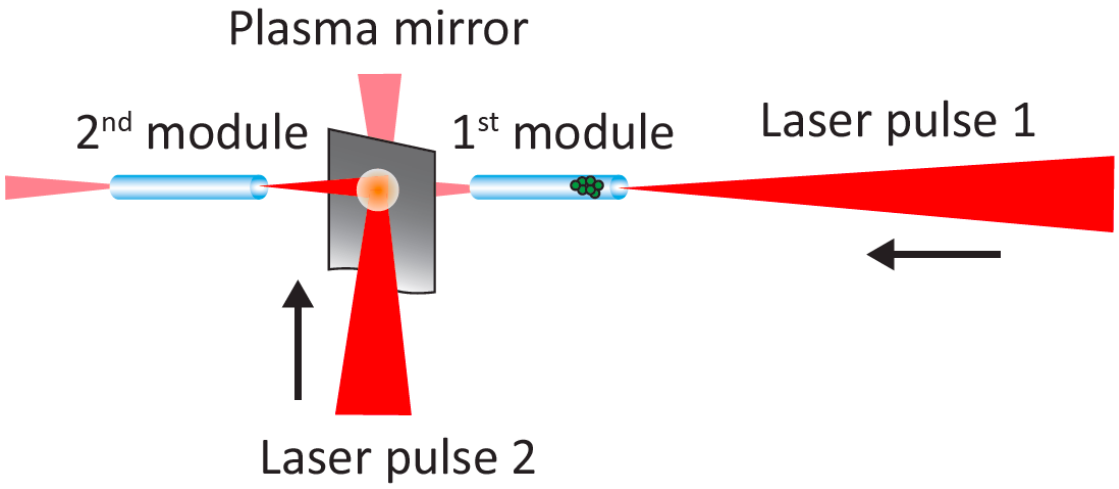

Figure 1.2: A schematic of the staged acceleration experiment's focal geometry. Image from Reference [18]. The electron beam is produced in the first accelerating stage (Laser pulse 1 focused into the 1st module which is shown as a gas filled capillary discharge). Following the exit of the first module, the electron beam travels through the thin tape, and is coupled into the second stage (Laser pulse 2 focused into 2nd module which is also gas filled capillary discharge) for post acceleration. The tape between the two accelerating modules also acts as a plasma mirror and is used to couple a laser pulse from the first stage out of the beamline, and couples a new laser pulse into the second stage to drive the plasma wave in the second module.

works by ionizing a surface plasma before the peak of the laser pulse arrives, and reflecting the peak of the pulse with the over critical density plasma ($n_{Plasma} > n_{crit}$). This results in reflection of both laser pulses.

Since the first demonstration of a plasma mirror in 1991 [19], plasma mirrors are most commonly used to improve the contrast of a laser pulse. The contrast of a laser pulse is the ratio of the intensity of the peak of the pulse, and the signal before the peak of the pulse. The signal before the peak of the pulse can be caused by prepulses, amplified spontaneous emission (ASE) or coherent scattering within transmissive optics. A contrast enhancement occurs from a PM reflection because the light which has an intensity below the ionization is not reflected on the rising edge of the pulse. Once the plasma mirror is formed the reflected signal level has been experimentally measured to as high as 96% of the input energy [20]. The lack of reflection prior to ionization and high reflectance following ionization, results in an enhancement of the ratio between the peak of the pulse and the prepulse.

A disadvantage of this type of laser-solid interaction is that the formation of a surface plasma is destructive to the solid surface in the area of the laser focus. After each shot, a fresh surface must replace the previous target to allow the next shot to interact with a flat and undamaged target. Using a long, spooled tape as a plasma mirror has the advantage over more conventional, polished-glass plasma mirrors, because a tape is long and provides a large number of plasma reflections before the tape must be replaced. An alternative solution relies on a water film [21, 22] but this is technically more challenging.

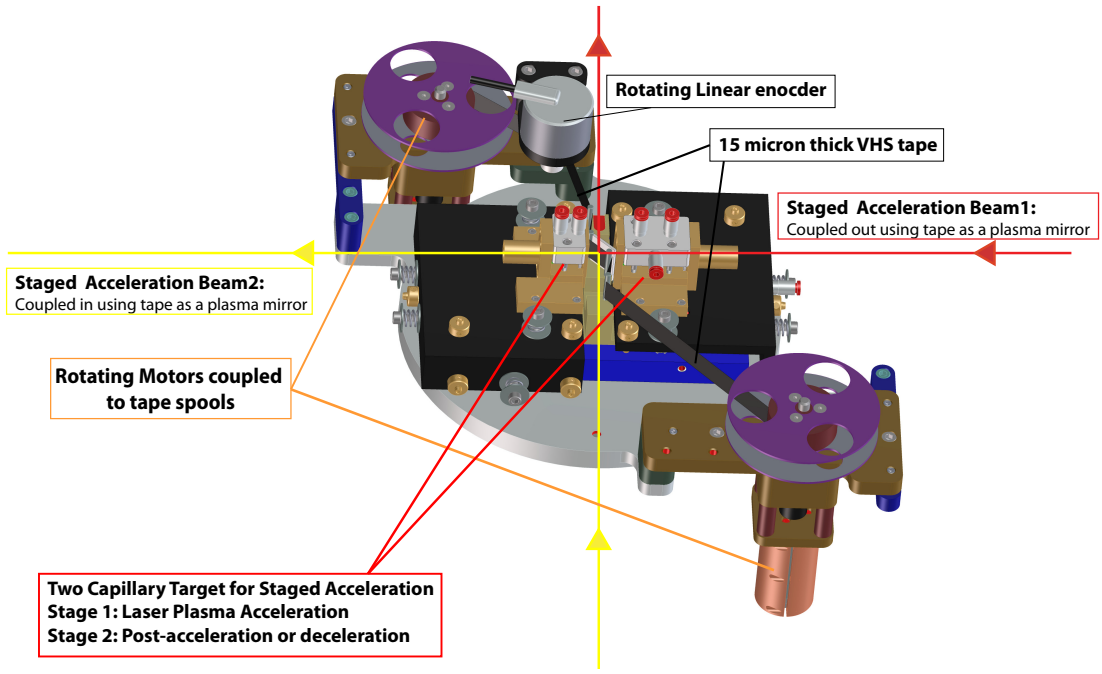

Figure 1.3: A schematic of the tape drive with the two capillaries mounted in the staged acceleration experimental geometry is shown. For this experiment, the tape spooled by the tape drive acts as a plasma mirror at 45°, coupling a second laser pulse which is overlapped in time and space with an electron beam from the first stage. The tape drive consists of two motors coupled to rotating reels for spooling the tape, a rotating linear encoder, and metal pegs to maneuver the tape into place.

Since the reflection from a plasma mirror is a specular reflection, its applications go beyond the use for pulse contrast enhancement. With a high quality reflection, a plasma mirror could also be used as a reflective optic, in spaces near focus, where damage to solid surfaces will occur. Figure 1.3 shows the tape drive spooled with a thin tape used in the staged acceleration setup [18] at the BELLA Center. This is the application for which the tape-based plasma mirror was characterized for this dissertation.

1.4 Free-electron lasers

An LPA-based free-electron laser (FEL) is one application which could take advantage of a plasma-based electron accelerator. An LPA-based FEL would not require electron beam energies higher than those which have been achieved with current LPA technology [2]. With current laser technology, a chirp pulse amplification (CPA) based, multi-TW laser system of this power could fit in a university-sized laboratory.

With the goal of making an FEL with the smallest possible footprint, seeding the electron bunch with resonant light at the FEL wavelength will further shorten the undulator length needed for gain saturation. One possible layout of an LPA-based seeded FEL is shown in Fig. 1.4. This FEL design uses surface high-harmonic generation (SHHG) of an infrared (IR)

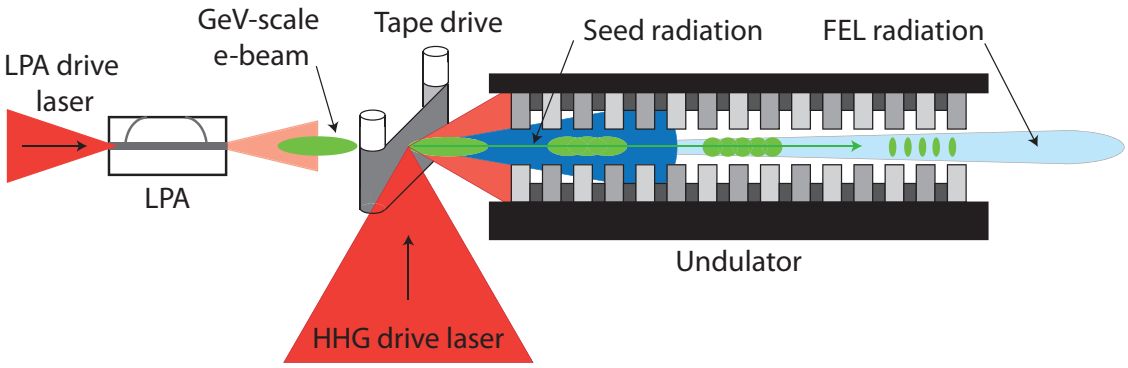

Figure 1.4: A schematic for a possible layout for a CWE-seeded LPA-based FEL. This layout uses an LPA to produce an electron beam, which is injected into an undulator to produce radiation. By placing a high harmonic generating source at the entrance of the undulator, resonant photons can be used to enhance the positioning of the free electrons into microbunches at the undulator wavelength. This process, known as seeding, is used to shorten the length of the undulator needed to position the electrons into periodic microbunches, which then radiate coherently.

drive laser to produce photons at the same wavelength as first order of undulator radiation (λ = 53 nm). As the seed photons overlap with the free electrons in the undulator, the electrons are driven into bunches separated in space by the wavelength of the seed and undulator light. For example, if the electron bunches are separated by 53 nm, and the wavelength of the seed light is equal to the wavelength of the radiation produced by the electrons' undulator oscillations (λ = 53 nm), the light radiating from each electron bunch interferes constructively, leading to gain in the FEL output signal.

The SHHG process explored in this thesis, known as coherent wake emission (CWE), is a process where a sub-relativistic laser pulse interacts with a surface plasma. The laser interacts with the free surface electrons, which radiate periodically at the laser frequency, leading to harmonics in the reflected pulse.

1.4.1 Coherent wake emission

Coherent wake emission (CWE) is a harmonic generating process which occurs on the surface of an overdense surface plasma. The process begins once a surface plasma is produced that expands to form a plasma density gradient. Once the gradient is formed, the laser undergoes Brunel absorption [23].

Brunel absorption begins by pulling electrons out of the plasma by a p-polarized laser's electric field component perpendicular to the target surface. When the electric field inverts, the electrons are accelerated back towards the surface plasma. The electrons propagate through the density gradient and beyond the critical surface. The critical surface is the surface within the plasma gradient where the electron density (n_{Plasma}) equals the critical density of the input light ($n_{crit} = \frac{m_e \epsilon_0 \omega_{Laser}^2}{e^2}$). Beyond the critical surface the electrons are

no longer affected by the electric field of the laser. Once the electrons are beyond the critical surface, they propagate freely through the plasma and excite plasma waves. These plasma waves undergo linear mode conversion [16] and radiate at the local plasma frequency within the density gradient. Because the relationship between the local electron density and plasma frequency is $\omega_p \propto n_e^{1/2}$, the maximum frequency which can be produced by CWE is equal to that of the plasma frequency of the solid bulk material.

The highest possible harmonic order produced (N_{max}) is given by

$$N_{max} = \omega_p^{max}/\omega_{Laser} = \sqrt{n_{max}/n_{crit}}, \tag{1.13}$$

where n_{max} is the maximum electron density of the solid used for SHHG and n_{crit} is the critical plasma density of the light used to produce the SHHG signal.

For the experiments described in this thesis, a thin tape was used to produce the CWE harmonics. Thin tape was used in the FEL layout shown in Fig. 1.4, because it allows an electron beam to propagate through the target used for producing the CWE signal. Also, the tape allows for a new surface to be spooled, creating an undamaged surface to produce a CWE source for each laser shot. A full characterization of CWE produced from a thin, spooling tape surface is presented in Chapter 4.

1.5 Overview

The experimental campaigns discussed in this thesis were performed using the TREX laser system. The TREX laser currently feeds two separate beamlines with different intensities on target and two different target geometries. One of the beamlines sends 50 TW laser pulses to a single LPA target and is used to produce electron beams which get sent to the THUNDER undulator [4]. This beamline is referred to as the "Undulator Beamline" for the rest of this thesis.

The second beamline of the TREX laser is the staged accelerator beamline, which splits the input laser using a beam splitter, and sends each pulse to focus in one of the two targets of the staged acceleration experiment. This beamline will be referred to as the "Staging Beamline" for the duration of this thesis. The TREX laser system and its two beamlines will be described in detail in Chapter 2, in Section 2.2.1.

The experimental campaigns discussed in this thesis show progress towards two high profile topics within the LPA community: (1) an LPA-based FEL and (2) a multi-staged laser plasma accelerator. Each of these topics presents a number of different challenges beyond current LPA technology.

First, an LPA-based FEL could be produced using beam energies which have already been produced by LPAs. The beam parameters for an electron beam which would be ideal for driving an FEL at the BELLA Center using the THUNDER undulator beamline are 310 MeV electrons to produce coherent undulator radiation and eventually see gain at $\lambda = 53$ nm.

Chapter 3 comprises of the experimental results to produce extreme ultra-violet (EUV) radiation by oscillating LPA-produced electron bunches within the THUNDER undulator [5].

The results show broadband spectrums of spontaneous radiation at photon energies from 15 eV to beyond 100 eV. A discussion on the mechanisms causing undulator harmonics is discussed, as well as how the shape and width of the harmonic orders give insight into the electron beam's energy spread and divergence [5, 24].

Chapter 4 focuses on the study of finding a suitable FEL seed using CWE from thin, spooling tapes [25, 26]. The CWE signal produced from a tape is explored for a number of different material surfaces. The experiment was performed on the staging beamline, which allowed for characterization of the harmonic spectrum and 2D mode profile of the EUV light. The setup allowed for full characterization of the amount of signal produced at the FEL resonant wavelength of 53 nm and the divergence of each harmonic order. To understand the results of different harmonic divergences seen from different tapes materials, we took two measurements of the surface roughness of each of the materials used in the study, and both measurements showed a clear correlation between the surface roughness and SHHG divergence [25]. Lastly, a microbunching model was used to show that the CWE signal which was produced from VHS tape is powerful enough to enhance microbunching in the current length of the THUNDER undulator [27].

The second laser-tape interaction which is experimentally characterized is the tape-based plasma mirror (PM) reflection used just before the second acceleration module in the staging experiment [28, 29]. Chapter 5 presents the experimental characterization of the highly reflective plasma mirror using the tape as a quasi-infinite, thin, spooling reflective optic near focus [30]. The characterization of the tape-based plasma mirror includes a study of the amount of reflected signal by changing (1) polarization of input light, (2) the tape material used as the reflective surface, and (3) a scan of the laser focus, which changes the spot size and intensity of the laser during interaction with the tape. A simple model of the PM is presented and used to explain the three different parameter studies. The model shows the importance of the ionization time of the surface plasma within the coherent shoulder of the femtosecond pulses [30].

Lastly, a summary of the work presented and outlook of future research are provided in Chapter 6.

This thesis includes experimental results published, submitted or in preparation:

- **B. H. Shaw**, J. van Tilborg, T. Sokollik, C. B. Schroeder, W. R. McKinney, N. A. Artemiev, V. V. Yashchuk, E. M. Gullikson, and W. P. Leemans. "High-peak-power surface high-harmonic generation at extreme ultra-violet wavelengths from a tape." *Journal of Applied Physics* 114, no. 4 (2013): 043106-043106.

- **B. H. Shaw**, J. van Tilborg, A. Gonsalves, K. Nakamura, T. Sokollik, S. Shiraishi, R. Mittal et al. "Undulator radiation from laser-plasma-accelerated electron beams." In *ADVANCED ACCELERATOR CONCEPTS: 15th Advanced Accelerator Concepts Workshop*, vol. 1507, no. 1, pp. 310-314. AIP Publishing, 2012.

- J. van Tilborg, **B. H. Shaw**, T. Sokollik, S. Rykovanov, S. Monchoc, F. Qur, Ph Martin, A. Malvache, and W. P. Leemans. "Spectral characterization of laser-driven

solid-based high harmonics in the coherent wake emission regime." *Optics letters* 38, no. 20 (2013): 4026-4029.

- J. van Tilborg, S. Steinke, C. G. R. Geddes, N. H. Matlis, **B. H. Shaw**, A. J. Gonsalves, et al. "Active Plasma Lensing for Relativistic Laser-Plasma-Accelerated Electron Beams" *Phys. Rev. Lett.* 115 (18 2015), p. 184802.

- S. Steinke, J. van Tilborg, C. G. R. Geddes, **B. H. Shaw**, et al. "Multistage coupling of independent laser plasma accelerators" (Submitted).

- **B. H. Shaw**, J. van Tilborg, S. Steinke, W. P. Leemans "Reflectance characterization of tape-based plasma mirrors" (In preparation).

Chapter 2

Lasers and Laser Plasma Accelerators

In this chapter, the technique used to produce ultra-short, high-power laser pulses is discussed. Next, the TREX laser at the BELLA Center is described, and the two beamlines are outlined where the laser system is used on are outlined. By stretching the pulse first before amplifying, the power of the pulse is greatly reduced, while the total energy within the pulse is unchanged. This allows for a large amount of energy to be input into a pulse before the power in the pulse is too large and the damage threshold of the optics in the beamline is exceeded. At the BELLA Center, CPA is used to amplify pulses to energies of 1-10's of Joules and compress pulses down to the order of 10's of femtoseconds which results in peak powers as high as 10^{15} J/s.

Lastly, the way in which the high-powered laser pulses are used to produce relativistic electron beams using laser plasma acceleration (LPA) is explained.

2.1 Lasers

A laser is a light source which uses stimulated emission to amplify a signal of seed photons to produce more photons of the same frequency. The process of stimulated emission requires seed photons of a given wavelength interacting with a gain medium which has a electron distribution in which there is a population inversion. A population inversion occurs within a gain medium when there are a larger number of electrons in a higher energy state than the number of electrons in a lower energy state. This can occur when energy is pumped into the gain medium using another source of photons which get absorbed by the gain medium or through an electrical discharge.

The TREX laser system used throughout this thesis has a central wavelength of ∼800 nm, which is determined by the separation in energy levels for which the population inversion is present. A laser which is centered around 800 nm can be produced using a gain medium of titanium doped sapphire ($Ti^{3+} : Al_2O_3$ or Ti:sapphire). Although the arrangement of energy states of Ti:sapphire is more complex than a 4 level energy model (as depicted in Fig. 2.1), describing a Ti:sapphire crystal as a 4 level system helps to understand how the population

inversion is produced and leads to amplification.

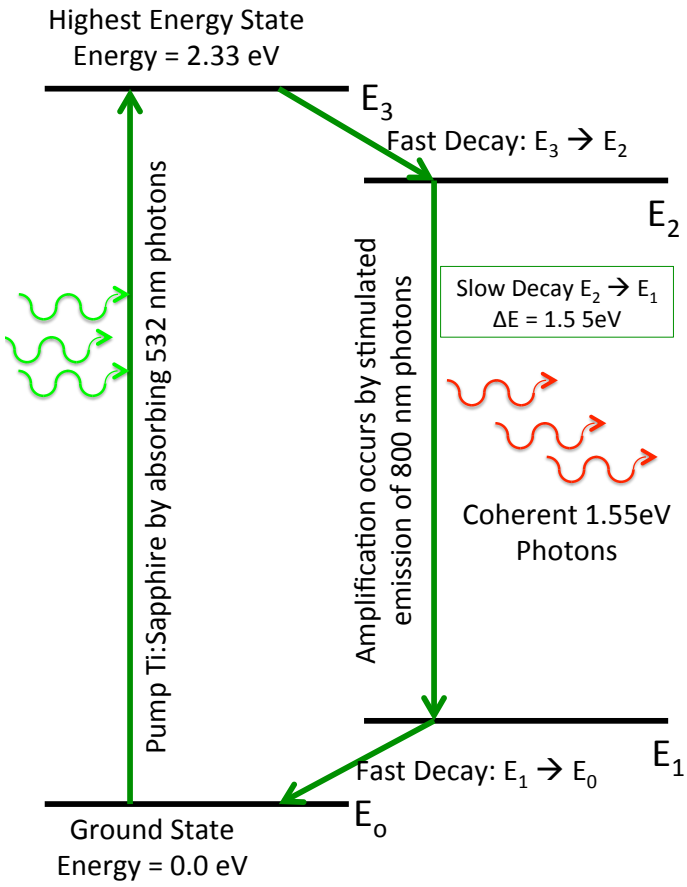

Figure 2.1: Schematic of a laser amplifier crystal with 4 energy bands. This is a simplified version of a Ti:Sapphire crystal used on the TREX beamline. 2.3 eV (visible green $\lambda = 532\ nm$) pump the electrons from the ground state into the highest energy state (E_3). The highest energy state has a fast decay rate compared to the decay rate from level E_2 to E_1. The lowest energy state (above E_0) also has a fast decay rate when compared to the decay rate from level E_2 to E_1. This ratio of decay rates, combined with a pump source creates a population inversion between energy states E_2 to E_1.

A source of 532 nm photons provides photons of energy 2.3 eV which pump the electrons in the ground state of the Ti:sapphire crystal into the upper energy state. With a decay time of order 10^{-13} sec for transitions between states $3 \rightarrow 2$ and $1 \rightarrow 0$, and lifetime of $3.2\mu sec$ between states $2 \rightarrow 1$, a population inversion is quickly produced with more excited electron in state 2 than in state 1. While the system is in a population inversion, if seed photons with the correct energy difference ($\Delta E = E_2 - E_1$) interact with the crystal, the probability of an electron giving up its energy to radiate coherently with the seed photons is higher than the probability of the seed photon giving its energy to an electron in state 1 to transition to

state 2, because more electrons occupy state E_2 than E_1. This is the amplification process of Ti:Sapphire crystals.

An actual Ti:sapphire crystal energy structure has many states which are situated at energies close to the states producing the 800 nm transition. The density of the states in the energy bands leads to transitions which occur at energies close to, but not exactly at, the 1.5 eV transition shown in Fig. 2.1. The resulting photons will have wavelengths around the 800 nm central wavelength. This arrangement of multiple wavelengths (or frequencies) of light centered around a central wavelength (or frequency) gives rise to bandwidth.

2.2 Chirped pulse amplification of laser pulses

Chirped pulse amplification [31] is a technique used for amplifying an ultrashort laser pulse up to Petawatt power levels and above. First coined in 1985 in Ref. [31], CPA uses dispersion to first stretch a laser pulse in time and space, amplification occurs on the long temporal pulse, and the pulse is then recompressed to ultra-short durations, leading to high powers after compression.

A chirped pulse is defined as a pulse having time dependence of its instantaneous frequency. In a stretcher, gratings are set up such that the lower frequency (higher λ) travel a shorter path. A stretcher creates positive chirp, which can be thought of as low frequency arriving first in time, or "red before blue." The counterpart to a stretcher is a compressor, which is setup such that the higher frequencies (lower λ) will have a shorter path length. The compressor reduces the amount of chirp, and is often referred to as "adding negative chirp." Following the right amount of compression, a pulse will no longer have a chirp, referred to as a transform limited pulse, and all the wavelengths have traveled an equal path length. So all wavelengths are overlapped in time.

A schematic of a typical CPA laser system is shown in Fig. 2.2.

2.2.1 TREX laser system

The laser system used in the experiments described in this thesis is the 50 TW TREX system at the BELLA Center at the Lawrence Berkeley National Lab. The TREX laser is a Ti:sapphire-based CPA laser system. A flowchart of each component of the laser system is shown in Fig. 2.3. The laser system is composed of an oscillator, regenerative amplifier, a cross-polarized wave generator (XPW), three multi-pass pre-amplifiers, and the main amplifier which produces pulses with an energy of 3.6 J before the compression and 2.0 J fully compressed on target.

The TREX oscillator is a FemtoSource (by Femtolasers) Ti:sapphire oscillator, pumped by a 3.3 W continuous wave (CW) Millennia laser (by SpectraPhysics) at $\lambda = 527nm$. The oscillator output pulses have a central wavelength of ∼800 nm at 75 MHz with 4 nJ/pulse and pulses of 15 fs. The pulses are then stretched to 220 ps, and a pair of Pockels cells are used to couple the pulses into and out of a regenerative amplifier at 10 Hz. A Pockels cell is a

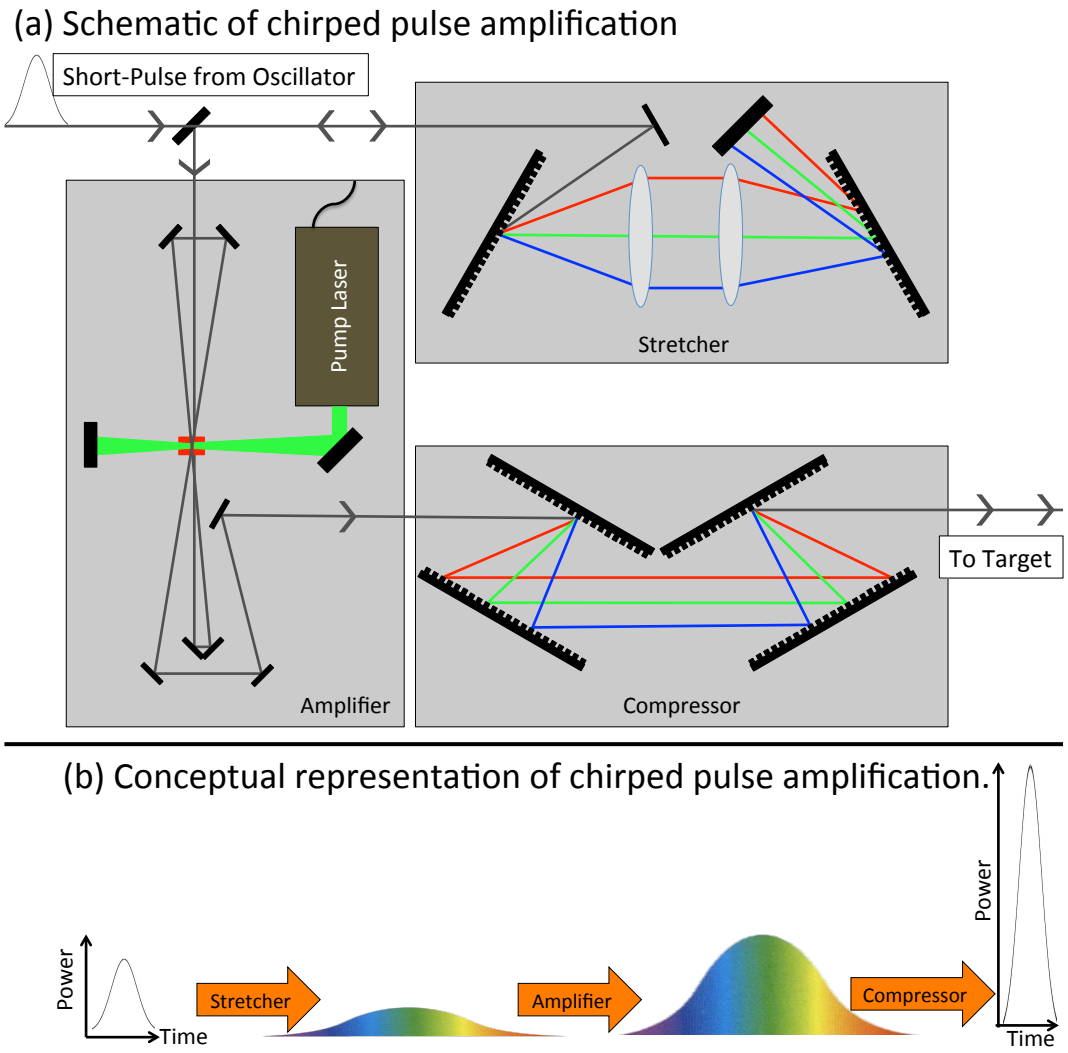

Figure 2.2: Fig. (a) A schematic of chirped pulse amplification [31]. A laser pulse is first stretched using a stretcher to add chirp to the pulse. Next, amplification brings the energy of the pulse up, while the pulse is still stretched. Lastly, the compressor reduces the pulse duration, and brings the power of the pulse up to its final power. Fig. (b) Shows how the pulse length and power change during the three components of CPA. First the beam is stretched, increasing the pulse duration and decreasing the power. Next, the pulse is amplified, increasing the energy but keeping the duration unchanged. Lastly, compression takes place, which shortens the pulse duration and increases the power of the pulse.

device consisting of an electro-optic crystal which pulses propagate through. By applying a variable electric voltage to the Pockels cell a phase delay can be produced in the light within the Pockels cells. This occurs because the crystal within a Pockets cell has a fast axis and a slow axis. The rotation of the crystal is set up such that the polarization of the electric field is decomposed onto the fast and slow axis. By applying the correct voltage a phase delay

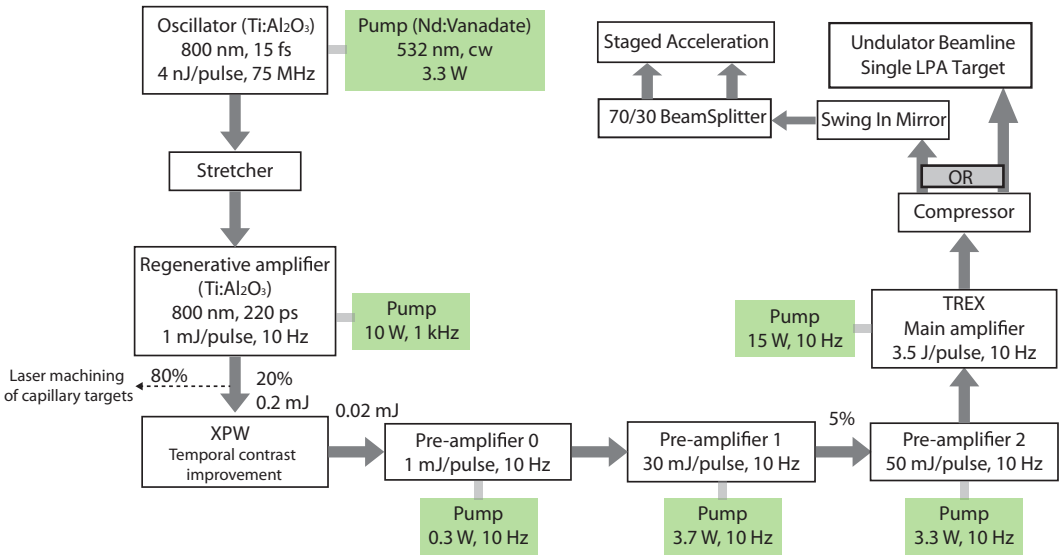

Figure 2.3: Flowchart of TREX laser system at the BELLA Center. Laser pulse duration, energy, and repetition rates are indicated at each of the major components of the beamline.

of $\Delta\phi = \pi$ is creates along one of the axis, and the output wave's polarization is rotated. When placed between polarizers, the Pockels cells act as a nanosecond fast shutter.

The regenerative amplifier (by Positive Light) is pumped using a 10 W Empower laser (by SpectraPhysics), operating at 1 kHz, producing pulses of 10 mW. Unlike a multi-pass amplifier, the regenerative amplifier is an optical resonator cavity with a gain medium inside the cavity. Using an optical switch, pulses are coupled into the resonant cavity and undergo multiple passes through the gain medium which produces small amplifications for each of the many passes (contrary to a multi-pass amplifier which requires few passes due to the high gain per pass). Pulses are then coupled out of the resonating cavity, using an optical switch.

Following the regenerative amplifier, the beam energy is split, keeping only 20% of the energy in the TREX beamline and using the remaining 80% for a test stand for low energy guiding experiments and a laser machining setup.

Following the regenerative amplifier is a cross polarized wave generator (XPW). XPW is a third order nonlinear process, which occurs when pulses interact with an anisotropic crystal of third order nonlinearity (commonly BaF_2) [32, 33, 34]. By placing the XPW crystal between two crossed polarizers, the only light which is transmitted though the set of polarizers is the light which undergoes this third-order polarization rotation. Although the XPW process is very inefficient when comparing the input and output energy, it is able to increase the ratio of the peak of the main pulse to a prepulse from order of 10^{-3} to contrasts of order 10^{-8} to 10^{-9} or better. For many laser-plasma interactions, a contrast of

10^{-8} to 10^{-10} may be required, due to the time scales on which the interactions occur and the expansion velocity of the plasma. For example, coherent wake emission (CWE) requires laser interaction with a plasma gradient with a length scale on the order of $\lambda/20$ [35], and with a typical electron velocity of order 100 nm/ps [36, 37], the plasma must be ionized less than a picosecond before the peak of the pulse arrives. For this to occur, the light before the peak within the 2-3 picosecond coherent shoulder must be suppressed below the ionization level of the surface material. This will be discussed further when solid surface high-harmonic generation (SHHG) is explained in Chap. 4.

Following the XPW, the pulse energy has decreased significantly as a trade-off for improved pulse contrast. The pulses then go through three successive pre-amplifying stages. At the output of the last pre-amplifier the pulses are 50 mJ/pulse at 10 Hz. Next, the main amplifier brings the energy of each pulse up to 3.6 J with a maximum repetition rate of 10 Hz. The main amplifier on the TREX beamline is pumped using 8 frequency doubled Nd:YAG GCR-350s produced by SpectraPhysics. Each of the GCR-350s produce 15 W of pump power at 532 nm second harmonic generation.

The final component which is shared by both the undulator and staging beamlines is the TREX compressor. The compressor is made up of two parallel gratings with a groove density of 1480 grooves/mm and an angle of incidence of $\sim 50°$. After interacting with the pair of gratings, the pulses go through a set of rooftop mirrors, and get sent back through the gratings for a second pass. The compressor is able to tune the pulse duration from 40 fs (fully compressed) to $\geq 1ps$.

Next, the pulses are sent to the switchyard, where a kinematic swing-in mirror is inserted to reflect the beam into the staging beamline, or removed to let the beam pass through to the undulator beamline.

2.2.1.1 Undulator beamline

Following the switchyard, with the swing-in mirror removed, the beam is sent onto a reflective off-axis parabola (OAP) with an f-number f/25. The beam is focused down to a beam waist $\omega_0 = 22\ \mu m$ at the entrance of the accelerating capillary. Figure 2.4 shows the layout of the undulator beamline from the target chamber, downstream to the extreme ultraviolet (XUV) spectrometer. A 250 μm diameter discharged capillary [12], is used to produce electron beams of 100's of MeV. Following the LPA, a magnetic spectrometer (Spectrometer 1) can be used to measure the energy of the electron beam [38]. When the magnet is turned off, the electrons propagate downstream to the Tapered Hybrid undulator (THUNDER) [4]. The undulator consists of three 0.5 m sections, of 22 periods each, and has a periodicity of $\lambda_U = 2.18$ cm. The wiggler parameter, K, is K=1.25, which represents a maximum magnetic field value of +/- 0.60 T on-axis. Following the undulator, the electrons are deflected using a second magnetic spectrometer (Spectrometer 2), and the spontaneous undulator emission is sent to an XUV spectrometer, which is setup to resolve spectra around 100 eV[24].

The XUV spectrometer consists of a focusing grating or a transmission grating, and two dual-stacked micro-channel plates (MCPs). The focusing grating is concave with varying

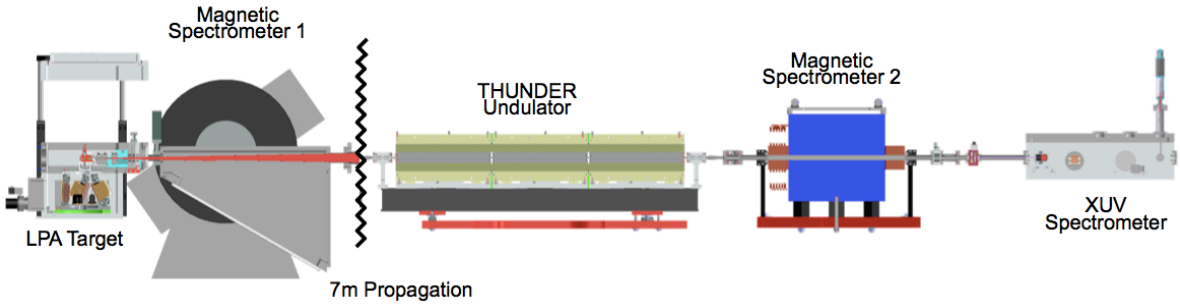

Figure 2.4: The experimental setup of the THUNDER undulator beamline of the TREX laser system. Electron bunches produced by the LPA propagate 7m to the undulator's entrance. The electrons emit extreme ultraviolet (XUV) spontaneous emission, which is sent into the high resolution XUV spectrometer. The XUV spectrometer uses a concave grating to focus the XUV spectrum onto a dual stacked micro-channel plate (MCP), where the emission spectrum is captured and analyzed.

line spacing to focus the 0th and first order undulator spectrum onto each respective MCP. It has a photon resolution of 0.1 nm [5], calibrated at 73 eV, yielding a relative resolution below 1%.

The use of the undulator as a diagnostic for energy spread and electron beam emittance is discussed in Chapter 3.

2.2.1.2 Staging beamline

When the swing-in mirror (SIM) is inserted into the beamline of the TREX laser in the switchyard chamber, the pulses are sent to the staging beamline. Each pulse from the TREX laser system is first split into two pulses using a 70/30 beamsplitter, in order to drive the two accelerating modules independently. Pulses are transported into the staging beamline from the lower right corner in Fig. 2.5. The beam's polarization is rotated from p-polarization to s-polarization in the chamber (#1). S-polarization is used to increase the laser reflectivity of the plasma mirror (As discussed in Chapter 5). Before splitting the pulse, the pulse energy is 2.0 J. The beam splitter (#2) reflects 70% (35 TW at 40 fs) of the laser energy and transmits 30% (15 TW at 40 fs) of the energy. Laser pulse 1 is used to produce e-beams in the first LPA target. Laser pulse 2 is reflected off the plasma mirror and excites wakefields in the second LPA target for the post-acceleration of the electron beam from the first stage. The arrival timing of the two laser pulses at the target is controlled with a delay stage (#3). Both laser pulses are focused using off-axis parabolic mirrors (OAPs) with f-number f/25. The laser pulses from the TREX laser system are focused down to a spot size of $\omega_0 = 22\ \mu m$ onto plasma targets indicated at the beams' crossing point (#6) .

The staging target chamber contains the target assembly, made up of the first LPA stage, the second LPA stage, and the spooled tape-drive used as a plasma mirror. For the experiments discussed in this thesis, the first accelerating stage is a gas jet. The target

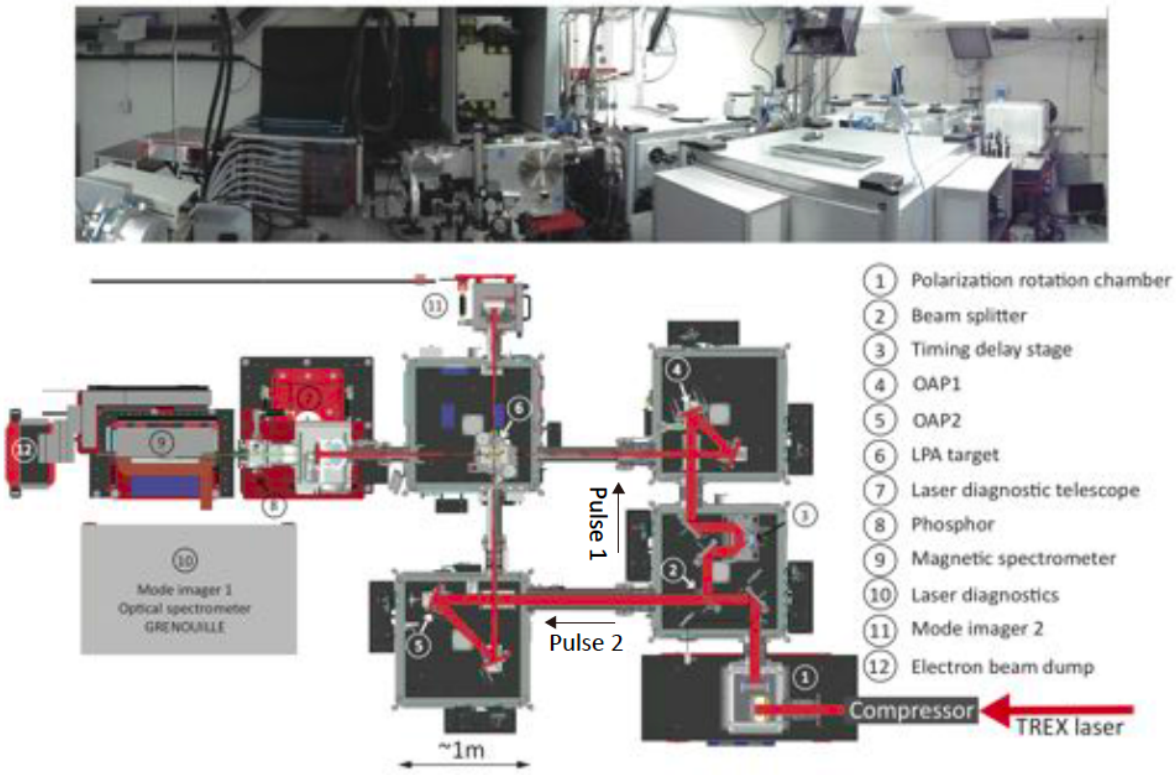

Figure 2.5: The experimental setup of the staging beamline. Top: A photo of the laser transport chambers, laser diagnostic and magnetic spectrometer. Bottom: A CAD model of the experimental setup indicating each component in the beamline [18].

assembly is placed on a hexapod, which allows six-axis adjustment of position and angle. The spooling tape-drive system was used as the plasma mirror in this setup because of its ability to provide a fresh, undamaged surface for each shot, and the tape is thin enough for the electron beam to travel through. The plasma mirror targets studied were VHS tapes and computer data-storage tapes, which are described in greater detail in Chapters 4 and 5. The distance between the first stage and the front surface of the tape is 11.5 mm. The distance between the plasma mirror and the second module is 10 mm.

The laser pulses following each stage of acceleration get attenuated and diagnosed using wedged reflective optics. The first wedge reflects 1% of the energy for diagnosis and the other 99% is transmitted to a laser beam dump. This wedge can be rotated out of the beamline to let the electron beam propagate to the e-beam diagnostics. The optical image of the laser at the target was recorded using a 10-bit charge-coupled device (CCD) camera, referred to as a mode imager. Before the mode imager, the laser pulse is split and optical spectra are measured. A magnetic spectrometer to measure electron energy distribution is downstream of the tape drive. A 1 T dipole magnet deflects the electrons onto phosphor screens imaged by three CCD cameras; enabling single-shot detection of the energy distribution and the

pointing of the electron beam. There is a limiting aperture of diameter 15.24 mm, 2.0 m downstream of the tape drive. So, the acceptance aperture for electron beams into the magnetic spectrometer is 3.8 mrad.

2.3 Laser plasma acceleration of electrons

In plasma-based accelerators a highly intense laser pulse interacts with ionized plasma electrons. The ponderomotive force of the laser pulse creates a density modulation by driving electrons away from the center of the pulse as it propagates through the plasma. Plasma ions are heavier than electrons and are assumed to be stationary during the plasma electrons' response to the laser fields. The ponderomotive force, given by

$$F_p = -\frac{e^2}{4m\omega^2}\nabla E^2, \tag{2.1}$$

where e is the electrical charge of the particle, m is the mass of the charged particle, ω is the frequency of laser pulse, and E is the amplitude of the laser pulse's electric field. Since intensity of a laser pulse scales with E^2, the ponderomotive force scales with the gradient of the laser intensity.

As a result the laser pulse propagates through a plasma, pushing the electrons forward and off axis, this separation of charge leads to the formation of a wake in the density of plasma electrons traveling behind the pulse. The excited plasma wave is described by [3, 39]

$$\left(\frac{\partial^2}{\partial t^2} + \omega_p^2\right)\frac{n}{n_0} = c^2\nabla^2\frac{1}{4}\left(\frac{eE_{Laser}}{mc\omega}\right)^2. \tag{2.2}$$

As the charge separation oscillates behind the pulse, an electric field is produced between regions of low electron densities (ion cavities) and regions of high electron densities (the amplitude or crest of the electron wake).

This charge separations produce electric fields between regions of high and low electron densities within the plasma wakefield. These fields can grow to as large as the cold wave breaking limit [3]:

$$E_0[V/m] = cm_e\omega_p/e. \tag{2.3}$$

Using plasma frequency, ω_p from Eq. 1.6, the speed of light, $c = 3.0 \times 10^8$ m/s, Eq. 2.3 can be approximated as

$$E_0[V/m] \simeq 96\sqrt{n_0[cm^{-3}]}. \tag{2.4}$$

For a typical LPA plasma density, $n_0 \simeq 10^{18}$ cm^{-3} an electric field on the order of $E_0 \simeq$ 96 GV/m can be achieved, which is three orders of magnitude greater than that of a conventional RF-accelerator.

The experiments results of LPA electrons discussed in this thesis are a result of plasma waves excited by a short, intense laser pulse ($> 10^{18}$ W/cm^2). This regime is a quasilinear regime ($a_0 \geq 1$) at which relativistic effects start to appear. At higher intensities ($a_0 >> 1$),

the interaction becomes more relativistic and the laser is able to fully expel the localized electrons. This regime is commonly referred to as the blow-out (or bubble) regime because of the way the laser pulse "blows out" the localize plasma electrons, creating a bubble-shaped density minimum behind the laser pulse. If the correct initial conditions are met for a sub-population of plasma electrons near the laser-plasma blowout bubble (correct initial position and velocity), these electrons can become trapped within the wakefield, and will then be accelerated by the electric fields created by the charge separation within the wakefield. This process of an electron becoming trapped in the wakefield of the laser and becoming accelerated to velocities near the speed of light is know as self-injection. There are a number of ways particles can get injected into a wake. Colliding-pulse injection is a technique which uses the interaction region of two pulses to inject electrons. One pulse is used to drive the density modulation within a plasma, and the second pulse's ponderomotive force is used to push electrons into the plasma wake of the first pulse. ionization injection occurs by ionizing deeply bound electrons from high atomic number (Z) atoms at the proper phase within the wakefield. When electrons are ionized near the peak of the laser field, these electrons are easily trapped. Down-ramp injection can occur when a laser pulse propagates in a plasma with a negative density gradient. This results in the plasma wave's phase velocity decreases as the laser propagates. At the lower phase velocity of the wake, self-injection is more likely to occur. These injections techniques are well understood, and are discussed in detail in Ref. [3].

This concept of a density wakefield following the laser pulse is analogous to a wakefield of a density minimum in a water wave following a speedboat traveling through water. In the water, a surfer will ride in the wake which travels at the speed of the boat producing the wake, and in LPAs, electrons ride in the plasma wakefield which travels at the speed of the laser pulse within the plasma, which is near the speed of light.

2.3.1 Limitations of Laser Plasma Accelerators

The three limitations to the acceleration of electrons using LPA are dephasing of the electron from the accelerating phase of the plasma wave, diffraction of the laser pulse at focus, and depletion of the laser energy to the plasma to produce the charge separation from the ponderomotive force. Dephasing occurs because the phase velocity of the optical field along the axis is greater than the speed of light. For a highly relativistic electron, $v_z \simeq c$, the length,L_D, over which an electron stays within an accelerating region of the wave (of length $\sim \lambda_p/2$) is given by [3]

$$(1 - \frac{v_p}{c})L_D = \lambda_p/2 \rightarrow L_D \simeq \gamma_p^2 \lambda_p. \tag{2.5}$$

Because λ_p and the phase velocity, v_p, are inversely proportional to the plasma density ($v_p = \omega/k$ and ω and k are given by Eqs. 1.8 and 1.9), the way to overcome dephasing is by tapering the plasma density within the accelerator. For example, if an electron is trapped within a highly dense plasma, and the laser sees a negative density gradient, the dephasing

length will increasing and the trapped electrons will stay in the accelerating fields over a larger distance. This longitudinal density tailoring is discussed at length in Ref. [40].

The distance over which acceleration occurs is a limitation of LPAs too, because laser diffraction occurs as the laser propagates through focus. So the laser intensity drops as $(1/w(z))^2$, where $w(z)^2 = w_0^2 \times (1 + (z/z_R)^2)$ and z_R is the Rayleigh length ($z_R \sim 2.0$ mm for the TREX laser focusing geometry). Laser diffraction can be overcome, however, using an optic which counteracts diffraction. At the BELLA Center, diffraction is contracted by using a preformed plasma waveguide produced by pre-ionizing a gas filled capillary of 250 μm in diameter. The round capillary is first filled with a neutral gas, and when a ~ 25 kV discharge is produces across the 33 mm long capillary, the temperature on axis is the highest, producing electrons with the largest kinetic energies. The temperature drops as a function of the radial position within the cap, and the plasma electrons near the walls of the cap have a lower temperature (and kinetic energy) than the electrons on axis. The resulting density profile produces plasmas with minimal densities on-axis and increasing densities further off-axis. Using Eq. 1.11 it is seen that the on-axis index of refraction $n_{Ref} < 1$ and also that the on-axis n_{Ref} is greater than the off-axis n_{Ref}. This produces a focusing effect as the light on-axis travels at a slower phase velocity than the light off-axis. The focusing properties of the capillary discharges used at the BELLA Center are fully described in Ref. [41].

Laser depletion (or pump depletion) is a result of the laser pulses expelling plasma electrons from the propagation axis and exciting plasma wakefield. For this process to occur, the laser pulse must transfer energy into the plasma giving the electrons kinetic energy. The only ways laser depletion can be overcome is if the laser energy can be replenished or if a external non-depleted laser pulse were used after depletion occurs. This is the motivation for the Staged Accelerator experimental campaign described in Sec. 1.3. The use of a non-depleted second laser pulse is first overlapped in time and space using a self-triggering plasma mirror, and the new, fresh laser pulse is able to post accelerate the electron beam in the second acceleration stage.

2.4 Summary and conclusions

This chapter discussed the production of high-power, ultra-short laser pulses using CPA. The laser system used in the experiments outlined by this thesis was described, with all of its components and how they help produce the pulses used for LPA at the BELLA Center. The two beamlines which make use of the 50 TW TREX laser at the BELLA Center were described. The results outlined in chapter 3 makes use of the undulator beamline, while chapters 4 and 5 were performed experimentally on the staging beamline.

Lastly, the basics behind laser-plasma wakefield excitation and electron acceleration were described. Due to the laser's ability to transfer energy to electrons within the plasma medium, a plasma wave and the accelerating fields are formed. The properties of plasma waves are determined by laser intensity and plasma density. Once plasma waves are formed,

electrons may be injected into the wake. The electrons are then trapped in the wakefield, which is traveling behind a laser pulse at velocities near the speed of light.

Chapter 3

Tapered Hybrid Undulator - THUNDER

3.1 Introduction

As laser plasma accelerator technology advances into producing electron beams of higher quality and stability, and applications such as powering a free-electron laser (FEL) are explored, the need for advanced diagnostics will grow concurrently. Diagnostics will need to have the ability to resolve sub-percent energy spread levels, and ≤ 1 mm mrad normalized emittance values on a single shot basis. Due to the large range of energies that an LPA can produce, the current magnetic spectrometers in use at the BELLA Center are all broadband, and have energy resolution above 1% [38]. In addition, this diagnostic does not provide information on the bunching.

To provide higher energy resolution and information on the emittance, an undulator-based diagnostic is employed at the BELLA Center. The spectrum of the spontaneous emission produced from an electron bunch in an undulator gives much finer details about the electrons than a magnetic spectrometer. Since each electron interacts with the same magnetic field throughout the undulator structure, each electron will radiate its own corresponding emission spectrum. Given that undulator radiation is directional, electrons traveling off-axis will radiate differently than those along the axis of propagation; so information about beam size and emittance is available, too. By measuring the spectrum of a single bunch of accelerated electrons, one can resolve energy spreads on the sub-percent level and calculate the beam emittance in the transverse direction.

3.2 First order electron equations of motion

A detailed discussion of synchrotron radiation can be found in Dr. David Atwood's textbook *Soft x-rays and extreme ultraviolet radiation: principles and applications*, Reference [42].

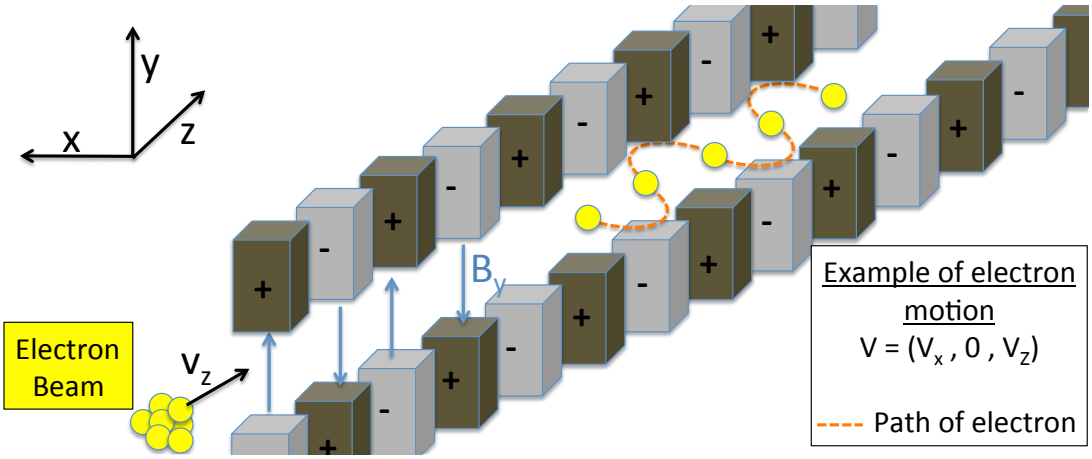

Figure 3.1: A schematic showing an undulator's oscillating magnetic field in +y and -y directions. The initial electron beam velocity and the oscillations within the magnetic field $B_y[z]$ are along the z-axis. The initial motion of the electrons (to first order) will be in the $v_z \times B_y$ direction, which is along the x-axis. It will be shown in section 3.3, that the velocity along the x-axis gives rise to a second order velocity from the $v_x \times B_y$ force, which will lead to motion in along the z-axis too. This motion is the motion of a single electron, and is described in section 3.2.

The equations of motion for an electron traveling in the z-direction (along the axis of an undulator) with magnetic field between the poles of the undulator in the y-axis (as shown in Fig. 3.1), are given to first order by:

$$\ddot{x} = \frac{d^2x}{dz^2} = \frac{e}{\gamma m_e c}\left(B_y - \dot{y}B_z\right) \tag{3.1}$$

$$\ddot{y} = \frac{d^2y}{dz^2} = \frac{e}{\gamma m_e c}\left(\dot{x}B_z - B_x\right) \tag{3.2}$$

where γ is the relativistic Lorentz factor, c is the speed of light, e is the charge of the electron, and m_e is the rest mass of the electron.

Assuming the magnetic field is directed only along the y-axis, the equations of motion for $\ddot{x}$ and $\ddot{y}$ simplify to a single term. This assumption sets $B_x = B_z = 0$ and $B_y = B$. Now Eq. 3.2 becomes $\ddot{y} = 0$, and Eq. 3.1 becomes

$$\ddot{x} = \frac{d^2x}{dz^2} = \frac{eB}{\gamma m_e c}. \tag{3.3}$$

The first order equation of motion is restricted to the x-axis. We know the magnetic field ($B_y = B$) points in the y-direction only, and varies with a period determined by the undulator pole spacing. The undulator period λ_U is defined as the distance between the center of two consecutive poles of the same polarity.

Given the definition of the undulator period λ_U, we can set the magnetic field to a sinusoidal magnetic field of form

$$B_y(z) = -B_o \sin\left(\frac{2\pi z}{\lambda_U}\right), \tag{3.4}$$

and letting $z = c \times t$, gives

$$\dot{x}(z) = \int \frac{d^2x}{dz^2} dz = \frac{eB_o\lambda_U}{2\pi\gamma m_e c} \cos\left(\frac{2\pi z}{\lambda_U}\right) \tag{3.5}$$

Often times a dimensionless parameter is used to simplify the equation for $\dot{x}(z)$, and to give a dimensionless "strength" parameter to describe the undulator. This parameter, K, is given by

$$K = \frac{eB_o\lambda_U}{2\pi m_e c} = 93.4 B_o[Tesla]\lambda_U[meters]. \tag{3.6}$$

The strength parameter K is analogous to the term a_0, which was given in Chap. 2. Similar to how $a_0 > 1$ refers to relativistic interactions and $a_0 < 1$ refers to sub relativistic interactions, if $K >> 1$, the periodic oscillating structure is known as a "wiggler" and if $K \leq 1$ the oscillating structure is known as an undulator. The differences in the spectra produced by undulators and wigglers is described in Ref. [42].

Solving Eq. 3.5, substituting in for K, gives

$$\dot{x}(z) = \frac{K}{\gamma} \cos\left(\frac{2\pi z}{\lambda_U}\right). \tag{3.7}$$

A trivial integration of $\dot{x}(z)$ along the z-axis, by following the same routine to get Eq. 3.3 to Eq. 3.7, gives the first order equation of motion for x(z):

$$x(z) = \frac{K\lambda_U}{2\pi\gamma} \sin\left(\frac{2\pi z}{\lambda_U}\right). \tag{3.8}$$

3.3 Even and odd undulator harmonics

This section is not meant to provide a rigorous derivation of the harmonic orders of electron oscillations caused by electron motion within an undulator (with constants being kept track of and carried out to the end of the derivation), but rather as a path to follow (removing details such as constants by referring to a collection of constants as $A_1, A_2, A_3, etc.$) for a motivated student to carry out in the future at their leisure.

By solving the equations of motion of the electron trajectories, harmonics orders of the fundamental frequency arise. One thing to note is that all of the harmonics of even orders are produced by electron oscillations along the axis of propagation of the undulator (the z-axis of Fig. 3.1), and therefore, the even harmonics are emitted perpendicular to the electron

propagation axis through the undulator. This is due to the $\sin^2\theta$ radiation cone produced by oscillating electrons in a dipole configuration. The odd harmonics (including the fundamental undulator wavelength), on the other hand, are produced by the $\vec{v}\times\vec{B}$ force, from the velocity of the electron propagating down the undulator axis. This force gives rise to electron motion perpendicular to the propagation axis, and produces electron oscillations in the the +/- x direction. The electron oscillations perpendicular to the undulator axis also radiate a $\sin^2\theta$ cone of radiation. This radiation will be directed along the axis of the undulator.

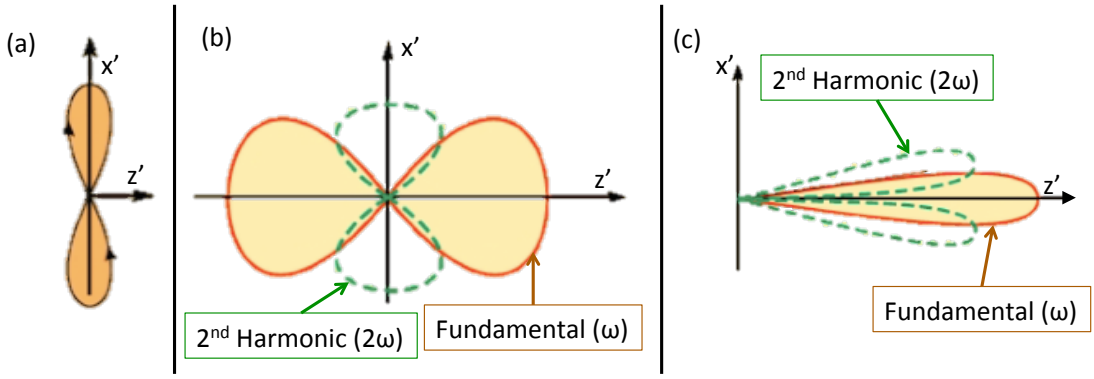

Figure 3.2: Electron motion and the radiation produced by these electron accelerations. (a) shows the propagation of an electron, in the frame of the electron; the x' motion is the first order motion, and the z' motion is the second order motion, which comes from a $\vec{v}\times\vec{B}$ force of the first order motion in x' and B_y. (b) shows the $\sin^2\theta$ radiation cone of an oscillating electron within the electron's frame traveling at $v\sim c$ (with c being the speed of light). (c) shows the Lorentz transformation of the $\sin^2\theta$ radiation cone from the electron frame to the lab frame. Notice that the on-axis radiation in produced by the odd harmonics and the off-axis radiation is made up of even harmonics. Since light is measured in the lab frame, undulator radiation (as detected experimentally) has on-axis odd harmonics and off-axis even harmonics. Image reproduced from Reference [42].

The electron's first and second order of motion are shown in Fig. 3.2. Since the electrons are moving at velocities near the speed of light, the motion is relativistic. While in the frame of the electron the radiation is emitted in a $\sin^2\theta$ cone, a different pattern is seen in the lab frame. The emitted radiation must be Lorentz transformed into the lab frame, which results in odd order harmonics on-axis, and even order harmonics off-axis.

The mathematical algorithm to produce on-axis odd harmonics and off-axis even harmonics, is described below, and because it is repetitive between even and odd harmonics, the calculation can be carried out beyond the 4 orders shown in the calculation, and continued on up to the desired harmonic.

An electron enters the undulator on-axis with velocity v_{o_Z}, and Eq. 3.4, gives the magnetic field of $B_y(z) = -B_o \sin\left(\frac{2\pi z}{\lambda_U}\right)$. The Lorentz force of $\vec{v}\times\vec{B}$ (to first order) gives rise to motion along the x-axis. which comes from Eq. 3.7, $v_x = \dot{x}(z) = (K/\gamma)\cos(2\pi z/\lambda_U)$.

The first order equations of the electron's position and velocity are given by

$$x(z) = \frac{K\lambda_U}{2\pi\gamma}\sin\left(\frac{2\pi z}{\lambda_U}\right) \tag{3.9}$$

$$\dot{x}(z) = \frac{K}{\gamma}\cos\left(\frac{2\pi z}{\lambda_U}\right). \tag{3.10}$$

Using these equations and the $\vec{v}\times\vec{B}$ term of the Lorentz equation, second order velocity and position equations are calculated.

Note: the trigonometric identities that are required are,

$$\sin(\alpha)\sin(\beta) = \frac{\cos(\alpha-\beta)-\cos(\alpha+\beta)}{2}$$

$$\cos(\alpha)\cos(\beta) = \frac{\cos(\alpha-\beta)+\cos(\alpha+\beta)}{2}$$

$$\sin(\alpha)\cos(\beta) = \frac{\sin(\beta+\alpha)-\sin(\beta-\alpha)}{2}.$$

Second Harmonic comes from $\dot{x}(z)\times B_y(z)$:

$$\left(\frac{K}{\gamma}\cos\left(\frac{2\pi z}{\lambda_U}\right)\right)\times\left(-B_o\sin\left(\frac{2\pi z}{\lambda_U}\right)\right). \tag{3.11}$$

To simplify things, and not to be concerned with constants, we rewrite this as

$$v_x \times B_y = A_1\cos(\omega_o)\times A_2\sin(\omega_o). \tag{3.12}$$

Using the trigonometric identities, we are left with a force

$$F_z = \left(\frac{A_1A_2}{2}\right)(\sin(\omega_o+\omega_o)-\sin(\omega_o-\omega_o)), \tag{3.13}$$

which reduces to

$$F_z = m\ddot{x_z} = A_3\sin(2\omega_o). \tag{3.14}$$

Solving for position and velocity,

$$v_z = \dot{x_z} = A_4\sin(2\omega_o) \tag{3.15}$$

$$x_z = A_5\sin(2\omega_o). \tag{3.16}$$

We can refer to this as the second order motion which leads to the production of radiation at $2\omega_o$.

Using the second order motion of the electron, we again use the $v_z(z)\times B_y(z)$ (or equivalently the $\dot{x_z}(z)\times B_y(z)$) force:

$$F_x = m\ddot{x_x} = (A_4\sin(2\omega_o))\times(-B_o\sin(\omega_o)). \tag{3.17}$$

To simplify things, and not to be concerned with constants, we rewrite this as

$$v_z \times B_y = m\ddot{x_x} = A_4\sin(2\omega_o)\times A_6\sin(\omega_o) \tag{3.18}$$

Using the trigonometric identities, we are left with a force

$$F_x = \left(\frac{A_4 A_6}{2}\right)\left(-\cos\left(2\omega_o + \omega_o\right) + \cos\left(2\omega_o - \omega_o\right)\right) \tag{3.19}$$

which reduces to

$$F_x = m\ddot{x_x} = A_7 \cos\left(3\omega_o\right) + A_8 \cos\left(\omega_o\right). \tag{3.20}$$

However, we already have an equation which oscillates at $\cos\left(\omega_o\right)$, so the second term of Eq. 3.20, can be ignored for the sake of this derivation.

Finally, solving for the 3rd order electron motion for position and velocity,

$$v_x = \dot{x_x} = A_7 \cos\left(3\omega_o\right), \tag{3.21}$$

$$x_x = A_8 \cos\left(3\omega_o\right). \tag{3.22}$$

We can refer to this as third order motion which leads to the production of radiation at $3\omega_o$ (electrons oscillating in the x-direction, producing radiation along the z-axis, as predicted).

Using the third order motion of the electron, we again use the $v_x(z) \times B_y(z)$ (or equivalently the $\dot{x_x}(z) \times B_y(z)$) force:

$$F_z = m\ddot{x_z} = \left(A_7 \cos\left(3\omega_o\right)\right) \times \left(-B_o \sin\left(\omega_o\right)\right). \tag{3.23}$$

To simplify things, and not to be concerned with constants. we rewrite this as

$$v_x \times B_y = m\ddot{x_z} = A_7 \cos\left(3\omega_o\right) \times A_9 \sin\left(\omega_o\right) \tag{3.24}$$

Using the trigonometric identities, we are left with a force

$$F_z = \left(\frac{A_7 A_9}{2}\right)\left(\sin\left(3\omega_o + \omega_o\right) - \sin\left(3\omega_o - \omega_o\right)\right) \tag{3.25}$$

which reduces to

$$F_z = m\ddot{x_z} = A_{10} \sin\left(4\omega_o\right) + A_{11} \sin\left(2\omega_o\right). \tag{3.26}$$

However, we already have an equation which oscillates at $\sin\left(2\omega_o\right)$, so the second term of Eq. 3.26, can be ignored for the sake of this derivation.

Finally, solving for the 4th order electron motion of position and velocity,

$$v_z = \dot{x_z} = A_{10} \sin\left(4\omega_o\right) \tag{3.27}$$

$$x_x = A_{12} \sin\left(4\omega_o\right). \tag{3.28}$$

We can refer to this as fourth order motion which leads to the production of radiation at $4\omega_o$ (electrons oscillating in the z-direction, producing radiation in the x axis as predicted).

To the informed reader, it should be well understood how to continue this derivation to higher order harmonics, with even harmonics oscillating in the z-axis, and producing radiation off-axis of the undulator's propagation axis, and odd harmonics oscillating in the x-axis, and producing radiation on-axis of the undulator.

3.4 Experimental setup

Fig. 1.4 shows the layout of the experiment. A 250 micron diameter discharged LPA [12], is used to produce electron beams. Following the LPA, a magnetic spectrometer (Spectrometer 1) can be used to measure the central energy of the electron beam [4]. When the magnet is turned off, the electrons can propagate down toward the BELLA Center's Tapered Hybrid undulator (THUNDER).

3.4.1 THUNDER and extreme ultraviolet spectrometer

The undulator consists of three 0.5 m sections, of 22 periods each, and has a periodicity of $\lambda_U = 2.2$ cm. The wiggler parameter, k, is k=1.25, which represents a maximum magnetic field value of +/- 0.6 T on axis. Following the undulator, the electrons are deflected using a secondary magnetic spectrometer (Spectrometer 2), and the spontaneous undulator emission is sent to an extreme ultraviolet (XUV) spectrometer, which is setup to resolve spectra around 100 eV.

The XUV spectrometer consists of a variable-width entrance slit, a focusing grating or a transmission grating, and two dual-stacked micro-channel plates (MCPs). The focusing grating is concave with varying line spacing to focus the 0th and 1st order undulator spectrum onto each respective MCP. With a photon resolution of 0.1 nm, calibrated at 73 eV, the XUV spectrometer has a resolution below 1% of relative electron energies.

3.5 Effect of emittance and energy spread on XUV spontaneous emission spectrum

For an idealized electron beam with zero emittance and energy spread only one electron energy would be present to produce spontaneous emission at wavelengths according to the undulator equation (Eq. 3.29).

$$\lambda = \frac{\lambda_U}{2\gamma^2}\left(1 + \frac{K^2}{2} + \gamma^2\theta^2\right) \tag{3.29}$$

The spectrum of a mono-energetic electron bunch would consist of thin peaks at the fundamental undulator wavelength and its harmonics. However, zero percent energy spread and emittance is not realistic, so using the computer code SPECTRA, the effects of energy spread and emittance can be modeled.

With a realistic energy spread, the width of the thin spectral peaks will become finite due to the presence of different electron energies in the beam. This causes the thin spikes at the undulator harmonics to broaden. Since the energy spread contains electrons above and below the fundamental wavelength, the broadening of the emission spectrum happens on both the positive and negative sides of the fundamental orders. The uniform broadening

of the emission spectrum is directly correlated to the energy spread within the electron beam [4].

The geometric emittance of the electron beam has two separate effects on the XUV spectrum [4]. First, the emittance of the electron beam causes some electrons to travel at an angle with respect to the axis of propagation. This decrease in on-axis velocity reduces the relativistic gamma (γ) term in (Eq. 3.29), leading to the emission of photons at larger wavelengths. Because the emittance can only reduce the on-axis velocity, this effect leads to a broadening of the emission spectrum only in energies lower than the fundamental. Emittance can therefore be obtained from measuring the asymmetric broadening of the fundamental harmonic orders (Fig. 3.3).

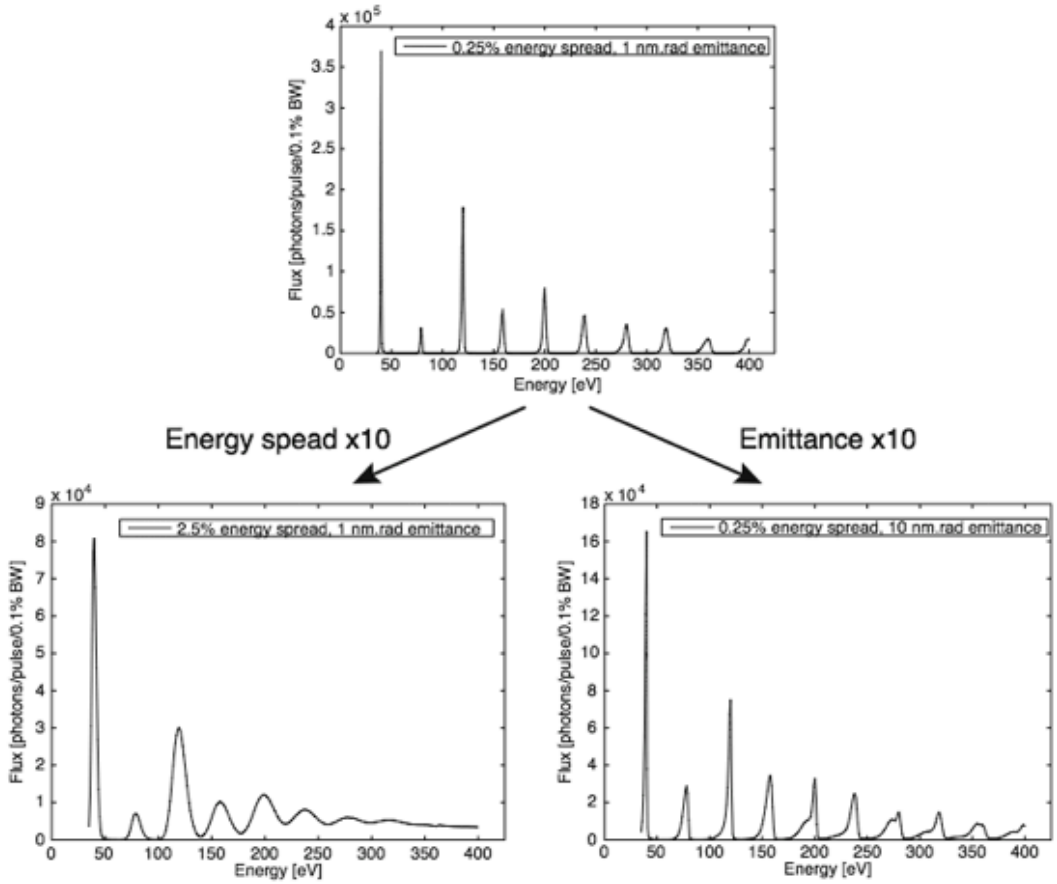

Figure 3.3: Effects of energy spread and emittance on the spectrum of spontaneous undulator radiation, with the spectrum measured on the axis of propagation. As energy spread increases, the emission spectrum broadens uniformly about each fundamental harmonic order. The increase in the geometric emittance causes an asymmetric broadening of the spectrum in the lower energy spectrum due to a decrease in on-axis velocities. Also, with off-axis electron trajectories, the on-axis flux of the even orders grows while the odd orders flux decreases. Image reproduced from Ref. [4].

Emittance also affects the ratio of the flux in even and odd orders. Since undulator

emission is directional, with odd harmonics emitted on-axis and even harmonics off-axis, the emittance will change the ratio of even and odd order flux on-axis. With a detector on axis and near-zero emittance, the undulator's odd orders will have a much larger flux than even orders. However, as the beam emittance increases, electrons traveling at an angle with respect to the axis of propagation will now have their off-axis emission emitted along the axis of propagation. A detector on-axis will now see an increase in the even order's flux and a decrease in the flux of the odd orders. This increase in the ratio of even to odd order harmonic flux is directly correlated to the beam's emittance.

3.6 THUNDER undulator's first light

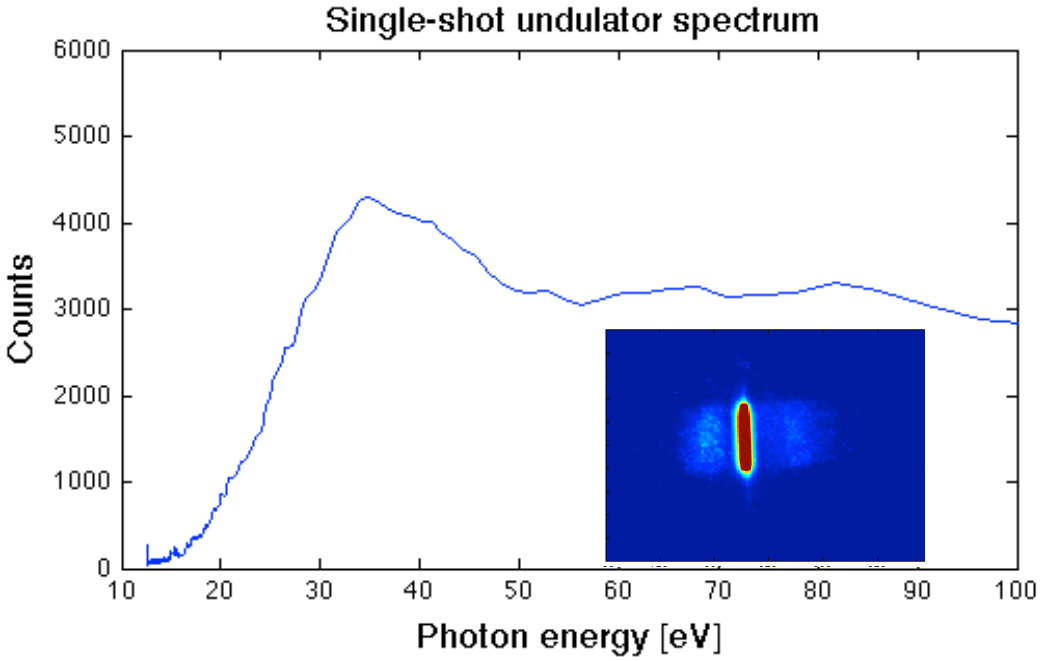

Figure 3.4: The spectrum of undulator emission from a 400MeV beam with energy spread and emittance much larger than those modeled using SPECTRA. The raw spectrum is shown with the saturated 0th order, and the 1st order spectrum on both the left and right. Converting wavelength to photon energy, the plot shows the spectrum's corresponding photon energies.

The first step in characterizing the THUNDER undulator was taken using a 100 nm period transmission grating and concave mirror. Initial experiments on generating undulator radiation used 400 MeV beams with broad energy spread (35%). Such beams allowed for studies on beam focusing and are easy to produce. With a fundamental harmonic energy of 40 eV and this level of energy spread and emittance, the structure of undulator harmonics becomes smeared out. Though this does not provide the high-resolution diagnostic the

undulator is capable of, it did allow for the characterization of the undulator as a working beam diagnostic; providing single-shot data retrieval of the undulator spectrum. (Fig. 3.4).

3.6.1 THUNDER undulator's XUV spectrometer calibration

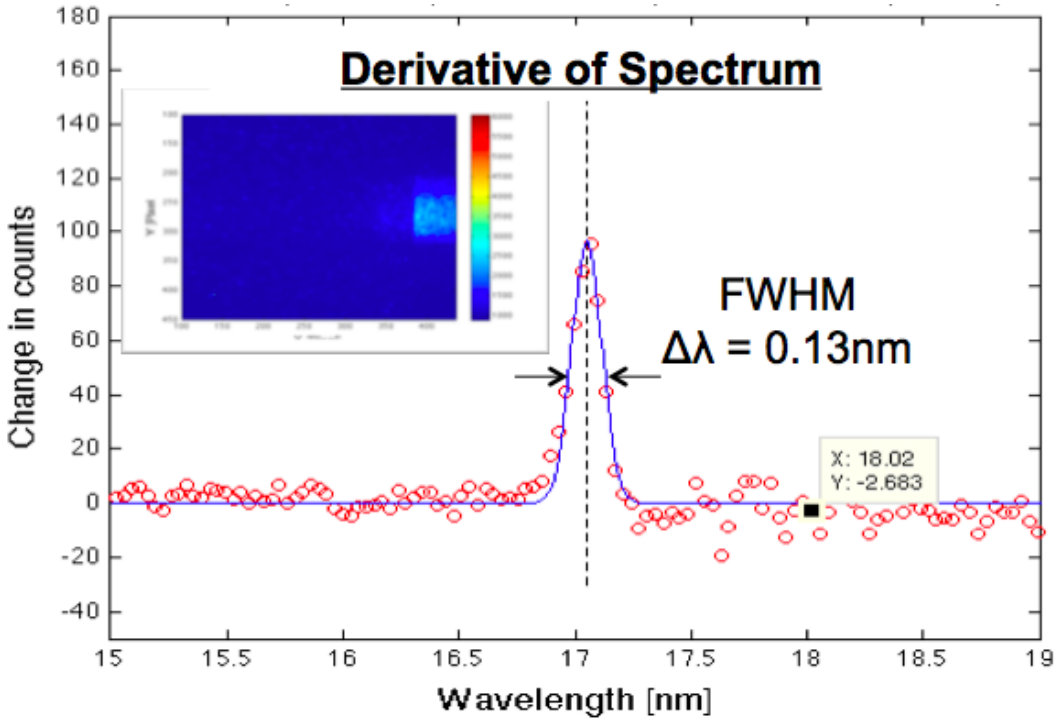

Figure 3.5: The raw undulator spectrum is shown is shown from broadband undulator radiation with an aluminum foil in the beamline with cutoff in transmission at $\lambda = 17$ nm. The gradient of the spectrum is plotted (red circles) and is fit to a Gaussian (blue line) peaked at $\lambda = 17$ nm. The width of the Gaussian is calculated to find the with of the drop in signal. This Gaussian width is used to determine the spectral resolution of $\Delta\lambda = 0.13$ nm.

After the characterization of the THUNDER undulator was completed with a low-resolution transmission grating, we replaced the curved mirror and transmission grating with the concave, focusing, reflective grating. This spectrometer design provides a higher resolution XUV spectrum, and produces a higher flux for the first order spectrum when compared to the transmissive grating. In order to produce ample counts on the MCPs, the slits on the spectrometer entrance remained fully open. Further improvements of the spectrometer resolution can be gained by closing the slit at the expense of signal level.

In order to calibrate the resolution of the XUV spectrometer, and in turn the electron energy resolution, a 200 nm thick aluminum foil was placed in front of the grating. The strong Al absorption line at 17 nm provided a sharp cutout in the undulator spectrum. By looking at the gradient of the spectrum (Fig. 3.5), the absorption line provided a spectral

cutoff 0.13 nm wide. This resolution at 17 nm (72 eV) corresponds to a resolution below 1% in energy spread [5].

3.7 Summary

In this chapter, the design of the THUNDER undulator, along with the spontaneous emission spectra of the first light and the calibration undulator have been presented. As a next step, we plan to produce beams of much lower energy spread (on the order of 5% and below) in order to benchmark our simulations and improve the diagnostic. The understanding of the spontaneous emission spectrum allows for high-resolution diagnosis of the electron beam's energy spread and emittance values. This high level of resolution is crucial in order to further diagnose electron beams, as LPA technologies continue to grow. Also, these high-quality diagnostics will play a crucial role as future undulator applications rely on sub-energy spread, such as an LPA based FEL.

Chapter 4

A Tape-based High-Harmonic Generating Seed for LPA-based FELS

Surface high-harmonic generation (SHHG) from a tape is experimentally studied. By operating at mildly-relativistic normalized laser strengths $a_0 \leq 0.2$, harmonics up to the 17^{th} order are efficiently produced in the coherent wake emission (CWE) regime. CWE pulse properties such as divergence, energy, conversion efficiency (CE), and spectrum, are investigated for various tape materials and drive laser conditions. A clear correlation of surface roughness and harmonic beam divergence was found. At the measured pulse properties for the 15^{th} harmonic (conversion efficiency $\sim 6.5 \times 10^{-7}$ and rms divergence $\sim 7 - 14$ mrad), the 100 mJ-level drive laser at 40 fs produces several MW's of extreme ultra-violet (XUV) pulses. The spooling tape configuration enables multi-Hz operation over thousands of shots, making this source attractive as a seed to the few-Hz LPA-driven free-electron laser (FEL). The results of a 1D FEL simulation code, GINGER, indicate that these CWE pulses with MW level powers are sufficient for seed-induced bunching and FEL gain.

4.1 Introduction

Intense coherent light sources in the extreme ultraviolet (XUV) domain (wavelength ∼10-120 nm) have applications which span material science, atomic and molecular optics, single-shot diffraction studies, and non-linear X-ray optics [42]. Two approaches towards the production of such ultra-short pulses are the electron-beam-driven free electron laser (FEL) and laser-driven high-harmonic generation (HHG). For example, the FEL facility FLASH in Hamburg, Germany, can deliver 100 μJ-level XUV pulses at sub-picosecond pulse durations leading to GW peak powers [43].

One challenge limiting the availability of high-power XUV sources is the intrinsic losses in reflectivity and transmission of XUV optics. A traditional laser oscillator cavity would not have the efficiency needed to maintain or amplify the XUV pulses. A common approach for intense XUV pulse production is laser-production of harmonics of the fundamental frequency.

At conversion efficiencies (CE's) of order 2×10^{-6} (described in Ref. [44]) it would take a 100 mJ-level laser system to produce XUV pulses of MW peak power (transport losses are neglected).

The most common experimental scheme for HHG is to interact a laser pulse with an underdense (gas-based) target [45]. This HHG scheme requires the ionization potential of the gas species to be close to the laser intensity. A fs-class 100 mJ-level laser system forces the use of focusing optics with an f-number of order 10^3 or greater. Such a weak focusing geometry combined with the accompanied transport losses (of order 80-90% for a few optics at 50% loss each) form a major challenge to a practical compact high-power XUV source. Optics within meters of the source would simply succumb to laser damage.

Solid-surface high-harmonic generation (SHHG) [35, 46, 47, 48, 49, 50, 51, 52, 53, 54, 55, 56] relies on full target ionization prior to arrival of the peak of the laser pulse, hence requiring a drive laser at intensities $\geq 10^{16}$ W/cm^2. This intensity regime lends itself to higher laser energies, shorter focusing optics, but often at lower repetition-rate, reduced stability, and larger divergence. Nevertheless, with a CE comparable to gas-based HHG, SHHG can produce XUV pulses at > 1 MW-levels using 100 mJ-level 40 fs laser pulses.

As will be extensively discussed in this chapter, we propose that SHHG could be used as a compact seed source for an XUV FEL [57]. With tighter focusing optics and the thin tape acting as both the SHHG source as well as the XUV/e-beam combiner, this setup would eliminate XUV transport optics and simplify the experimental configuration.

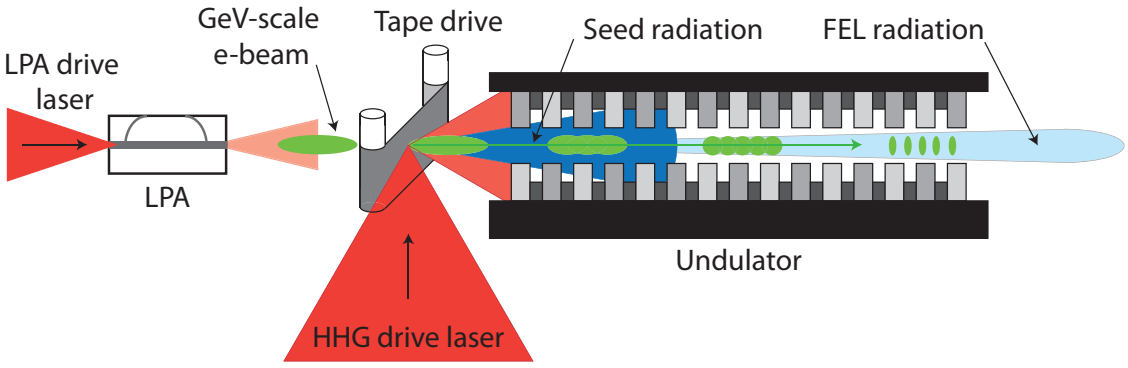

Figure 4.1: Schematic of the integration of the tape-based HHG source with an LPA-driven undulator. The intrinsic synchronization of the e-beam and HHG pulses, as well as the elimination of an HHG transport line, allow for MWs HHG pulses to initiate FEL lasing.

In an XUV FEL, a relativistic electron beam passing through an undulator uses XUV radiation to produce coherent gain. The periodic magnetic structure of the undulator oscillates the electron bunch, which producing radiation along the propagation axis. Without using an external source to seed the FEL, the electrons are initially incoherent and each radiate light which has an effect on the electrons upstream. FEL's can generate coherent radiation via self-amplified spontaneous emission (SASE), where during undulator propagation an electron beam self-bunching instability grows, leading to the transition from incoherent spontaneous

emission from unarrangned electrons, to coherent radiation from stimulated emission of electrons which are arranged in micro-bunches separated in space by the FEL wavelength [58]. The self-bunching process can be initialized (and stabilized) if a seed pulse at the resonant wavelength is co-propagating with the electron beam in the undulator. Recent efforts worldwide have focused on combining both HHG and FEL technology by configuring the FEL to amplify the incoming coherent XUV pulses [59, 60, 61]. Such a seeded FEL configuration would reach saturation over shorter undulator lengths, with improved stability and coherence properties.

Underdense HHG sources [62] have been primarily considered as FEL seed due to the gas target's intrinsic replenishing nature. Indeed, for a solid-surface HHG (SHHG) source, the target (typically a polished mirror) needs replacement or repositioning after every laser shot, limiting the repetition rate and experimental life time. However, equivalent CE's at much larger laser energies make SHHG sources attractive as a high-power XUV source.

Borot *et al.* [63] enabled a higher repetition rate by applying a rotating glass mirror. Here we present a novel solid target configuration based on a tape, allowing for hundreds of meters (5 mm between successive shots) of solid target to be spooled through the laser focus, allowing for over 10^5 shots on target before needing to change tape. Such a source could be applied to seeding an FEL. By placing the tape right at the undulator entrance, losses and aberrations from HHG beam transport optics are eliminated, while the electron beam propagates through the thin (<10 micron) tape, overlapping with the HHG beam inside the undulator [57]. This compact configuration for HHG could be paired with a compact LPA [3], operating at a few Hz repetition rate. The high-intensity laser driving the LPA and the moderate-intensity laser driving the tape-based SHHG source could be derived from a single laser system, offering intrinsic synchronization between the electron beam and SHHG seed radiation. Such a configuration is depicted in Fig. 4.1. Development of compact LPA-driven FELs is an area of active research [60, 64, 65]. LPA electron beams have been used to produce incoherent undulator radiation in the visible [66] and soft x-ray [67] wavelength regimes. Application of the Berkeley Lab LPA to generation of incoherent and coherent (gas-based HHG seeded FEL) radiation can be found in Refs. [5] and [68], respectively.

SHHG from overcritical plasmas has received great interest over recent years (see [35, 49, 69] and references therein). Though the accepted nomenclature of surface high-harmonic generation, or SHHG, may imply harmonics are created from a laser-solid interaction, it is in fact the interaction of the laser pulse with an overdense plasma (following a laser produced surface ionization), which creates a laser-plasma interaction leading to the collective effects governing harmonic generation. Different emission mechanisms have been isolated: at relativistic normalized intensities of $a_0 > 1$), the highly non-linear relativistic oscillating mirror (ROM) regime has extensively been studied [70, 49, 69, 71], while at sub-relativistic intensities ($a_0 < 0.2$) a more quasi-linear regime referred to as the coherent wake emission (CWE) regime was identified [52, 53, 54, 47, 46, 55, 72]. For the studies described in this chapter (and for the proposed seeded-FEL application), the CWE regime was chosen due its quasi-linear intensity scaling (enhancing shot-to-shot stability), the availability of up to 100 mJ in 40 fs in the seed's drive laser of our FEL design, and the contrast levels present in the

TREX laser system.

The outline of this chapter is as follows: we will first present theoretical foundation of SHHG. Both SHHG produced from laser intensities in the relativistic regime (known ROM harmonics), and in the sub-relativistic regime (CWE harmonics) are explained. Next, the experimental setup for the tape-based CWE campaign is discussed along with relevant details of the experiment, including tape roughness and detector calibration. The experimental characterization of CWE pulses includes the spectral analysis, spatial/divergence analysis, and absolute flux derivation. At the 15^{th} harmonic-order conversion efficiencies of 5-7$\times 10^{-7}$, MW pulses are produced at 7-15 mrad (rms) divergences. We conclude with the integration of the experimental seed parameters and an FEL model, and show that strong electron bunching is expected for the presented parameters.

4.2 Harmonic generation from solid surfaces

The two mechanisms that have been identified for harmonic generation by interacting high intensity laser pulses with solid targets are ROM and CWE harmonics. These SHHG techniques have been understood since the 1980's [23, 73] and are have recently been shown experimentally [35, 74] with the availability of highly-intense laser pulses. Due to the strong electric field of a relativistic laser pulse, ROM is based on the reflection of the incident laser pulse from a plasma at critical density oscillating at velocities near the speed of light. The CWE harmonics mechanism uses plasma waves excited by Brunel electrons in a plasma density gradient. Once absorbed, the electrons undergo subsequent mode conversion from plasma waves to electromagnetic waves. Each of the two processes has very different properties. The most trivial difference of the harmonic generating mechanisms is the intensity range in which they are generated. CWE occurs at sub-relativistic intensities with $a_0 < 1$, and ROM occurs for relativistic laser pulses and dominates the harmonic mechanism when $a_0 > 1$.

4.2.1 Coherent wake emission

In contrast to the ROM harmonics, coherent wake emission (CWE) is a bulk process. Thus, harmonic orders are generated inside the bulk plasma target. Bunches of electrons (Brunel electrons) are first pulled out of the plasma by the laser's electric field component perpendicular to the target surface. Note that p-polarization is required for this first step to occur. Following being pulled from the plasma, when the electric field flips, the electrons are accelerated back towards the plasma gradient. As electrons propagate through the density gradient, they pass through the critical density surface and are no longer affected by the laser pulse's electric field. Beyond the critical surface the electrons propagate and excite plasma waves in their wake. These plasma waves undergo linear mode conversion [16] and radiate electromagnetic waves. This process is essentially inverse resonance absorption [75].

It should be noted that CWE harmonics can only be generated in plasmas that have a gradient length of order $\lambda/100$ to $\lambda/10$ [35].

The highest producible harmonic order for CWE depends on the properties of the target material which is used. Since the Brunel electrons are creating a wake and linear conversion occurs based on the local plasma density, the highest frequency which can be emitted is that of the highest possible plasma density. This gives rise to the equation for the cutoff order q_{cutoff}:

$$q_{cutoff} = \sqrt{\frac{n_{max}}{n_{crit}}} \tag{4.1}$$

where n_{crit} is the critical density based on the frequency of the input light and n_{max} is the density of electrons in the solid material used to produce the plasma.

For typically used target materials, q_{cutoff} lies between 15 for low-density plastics, 20 for BK7-glass or fused silica, and metal targets which can produce 25+ order for a drive laser at $\lambda = 800$ nm. However, the highest produced harmonic is based on many factors, such as the intensity of the driver pulse, the pulse contrast, the surface quality of the solid target, among others. The dependence of the spectral cutoff for CWE harmonics has been shown in Ref. [50, 76, 77].

To evaluate the physics behind the mechanism of CWE, we first look at the linear density gradient of length L over which the electron density in the target rises from zero to n_{max}. The density as a function of position x can then be written as

$$n_e(x) = \frac{x}{L} n_{max}. \tag{4.2}$$

The position within the gradient at which each different frequency of light is produced is given by the localized plasma density at a given depth x. Since the plasma frequency is proportional to localized electron density ($\omega_p \propto n_e^{1/2}$), the position x(q) inside the gradient at which the harmonics order q is generated is given by [77]

$$x(q) = \frac{L n_{crit} q^2}{n_{max}}. \tag{4.3}$$

The discussion of CWE harmonics in this chapter shows that CWE has unique properties which can be distinguished from ROM harmonics. Mainly that the highest achievable harmonic is determined by the maximum density of the target. This limits the spectral range to harmonics up to $\lambda \sim 40$ nm for commonly used BK7-glass targets. There is no universal spectral roll-off [50, 76, 77].

4.3 Experimental setup

As depicted in Fig. 4.2, laser pulses from the BELLA Center's TREX [12] laser system (central wavelength 803 nm +/-5 nm) were focused by a 2 m focal length parabola to a spot size of 23.0 μm. The Strehl ratio was measured to be 0.73, and the pulse duration was τ_0=48

fs (intensity FWHM). The energy on target was measured with calibrated energy detectors, and was varied from several mJ's to over 300 mJ. For a laser energy on target of 70 mJ, this yielded a peak intensity of 1.8×10^{17} W/cm^2 ($a_0 = 0.29$).

The laser pulse contrast was optimized with an XPW [34], with the contrast after amplification measured by a 3rd-order cross-correlator. A fit to the cross-correlation is shown in Fig. 5.13. The laser pulse can be described as having a 5-ps-long pulse pedestal during which the contrast increases from 1×10^{-8} relative intensity (the amplified spontaneous level) to 1×10^{-4} relative intensity.

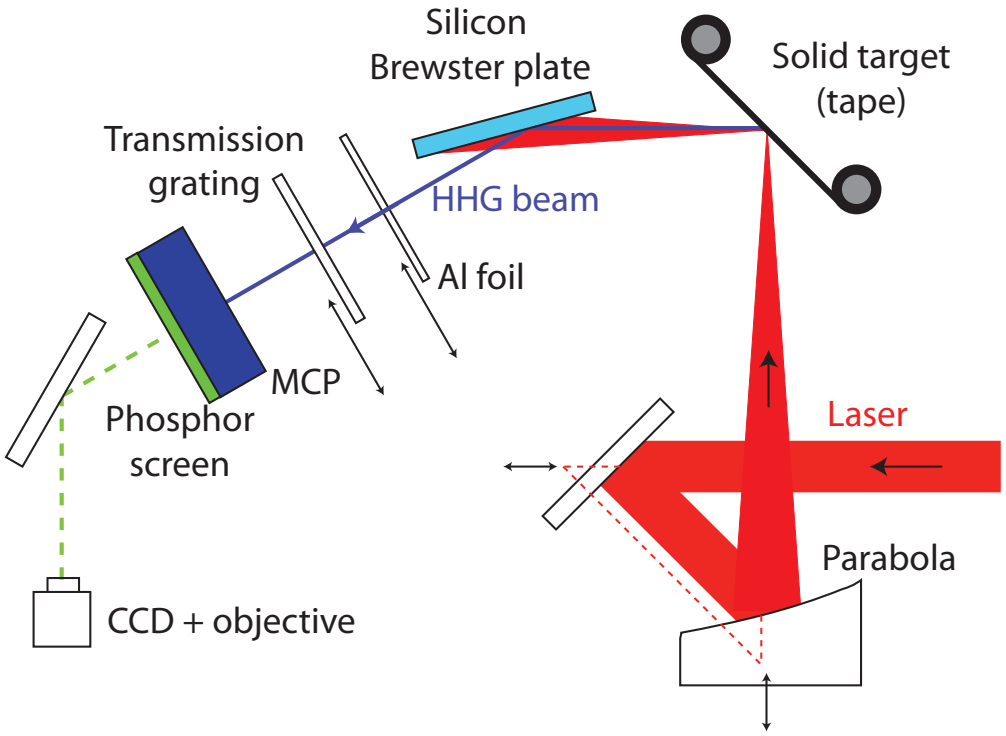

Figure 4.2: Schematic representation of the experimental setup for the generation of CWE pulses and their characterization. A 100 mJ-level laser is focused onto a thin tape, with the surface-generated harmonics propagating to an MCP-based detection setup.

The focal position with respect to the tape surface was varied by two coupled translation stages (parabola and steering mirror), see Fig. 4.2. A detailed description of the tape materials and mechanics of the tape drive is described in Chapter 5. The tape was moved in incremental steps of ∼1 cm between laser shots. The reflected laser, together with the surface-produced harmonics propagated to a silicon mirror at 74.9° with respect to normal (Brewster angle for 800 nm light), where the bulk of the laser energy was absorbed.

The spatial profile of the XUV light was measured by a phosphor-backed micro-channel plate (MCP) covering an observation angle of 88 mrad. Insertion of a 200-nm-thick aluminum foil and/or a 100 nm period transmission grating was possible, allowing for both angular

intensity and spectral characterization. The transmission grating (described in Ref. [78]) contained free-standing silicon nitride line pairs covering an area of 1.1×4.7 mm^2 with added horizontal support bars every 5 μm. The 575-nm photons from the phosphor screen were imaged onto a 10-bit (effective range) CCD camera.

4.3.1 Tape materials and surface quality

The CWE performance from three tapes was compared to a polished glass substrate. The tape materials were Mylar (thickness 24 μm), the magnetic-recording side of VHS (1.5 μm thick iron-oxide layer on a 13.5 μm thick Mylar substrate), and Kapton (thickness 9 μm)[1]. The iron-oxide layer of the VHS tape is mixed in with a bonding material following a $\sim$50/50% volume ratio.

Previous studies have focused mainly on the role of roughness in production of ROM harmonics. Rykovanov *et al.* [79] showed through simulations that under sufficiently strong laser intensities the roughness can get smoothed. Dromey *et al.* [80] indeed confirmed the limited or absent impact of roughness on ROM divergence. In Dromey's work, the roughness was expressed as a sample averaged standard deviation.

While the mechanics of ROM surface denting can be used to directly determine pulse divergence, pulses generated using CWE depend on the intrinsic emission phase across the 2D interaction area. Since the interaction of the drive laser with a spatially non-uniform solid surface governs the spatial phase, the roughness values of the tape will be used to parametrize the material's surface properties, and in turn influence the divergence of the generated CWE pulse.

Here we will discuss the impact of roughness on CWE harmonic divergence (at lower laser intensities than for ROM), with the roughness analyzed explicitly in terms of its spatial-frequency spectrum. It will be shown in Sec. 4.4.2 that an experimental correlation between roughness and CWE divergence clearly appears.

For an arbitrary surface of height distribution $h(x, y)$, it is most common to discuss the surface properties in terms of the profile at a given spatial frequency. The measurement of $h(x, y)$ is typically a discrete 2D array $h_{m,n,}$ with $M \times N$ number of pixels at physical size Δx and Δy for the tangential and sagittal directions, respectively. In the Fourier domain the 2D power spectral density (PSD) function $S_2(l, \kappa)$, with l the tangential and κ the sagittal spatial frequency, is then defined as [81] $S_2(l, \kappa) = MN\Delta x\Delta y|F_{l,\kappa}|^2$, with

$$F_{l,\kappa} = \frac{1}{MN}\sum_{m=0}^{M-1}\left[\mathrm{e}^{-2\pi\imath ml/M}\sum_{n=0}^{N-1}h_{m,n}\mathrm{e}^{-2\pi\imath n\kappa/N}\right]. \tag{4.4}$$

The estimates for the 1D two-sided tangential (positive and negative frequencies) PSD $S_1'(l)$ and sagittal PSD $S_1'(\kappa)$ are obtained by integrating over rows (κ) and columns (l), respectively. These are then converted to 1D one-sided (positive frequencies only) PSD's $S_1(l)$

[1]Mylar is the brand name for a stretched film made of polyethylene terephthalate (PET), while Kapton the brand name for DuPont's polymide film with chemical name poly(4,4'-oxydiphenylene-pyromellitimide).

and $S_1(\kappa)$ by multiplying the 1D two-sided PSD's by $\times 2$. Note that these concepts are extensively discussed in Ref. [81].

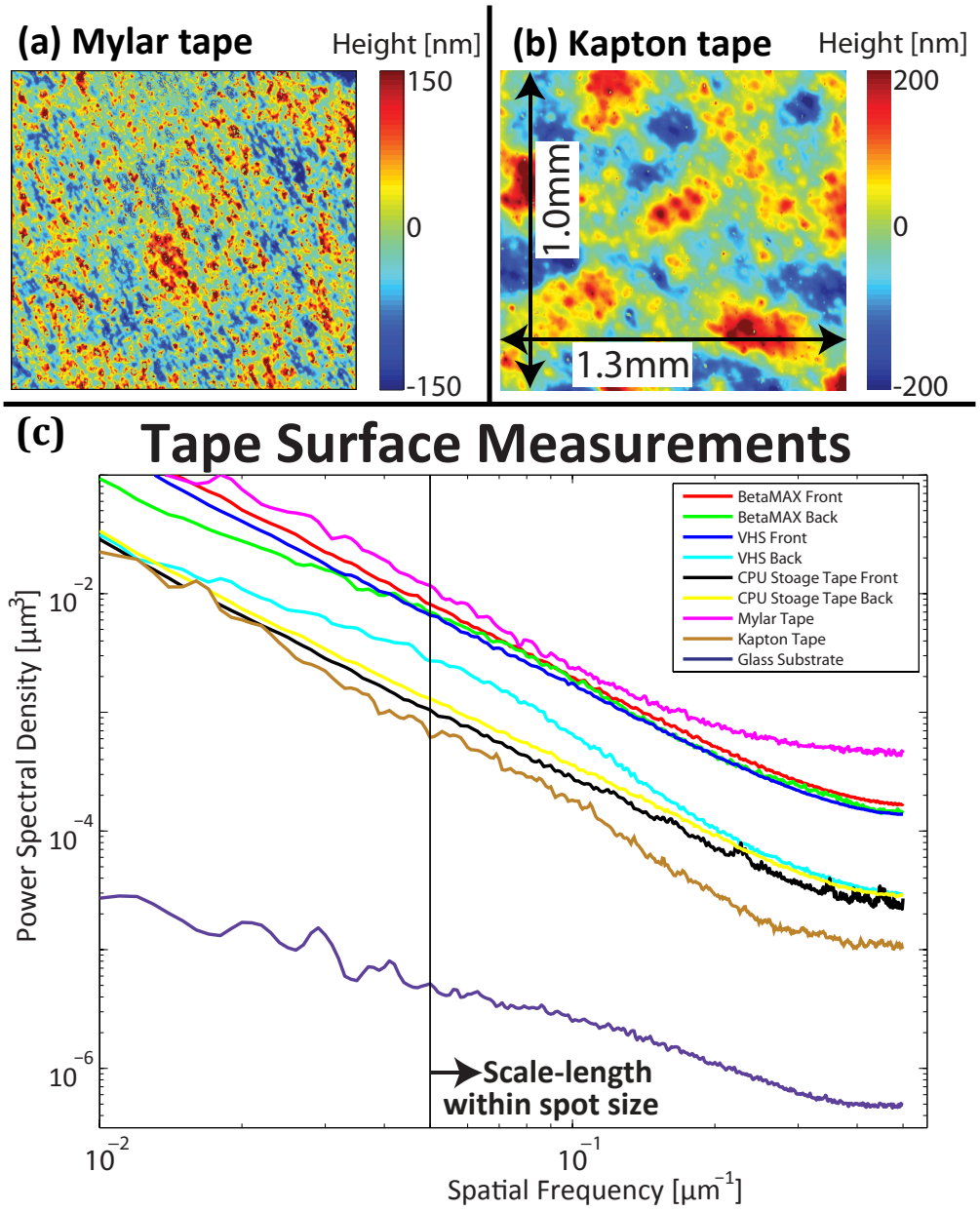

Figure 4.3: Measured surface profiles for the (a) Mylar and (b) Kapton tape. From the raw measurements (a) and (b), the 1D one-sided power spectral density was calculated (averaged over the tangential and sagittal planes), shown in (c). The polished glass substrate has the smoothest surface, while for spatial frequencies above 0.02 μm^{-1} (corresponding to spatial wavelengths below 50 μm) Mylar, Betamax and VHS tapes are rougher than the Kapton tape and the computer storage tape.

We have performed measurements on the surface roughness in two spatial frequency ranges. The first measurement was performed with a interferometric microscope (MicroMap Corporation, MicroMap-570), capable of measuring the surface distribution at spatial frequencies below a few μm^{-1} depending on objective selection [81]. Such a detection range is ideal to study the surface quality for spatial structures ranging from ~ 1 μm to larger features of the order of the laser spot size (few tens of microns). Figures 4.3(a) and (b) show the spatial profiles obtained with a 5× objective for Mylar tape and Kapton tape. The average of the 1D one-sided PSD in both tangential and sagittal planes for each substrate is shown in Fig. 4.3(c). Note that no corrections for the instrument response and resolution were made [82, 83]. One can see that the polished glass substrate is the smoothest substrate. Both the VHS tape and the Mylar tape are significantly rougher than the Kapton tape for spatial frequencies > 0.02 μm^{-1} (spatial wavelengths < 50 μm). The relevance of these findings will be addressed in the experimental discussion of Sec. 4.4.2.

A second roughness related measurement was performed at the soft X-ray beamline (beamline 6.3.2) at the Center for X-ray Optics (CXRO) at the Advanced Light Source (ALS) in Berkeley, California (details online[2]). At the ALS, monochromatic light was delivered onto a tape at the desired wavelength. The energy in the reflected beam was measured by a photo-diode downstream of the tape. When operated at grazing incidence angles ($> 80°$ with respect to the surface normal), the reflectivity measurement in this configuration is dominated by the energy loss due to scattering of surface fluctuations at spatial frequencies above the inverse XUV wavelength $> 1/\lambda$ (discussed in Ref. [81]). Under these assumptions (also referred to as the Nevot-Croce regime [84]), the surface roughness can be described by a single roughness parameter σ. The database of CXRO (available online[3]) incorporates a choice for σ in order to adjust the reflectivity, with the roughness-adjusted reflectance $R(\lambda)$ expressed as

$$R(\lambda) = R_0(\lambda)\ \exp\left[-\left(\frac{4\pi\sigma}{\lambda}\right)^2 n_i n_t \sin\theta_i \sin\theta_t\right], \tag{4.5}$$

where $R_0(\lambda)$ is the reflectance from a smooth surface ($\sigma = 0$), and $n_{i,t}$ and $\theta_{i,t}$ are the refractive index and angle of incidence of the incoming and transmitted beam [84] respectively.

The results for (a) the Mylar tape at 80°, (b) the iron-oxide side of the VHS tape at 80°, (c) the Kapton tape at 80°, and (d) the polished glass substrate at 82°, are shown in Fig. 4.4. Note that these are the same materials studied by the optical interferometer as shown in Fig. 4.3. We can see from Fig. 4.4 that also in this spatial-frequency regime, the glass substrate is the smoothest at σ=4 nm, followed by the Kapton tape at σ=8 nm, the VHS tape at σ=11 nm, and the Mylar tape at $\sigma = 13$ nm. As will be shown, the roughness of the material determines the SHHG pulse divergence.

[2] cxro.lbl.gov/als632

[3] henke.lbl.gov/optical_constants/mirror2.html

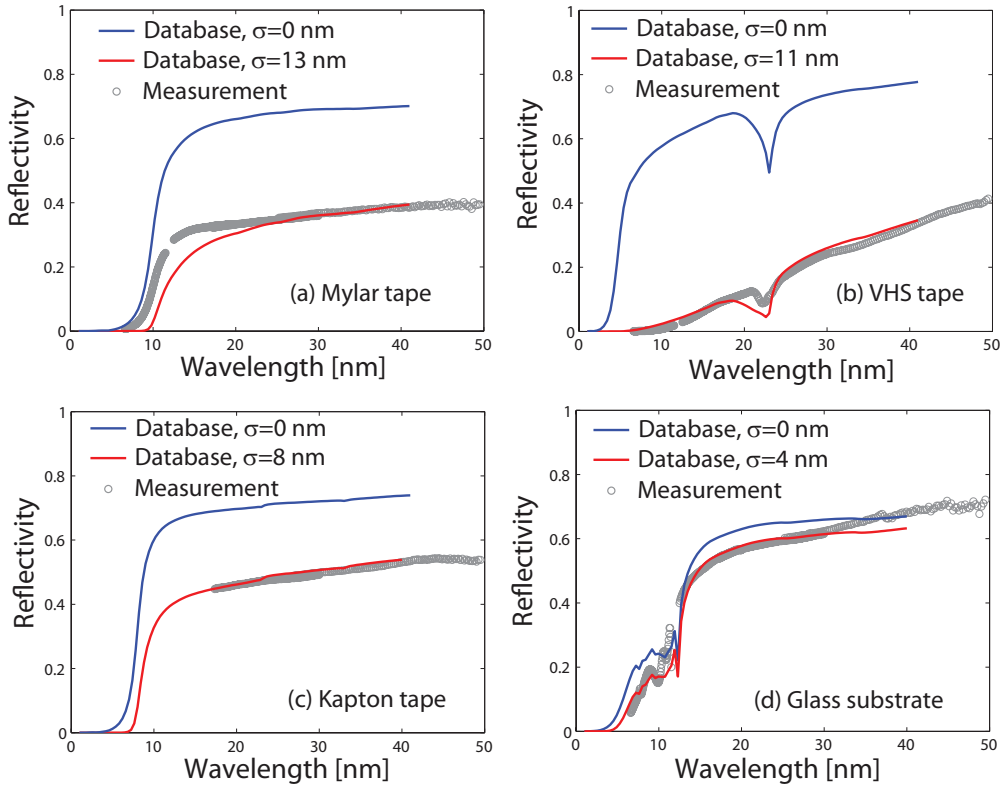

Figure 4.4: Plotted are the theoretical and measured grazing-angle reflectivity curves for (a) Mylar tape, (b) VHS tape, (c) Kapton tape, and (d) a polished glass substrate. The theoretical curves represent the values given by the CXRO database assuming no surface roughness (blue line), and a surface roughness value (σ) that best matches the measured reflectance values (red line). The reflectance values from each tape surfaces were measured at the ALS and are plotted at each wavelength (grey circles). Note that the database roughness parameter σ is physical only in a regime where the measurement is performed within the Nevot-Croce frame (i.e. where the relevant spatial frequencies are higher than $1/\lambda$).

4.3.2 Absolute calibration of XUV detector

As described in the setup discussion, the detection of the XUV photons was done by a phosphor-backed MCP (see Fig. 4.2). An f/1.4 objective, placed at 30 cm from the MCP/phosphor detector, enabled imaging of the spatial XUV profile at the MCP onto a 10-bit (effective) CCD camera. In order to obtain an absolute number for the XUV photons in a given harmonic, a calibration (XUV photons to CCD counts) is essential. A wavelength-dependent calibration was realized at the CXRO beamline at the ALS. Note that the ALS beam is free of higher-order grating reflections by means of foils and order suppressors, available at a wavelength range of ∼1-50 nm. A calibrated photodiode measured the absolute photon flux at a given wavelength, and the MCP/phosphor detector (under identical imaging conditions as in the CWE SHHG setup) measured the total counts. The resulting calibration curve of photons per count is shown in Fig. 4.5.

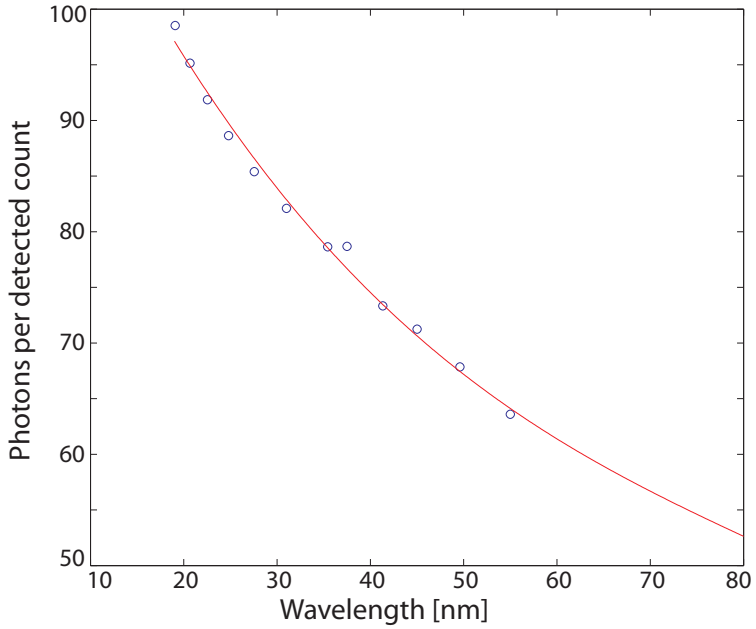

Figure 4.5: Calibration of XUV photons per CCD count from the MCP+Phosphor as measured at the ALS beamline. The calibration curve for wavelengths above 50 nm was obtained through extrapolation.

At the same ALS beamline, the wavelength-dependent reflectivity of the Brewster-angle silicon plate and the transmission of the 200-nm-thick aluminum foil, see Fig. 4.2, were recorded. The losses at a wavelength of 50 nm were 35% for the silicon plate and 40% for the aluminum foil.

4.4 Experimental results

The experimental results are divided into three sections: spectral measurements, spatial or divergence measurements, and absolute photon yield. An overview of the measured CWE parameters is presented in Table 4.1 at the end of this chapter.

4.4.1 SHHG spectral measurements

Figure 4.6(a) shows a typical spectrally-dispersed CWE image obtained from VHS tape. This image was obtained with the transmission grating, and aluminum foil in the beamline, while the focus was positioned 1 mm downstream of the tape surface. A 260 mJ pulse with pulse duration of 79 fs (chirped with ξ=1.32 following $\tau = \tau_0\sqrt{1+\xi^2}$), yielded a focal intensity of 2.8×10^{17} W/cm^2 ($a_0 = 0.36$). Even and odd harmonic orders up to the 18^{th} can clearly be observed. Note that the horizontal support bars of the transmission grating add secondary dispersion in the vertical plane as can been seen in the raw image in Fig. 4.6(a),

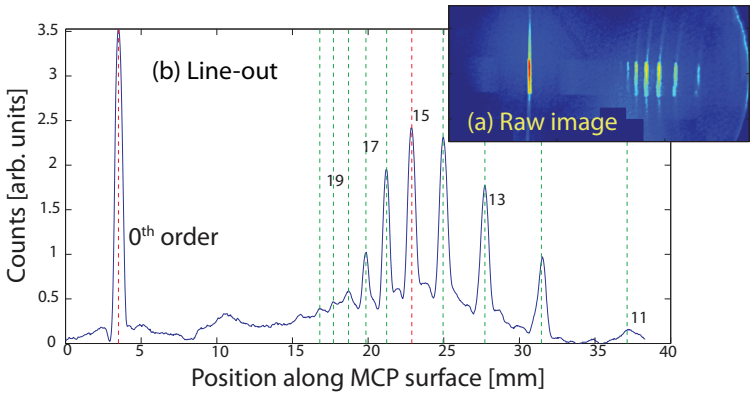

Figure 4.6: (a) A typical spectrally-dispersed spatial profile of CWE harmonics produced off the VHS tape (on-target laser energy of 150 mJ). A line-out is shown in (b). Even and odd harmonics up to the 18^{th} order are observed. The strong peak at the position of 3 mm is the 0^{th}-order transmission through the grating. The vertical bars represent the calibrated locations of integer harmonics. See Fig. 4.5 for the relative photons/counts calibration at each wavelength.

which was extensively described by Kornilov *et al.*[85] The spectral image was vertically averaged over the relevant region to form the line-out in Fig. 4.6(b). With the spectral calibration dictated by the grating and setup configuration, we used the drive wavelength λ as a variable to match the individual q^{th}-order harmonics (following λ/q). As seen from Fig. 4.6(b), the lines overlap with the observed harmonics of the drive laser's wavelength centered at 800 nm ($\sim$1% error in absolute spectral calibration), which is in agreement with the measured central wavelength.

A comparison between VHS tape, Kapton tape, and polished glass is shown in Fig. 4.7. The three spectra are representative of several successive shots, and were recorded under identical laser conditions. The laser energy was 70 mJ with a focal intensity of 1.8×10^{17} W/cm^2 ($a_0 = 0.29$). The glass produced a spectrum up to the 20^{th} order, which is consistent with the maximum density of $7.8{\times}10^{23}$ cm^{-3} and $q_{max} = \sqrt{n/n_{cr}} \simeq 21$ as described in the supplement of Thaury *et al.* [76] with $n_{cr} = 1.75 \times 10^{21}$ cm^{-3} the critical density for 800 nm light. The observed cut-off for both the VHS and Kapton tape was $\simeq 16$. Though the exact density is unknown for both tapes, their density is greater than that of pure CH plastics, which have a predicted cut-off at 15^{th} order. [76]

4.4.2 SHHG spatial profile measurements

By removing the transmission grating in front of the MCP (see Fig. 4.2 for the setup), the full spatial profile (and hence divergence) of the CWE beam was recorded. With the 40 mm diameter MCP placed 455 mm from the tape surface, the total observable angle was 88 mrad. The divergence of the CWE drive laser was 34 mrad (FWHM).

Representative images for the divergence off Mylar tape, VHS tape, Kapton tape, and

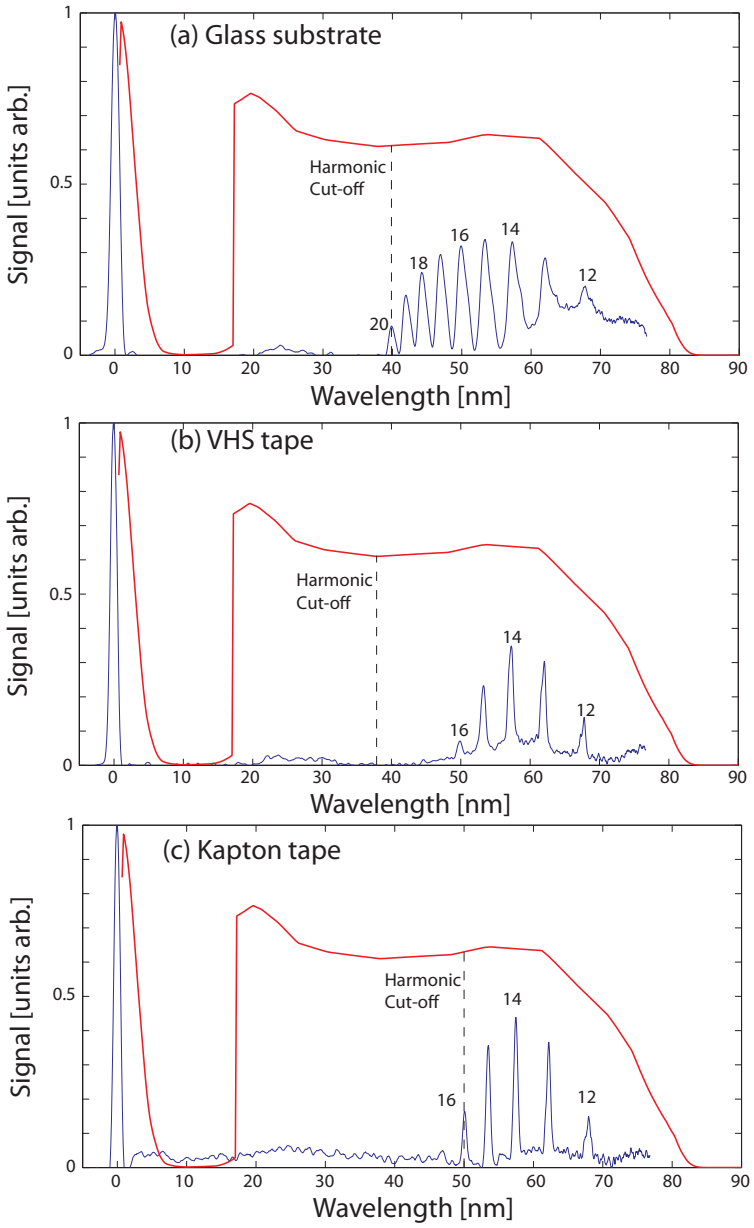

Figure 4.7: Representative CWE spectra off (a) a polished solid glass substrate, (b) the VHS tape and (c) the Kapton tape. All spectra were taken with an energy on target of 70 mJ. The red curve in the plots shows the transmission curve of the 0.2-μm-thick aluminum foil. The dashed black line shows the harmonic cut-off of each material [74]. See Fig. 4.5 for the relative photons/counts calibration at each wavelength.

a polished glass substrate, are shown in Fig. 4.8. The data was recorded under identical laser conditions as the CWE spectra in Sec. 4.4.1, with the drive laser energy of 70 mJ (intensity of 1.8×10^{17} W/cm^2 and $a_0 = 0.29$). With the aluminum foil in place, the spatial profiles represent a spectrally-integrated CWE beam size, covering orders 11 to 46.

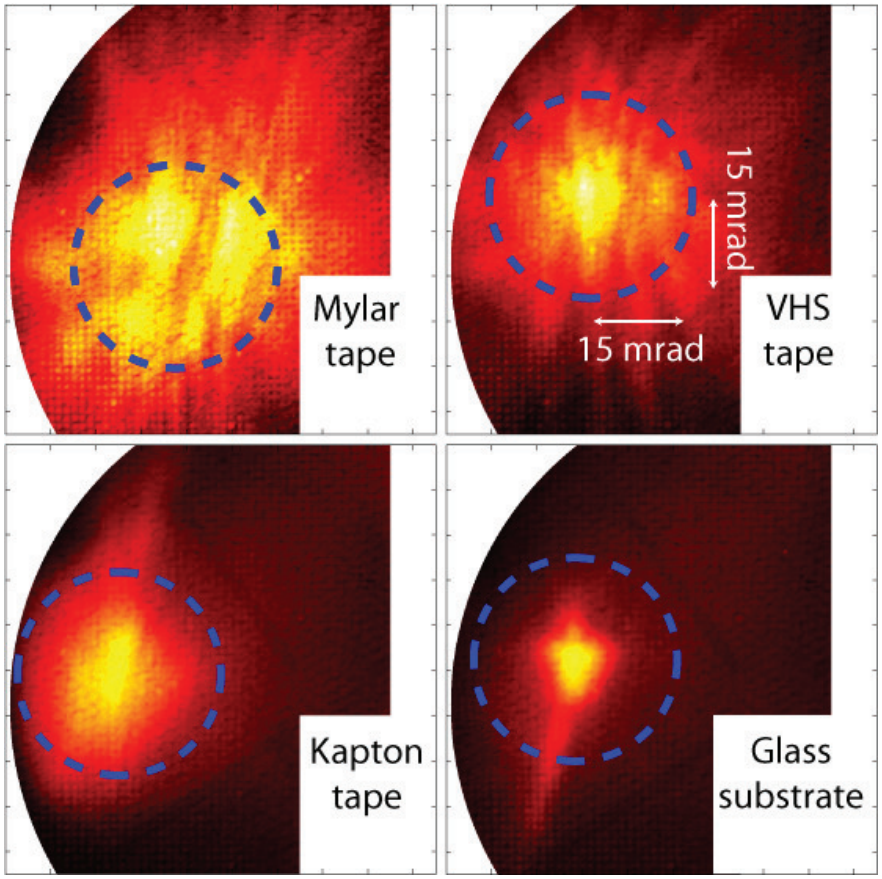

Figure 4.8: Spatial CWE pulse profiles for Mylar tape, VHS tape, Kapton tape, and the glass substrate. From these images the CWE divergence (integrated over orders above 11) was derived, ranging from 4 mrad (rms) for glass, to 7 mrad for Kapton tape, and 12 mrad for VHS tape, and 14 mrad for Mylar tape. The dashed blue line represents the beam size and divergence of the input IR beam [15 mrad (rms)].

Spectral dependencies on the divergence were not investigated during these experiments. The measured divergence was found to be correlated to the surface roughness measurements of Sec. 4.3.1.

The smoothest target was solid glass (see both Figs. 4.3 and 4.4), which yielded a roughness of 4 nm and divergence of 4 mrad (rms). Kapton, Mylar and VHS had measured roughnesses of 8 nm, 11 nm and 13 nm, respectively, using the Nevot-Croce method [84] (with relevant spatial frequencies above $1/\lambda$.) Using the power spectrum density in the Fourier domain of the 2D surface map yielded the same increasing order of materials from smoothest to roughest: glass, Kapton, VHS, and Mylar. The SHHG beams produced from these surfaces were ordered in the same way with increasingly larger divergences of 4 mrad, 7 mrad, 12 mrad, and 14 mrad, respectively (Fig. 4.8). Comparison between the Nevot-Croce roughness values and the rms beam divergences yielded a strikingly similar values with nearly a 1:1 ratio of roughness (nm) to divergence (mrad) [Table 4.1].

Other groups have typically used stronger focusing conditions ($f/\# < 5$) for the drive laser, with corresponding large CWE divergence angles of order 50 mrad or larger. [48, 80, 86] For similar focusing conditions as our setup ($f/\# > 20$), Thaury *et al.* measured a similar CWE divergence of 6 mrad (rms). [76] Both this experiment and Thaury *et al.* [76] produced XUV pulses from a glass substrate with a divergence about three times smaller than that of the drive laser, suggesting good transverse coherence of the target surface and an IR phase-front free of significant aberrations.

In order to demonstrate the shot-to-shot stability of CWE harmonics, nine successive images of the spatial profile from the VHS tape are shown in Fig. 4.9. The observed stability is consistent with the quasi-linear nature of CWE. [69] Table 4.1 of this chapter lists the standard deviation on the divergence and total counts, as well as the pointing fluctuations. All fluctuations are of few-% level, with the pointing fluctuations of order 0.2 mrad (few % of the divergence). For the proposed LPA-based FEL application, these fluctuations are well within the specifications required for the electron and seed beam overlap.

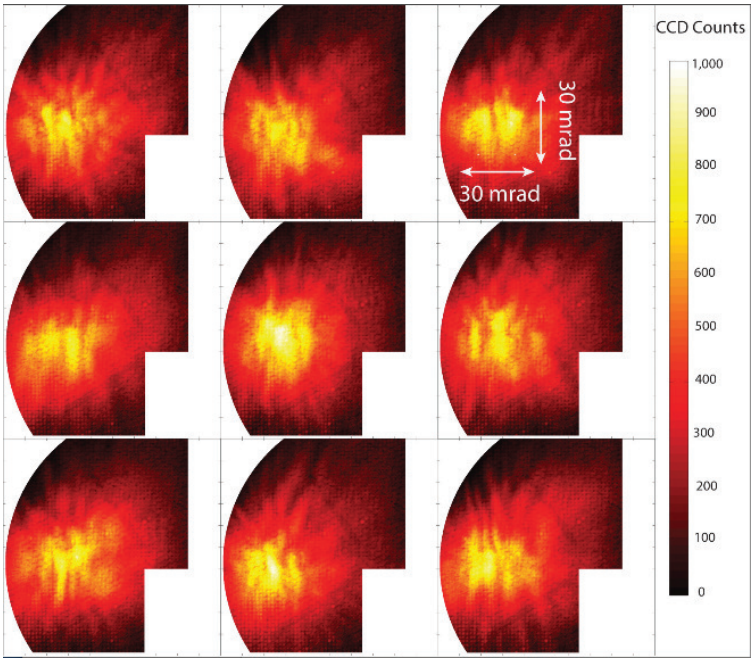

Figure 4.9: Nine sequential CWE spatial profiles measured off the VHS tape. Consistent with theory, we see excellent shot-to-shot reproducibility, due to the quasi-linear mechanism responsible for CWE emission.

4.4.3 Absolute photon flux

Another critical parameter to be determined is the CE for the 15^{th} order. From the spatial profiles (collecting the entire CWE beam), and with the ratio of counts in each harmonic order obtained from the spectral measurements, the total counts in the 15^{th} order

Table 4.1: Overview of measured CWE pulse parameters

Tape Material	Mylar	VHS	Kapton	Glass Substrate[5]
Thickness [μm]	24	15 (total)[4]	8.8	5000
Roughness (XUV reflectometry) [nm]	13	11	8	4
Roughness (PSD at 0.1 μm^{-1}) [μm^3]	4×10^{-3}	1×10^{-3}	1×10^{-4}	5×10^{-5}
CWE pulse divergence (rms) [mrad] [6] [7]	14	12	7	4
CWE pulse pointing fluctuation (rms) [mrad]	0.6	0.18	0.21	0.15
15^{th} order conversion efficiency	3.5×10^{-8}	6.5×10^{-7}	4.8×10^{-7}	2.9×10^{-8}
CWE pulse total counts fluctuation (rms) [%]	2.5	2.8	5.6	7.9

was estimated. Since the CWE beams were typically larger than the size of the transmission grating, the spectrum was only sampled near the center of the CWE beam (hence, a spectrally-dispersed CWE pulse divergence was not obtained). For the analysis presented in the next paragraphs, we will assume that the spectrum measured at the CWE pulse center is representative of the spectrum of the entire CWE pulse.

To convert counts to photons, the absolute detector calibration described in Sec. 4.3.2 and Fig. 4.5 was used. For VHS, beams of 11 mrad (rms) divergence were observed, with $\simeq$23% of the counts in the 15^{th} order, equivalent to 45 nJ of energy.

Using $\sim$70 mJ of IR light, the 15^{th} order conversion efficiency was 6.5×10^{-7}. Similarly, CE's for Kapton tape (CE= 5×10^{-7}), Mylar (CE= 3.5×10^{-8}), and the glass substrate (CE= 2.9×10^{-8}) were estimated. Although future efforts will focus on further enhancing the CE, these values are already of equal or higher value than measured by other groups (Borot *et al.* [63] measured a CE=3×10^{-8} for the 15^{th} order, while Easter *et al.* [86] measured a CE=2×10^{-7}, although under different drive laser conditions). At a CE=6.5×10^{-7}, note that this SHHG source offers a competitive advantage to gas-based systems. The SHHG laser focusing system is of length 2 meters versus >10 meters in gas-based HHG (distance from parabola to first post-focus optic). The long gas-based HHG length explains the limited number of labs pursuing high-peak-power gas-based sources (one exception is Midorikawa *et al.* [87]). Furthermore for the SHHG-seeded FEL application transport optics would not be necessary, providing a gain of order $\times$5-10 in on-target delivery (MW at the source translates to MW at the application). Also, the 10-mrad level divergence removes the shot-to-shot alignment sensitivity to overlap the seed with the e-beam.

4.5 CWE induced microbunching

The CWE source characterized in Sec. 4.4 has many potential applications due its high-power nature. One such application is as a coherent seed for an XUV FEL. In this application (see Fig. 4.1 for a schematic) the source of the CWE emission would be installed upstream of the undulator entrance without additional HHG transport optics. The divergence of the CWE pulse results in an intensity that rapidly decreases along the undulator. Despite this rapid reduction in radiation intensity, the CWE pulse can still strongly bunch an electron beam in the undulator, seeding the FEL.

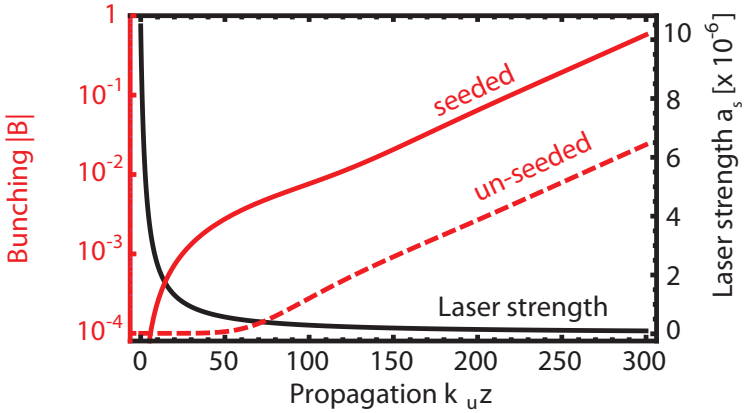

Figure 4.10: Bunching factor $|B|$ versus normalized undulator length $k_u z = (2\pi/\lambda_u)z$ with (solid red curve) and without (dashed red curve) seed radiation. Without seeding, initial bunching $|B(z=0)| = 10^{-4}$ was assumed. Also shown is the amplitude of the seed radiation intensity $a_s(z)$ (black curve).

For a given seed divergence, a corresponding source spot size w_{0s} can be defined through $w_{0s} = \lambda/(\pi\theta_{rms})$, with $\theta_{rms} = \theta_{FWHM}/\sqrt{8\ln 2}$ the divergence. The focus of the CWE will be located at position $z_F < 0$, with $z = 0$ the undulator entrance. For our proposed seeded-FEL configuration (see Fig. 4.1), the undulator entrance is many Rayleigh ranges z_{Rs} from focus (with $z_{Rs} = \pi w_{0s}^2/\lambda$). With $|z_F| >> z_{Rs}$, combined with the fact that we consider the electrons to be close to the propagation axis, we may approximate the seed field as a plane wave. The effects of seed wavefront curvature will be the focus of future studies. For a Gaussian beam, the z-dependent normalized field strength a_s is

$$a_s(z) = \frac{a_{s0}}{\sqrt{1 + (z - z_F)^2 / z_{Rs}^2}}. \tag{4.6}$$

[4] 15μm total = 13.8μm (Mylar substrate) + 1.2μm (magnetic coating of iron-oxide and bonder).
[5] Not a tape material.
[6] Shot to shot beam divergences fluctuate below 5% of the reported divergences values.
[7] All measured divergences were smaller than the drive laser's divergence of 15 mrad (rms).

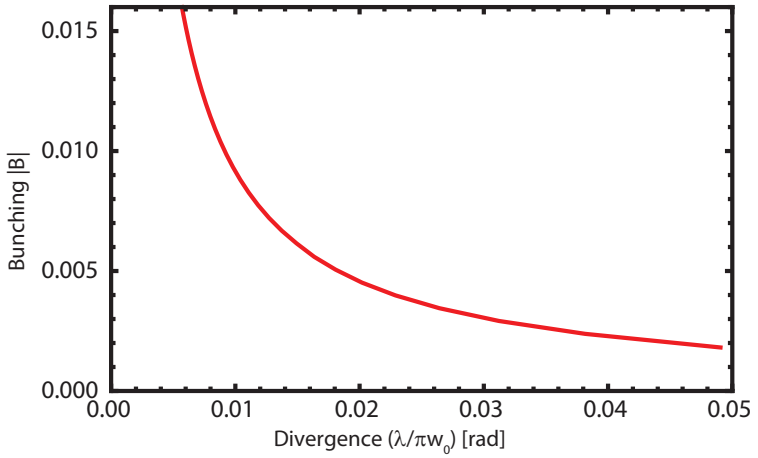

Figure 4.11: Bunching factor $|B|$ after 22 periods ($k_u z = 44\pi$) as a function of CWE seed divergence (with the seed power of 3 MW fixed). To achieve bunching above $|B| = 10^{-3}$, a divergence below 20 mrad rms is required. The measured integrated CWE pulse divergences are of order 7-15 mrad.

The peak strength a_{s0} is related to the seed energy W_s (filtered to include only the 15^{th} harmonic), pulse duration τ_s, and source size w_{0s}. We will consider parameters using our experimental observations and the proposed LBNL LPA-driven FEL design, [65] $\lambda_u = 2.18$ cm, $z_F = -1$ cm, $\lambda = 800/15 = 53.3$ nm, $\theta_{rms} = 5.7$ mrad (with $w_{0s} = 3$ μm and $z_{Rs} = 524$ μm), and 3 MW power (W_s=60 nJ in τ_s=20 fs), yielding $a_{s0} = 2 \times 10^{-4}$. A slightly smaller divergence is considered than the measured 8 mrad for the Kapton tape, since the 15^{th} order divergence is expected to be smaller than the spectrally-integrated divergence. A pulse energy of 60 nJ is consistent with measured CE's in the $5 - 7 \times 10^{-7}$ range for VHS and Kapton tapes,with >100 mJ drive laser energy available. The z-dependence on a_s is plotted in Fig. 4.10 as the solid black curve (note that the propagation distance z on the x-axis is normalized to $k_u z = 2\pi z/\lambda_u$). For this case, $a_s(z = 0) = 10^{-5}$ at the undulator entrance and decreases to $a_s = 10^{-6}$ after $k_u z = 8\pi$ (four undulator-periods). Note that further details of the CWE seed-induced microbunching model are discussed in Sec. 4.6. As Fig. 4.10 demonstrates, with the 3 MW seed present, the bunching is strongly accelerated and already reaches $|B| = 10^{-2}$ within 15 undulator periods ($k_u z = 30\pi$). So although the seed has a focus upstream of the undulator entrance (19 z_{Rs}'s) and has a divergence of 5.7 mrad (rms), its $a_s = 10^{-6} - 10^{-5}$-level field strength is still sufficient to induce and dominate bunching.

Figure 4.11 shows the effect of bunching after 22 undulator periods as a function of seed divergence. To achieve bunching $|B| > 10^{-3}$, a seed divergence below 20 mrad (rms) is required. Note that the bunching growth in any FEL (with or without seeding) will be strongly reduced for an e-beam with slice energy spread σ_γ/γ larger than the FEL Pierce parameter ρ.

4.6 CWE seed-induced micro-bunching model

In this section the basic steady-state FEL equations [58] are extended to include a seed radiation field that is rapidly evolving compared to FEL gain length [e.g., a strongly diverging CWE radiation field of the form Eq. (4.6)], and the initiation of bunching by the seed radiation in the exponential growth regime is examined. A plane wave model of the seed field is adopted that neglects the phase front curvature of the seed. We expect this to be a reasonable approximation since we are considering that the seed radiation source (tape) is many ($\gtrsim 10$) Rayleigh ranges from the undulator entrance and that the transverse electron beam size is much smaller than the spot size of the seed radiation in the undulator.

Consider seed radiation at the resonant wavelength for the beam in the undulator

$$k = 2k_u\gamma_r^2/\left(1+a_u^2\right), \tag{4.7}$$

where $kc = \omega = 2\pi c/\lambda$ is the radiation frequency, γ_r is the resonant beam energy, and we assume a planar undulator with $\lambda_u = 2\pi/k_u$ the undulator wavelength and $a_u = K/\sqrt{2}$ the normalized rms undulator field strength.

The seed radiation co-propagating with the electron beam in the undulator initiates bunching of the beam. To estimate this bunching we consider a 1D model of the interaction (note that the decrease in seed strength versus propagation is following 2D geometry). Assuming the normalized seed field is small $a_s \ll 1$, the combined fields of the undulator and seed provide a ponderomotive force on each electron such that

$$d\eta_j/dz = \kappa_B\left[(a+a_s)e^{i\theta_j} + \text{c.c}\right] \tag{4.8}$$

where $\eta_j = (\gamma_j - \gamma_r)/\gamma_r \ll 1$ is the energy deviation from resonance of the j^{th} electron, $a_s(z) = eA_s/m_ec^2$ is the normalized seed radiation field, $a = eA/m_ec^2$ is the normalized FEL radiation field, $\theta_j = (k+k_u)z_j - \omega t$ is the ponderomotive phase of the j^{th} electron, and $\kappa_B = kK[JJ]/(2\sqrt{2}\gamma_r^2)$. Here an average over the orbit in the planar undulator was performed and $[JJ] = J_0(\xi) - J_1(\xi)$ with $\xi = a_u^2/[2(1+a_u^2)]$ and J_m are the m^{th}-order Bessel functions. The position of the electron in the ponderomotive phase evolves as $d\theta_j/dz = 2k_u\eta_j$.

Assuming a slowly-varying envelope approximation and neglecting slippage effects, the linearized wave equation for the FEL radiation is

$$da/dz = \kappa_M\left\langle e^{-i\theta_j}\right\rangle, \tag{4.9}$$

where the brackets indicate an average over the beam electrons and $\kappa_M = k_p^2K[JJ]/(2\sqrt{2}k\gamma_r)$, with k_pc the plasma frequency corresponding to the beam density. The beam bunching $\langle\exp(-i\theta_j)\rangle$ drives the emission of FEL radiation. Using Eq. (4.8), neglecting harmonics, and linearizing, the evolution of the beam bunching is

$$\frac{d^2}{dz^2}\left\langle e^{-i\theta_j}\right\rangle = 2ik_u\kappa_B(a+a_s). \tag{4.10}$$

Combining Eqs. (4.9) and (4.10) yields the evolution of the FEL radiation driven by the seed,

$$\left(\partial_{\hat{z}}^3 - i\right) a = i a_s, \tag{4.11}$$

where $\hat{z} = 2\rho k_u z$, and the FEL parameter ρ is

$$\rho = \left(\frac{K^2 [JJ]^2 k_p^2}{32 k_u^2 \gamma_r^3} \right)^{1/3}, \tag{4.12}$$

with $L_g = 1/(2\sqrt{3}k_u\rho)$ the 1D FEL power gain length.

Equation (4.11) and the corresponding bunching $\langle \exp(-i\theta_j) \rangle = \kappa_M^{-1} da/dz$ can be solved for the a diffracting CWE seed of the form Eq. (4.6). The beam bunching $\langle \exp(-i\theta_j) \rangle$ is shown in Fig. 4.10 versus propagation distance in the undulator $k_u z$ for the FEL parameters $K = 1.25$, $\lambda_u = 2.18$ cm, $\gamma_r = 600$, and $\rho = 0.012$ ($I = 4.4$ kA and 24 μm transverse rms beam size), and the CWE seed parameters $a_{s0} = 2 \times 10^{-4}$, $z_f = -1$ cm, and $Z_{Rs} = 524$ μm [27].

4.7 Conclusion

In this chapter, experimental results for coherent wake emission (CWE) driven surface high-harmonic generation (SHHG) from a thin-tape were presented. Such an experimental configuration allows for the SHHG source to be placed near the undulator entrance in an LPA-based FEL experiment, where the SHHG pulse will act as a seed to enhance FEL lasing. CWE pulse properties from various tape materials (VHS, Mylar, and Kapton) were compared to a polished glass substrate. The roughness of the materials, defined as a power spectral density function versus spatial frequency, was extensively studied. In terms of CWE pulse characterization, we recorded the spectrum, spatial profile, divergence, and absolute flux. The glass was the smoothest structure over the relevant spatial scale-lengths, yielding the lowest divergence [4 mrad (rms)], but at a low 15^{th}-order conversion efficiency (CE) of 2.9×10^{-8}. Its CWE spectrum covered the harmonic orders up to the 21^{st}. Among the tapes Kapton was the smoothest, resulting in the smallest divergences of the harmonic signal produced from a tape (rms divergence = 8 mrad). At 4.8×10^{-7}, the 15^{th}-order CE was significantly larger than for glass. The VHS and Mylar tapes were the roughest targets, and yielded the largest divergences at 12 mrad (rms) and 14 mrad (rms), respectively. The VHS tape however did produce the largest 15^{th}-order CE at 6.5×10^{-7}. All tapes produced harmonics up to the 17^{th}. An overview of the measured CWE parameters is given in Table 4.1.

It was demonstrated that the CWE regime offers great shot-to-shot stability due to the intrinsic nature of the (quasi)-linear physics driving the emission process. The pointing fluctuation was of the 0.2 mrad level (few % of the total divergence). The shot-to-shot variations in beam divergence and total counts was also of few % level (without correcting for laser energy fluctuations).

Based on these measurements, 3 MW CWE pulses can be delivered into the undulator. This is based on 60 nJ in the 15^{th} order in a 20 fs pulse, with 100 mJ of laser energy and a CE of 5-7$\times 10^{-7}$. We presented a model that calculated the effect of the seed on the electron beam micro-bunching following undulator propagation. Parameters close to the proposed LPA-based experiment [65] (largely based on existing hardware parameters of the BELLA Center) were used. It was shown that within 10 undulator periods, the seed already initiated strong bunching approaching normalized bunch parameters of $|B| = 10^{-2}$. In this model, the focal location of the $a_0 = 2 \times 10^{-4}$ seed was placed 1 cm upstream of the undulator entrance. For the current measured seed parameters and model results, the outlook for an LPA-based seeded FEL seems promising.

Chapter 5

Tape Based Plasma Mirror Characterization

5.1 Introduction

When a highly-intense laser pulse interacts with a solid surface, ionization of the solid occurs creating a surface plasma. Following ionization, the plasma expands into vacuum creating a plasma density gradient seen by the remaining portion of the input pulse. The remainder of the pulse interacts with the expanding plasma, which reflects the light at the critical surface, n_{crit}, creating a plasma mirror (PM) reflection. One challenge to using the PM experimentally is that the formation of a surface plasma is destructive to the solid surface in the area of the laser focus. After each shot, an undamaged surface must be provided [63]. This chapter explores the use of a thin, spooled tape surface a plasma mirror, which allows for 10's of thousands of shots on target before the tape must be replaced [25, 26].

With a high quality reflection and minimal pointing fluctuations, a plasma mirror can be used as a reproducible steering optic in a geometry where a laser pulse is near focus and damage to the optic will occur. PMs are more conventionally used to provide contrast enhancement.

Using a thin tape as a plasma mirror has other advantages over more conventional, polished-glass, plasma mirrors [63]. One example is using a thin tape to transmit an electron beam through the tape while reflecting the input laser light. This creates new experimental geometries that require the spatial overlap of a particle beam and reflected light [25, 26].

A tape drive has been developed and optimized at the BELLA Center at the Lawrence Berkeley National Laboratory, which spools 1/2 inch wide VHS tapes of 15 μm of thickness [88]. With pointing fluctuations on the order of the laser itself and reflectance of $> 80\%$ the input light make this a novel, replaceable, steering mirror which can be positioned near the focal plane of a laser.

5.2 Thin, spooling, tape-based plasma mirror

5.2.1 Tape drive motion and tape design

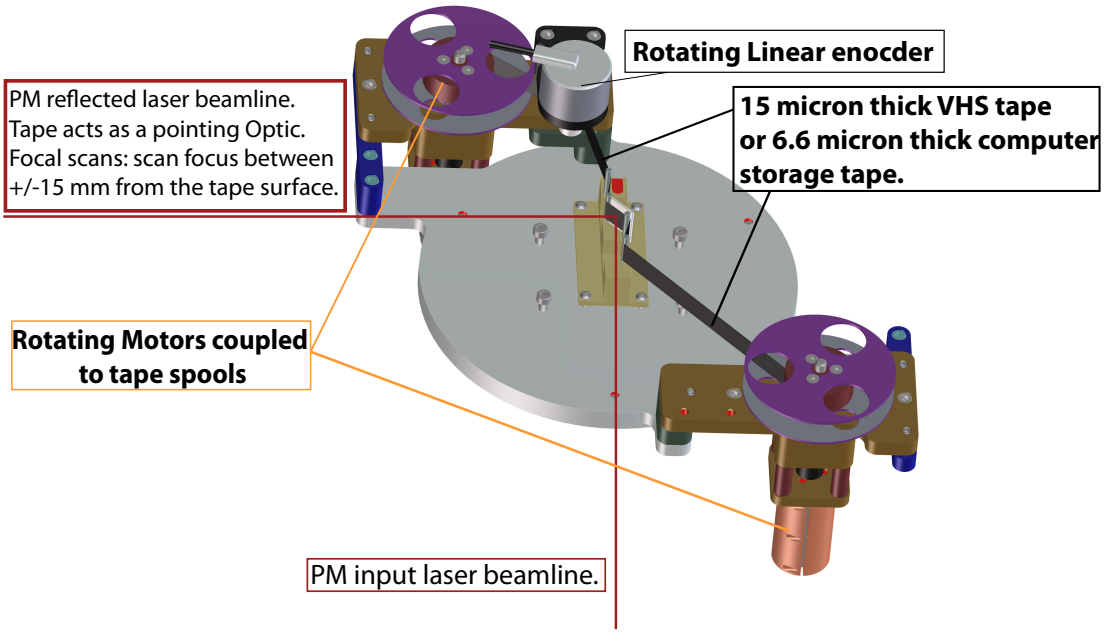

Figure 5.1: A schematic of the tape drive is shown here. The tape drive consists of two motors coupled to rotating reels for spooling the tape, a rotating linear encoder, and metal pegs to maneuver the tape into place.

The electronics of the tape drive are shown in Fig. 5.1. The tape drive consist of two Faulhaber DC stepper motors and a linear encoder used to track the movement of the tape. Each stepper motor is surrounded by water cooled insulation to allow for use in vacuum without heating up, and the motors are controlled using a Newport ESP301 3-Axis Motion Controller. When the tape is being held stationary each of the two motors pull the tape with equal force in opposite directions, creating tension and keeping the tape from moving. Providing the proper tension on the tape is crucial to ensure the tape surface doesn't ripple, bow, or break from the holes created following each laser shot. To spool the tape, the rotational force in one of the two tape motors is gradually reduced until the tape begins to move. This tape surface motion is spooled in a controlled way, which is monitored by the encoder. Once the tape has spooled by the correct amount, the rotational force in both motors is again equalized, and the tape is held taut.

5.2.2 Chemical structure and material make up of magnetic recording tapes

The make-up of the magnetic recording tapes used in this study are all constructed with a plastic base, which acts as the bulk material support for magnetic particles on the surface [88]. The magnetic particles are bound to the plastic using a binding polymer, which has a mass ratio of $\sim 50/50$ (mass binding polymer/mass magnetic particles) and a volume ratio of $\sim 90/10$ (volume binding polymer/volume magnetic particles). Since the density of the magnetic surface polymers differs little for different tapes, manufacturers typically alter the thickness of the plastic substrate in order to allow for more or less tape to be spooled onto a single spool, giving consumers more or less data storage capabilities on a standardized size spool of tape [88]. The tapes used in this study had a thickness of 6.6 μm for computer storage tape [89] (5.1 μm thick plastic film with 1.5 μm thick recording layer with a possible backing coating [90] depending on the manufacturer) and a thickness of 15 μm for standard VHS tapes [88] (13.5 μm thick plastic film with 1.5 μm thick recording layer).

The computer storage tape used in this study is an Linear Tape-Open (LTO) Ultrium 4 800 GB Data Cartridge [89]. In the characterization of the tape to be used for this study (Shown in Fig. 4.3), LTO storage tapes were chosen due to their thickness of 6-8 μm [91, 89, 92]. Because the PM is being used in the two staged acceleration experiment, which requires the transmission of an electron beam through the bulk of the tape, the thickness of the material was minimized to decrease negative affects to the electron beam's emittance. The LTO 4 800 GB cartridge was chosen because it is thinner than the LTO 1, 2, and 3 models, and provided a better pointing stability than the LTO 5 1.5 TB tapes, which have a thickness of 6.4 μm [92].

It has been shown in Chap. 4 of this thesis (see also Ref. [25]), that surface high harmonic-generation (SHHG) produced from the recording side of a magnetic storage tape produces harmonics up to $\lambda = 40$ nm (20^{th} order of the 800 nm drive laser). The harmonic cutoff order for the sub-relativistic ($a_o = 0.29$ in Ref. [25]) SHHG scales with the maximum electron density of the solid material. Plastics are only capable of producing light up to $\lambda \sim 50$ nm (due to their maximum electron density of $\sim 4 \times 10^{23}$ cm^{-3}). Therefore, the presence of sub-relativistic harmonics up to $\lambda = 40$ nm produced from the front surface of VHS tape, indicates the interaction of the laser pulse with magnetic particles (Iron(III) oxide and binder mixture).

5.3 Plasma mirror (PM) reflectance measurement

The reflectance of a PM is affected by two factors: how much energy gets absorbed by the plasma, and the flatness of the ionized surface plasma when the peak of the pulse interacts with the PM. In the left region of Fig. 5.2 (Region I), the focus of the pulse is close to the tape surface (tape surface at x = 0 mm). Here the spot size of the laser is small, creating a high fluence on the surface of the tape. With a higher fluence, the surfaced is ionized

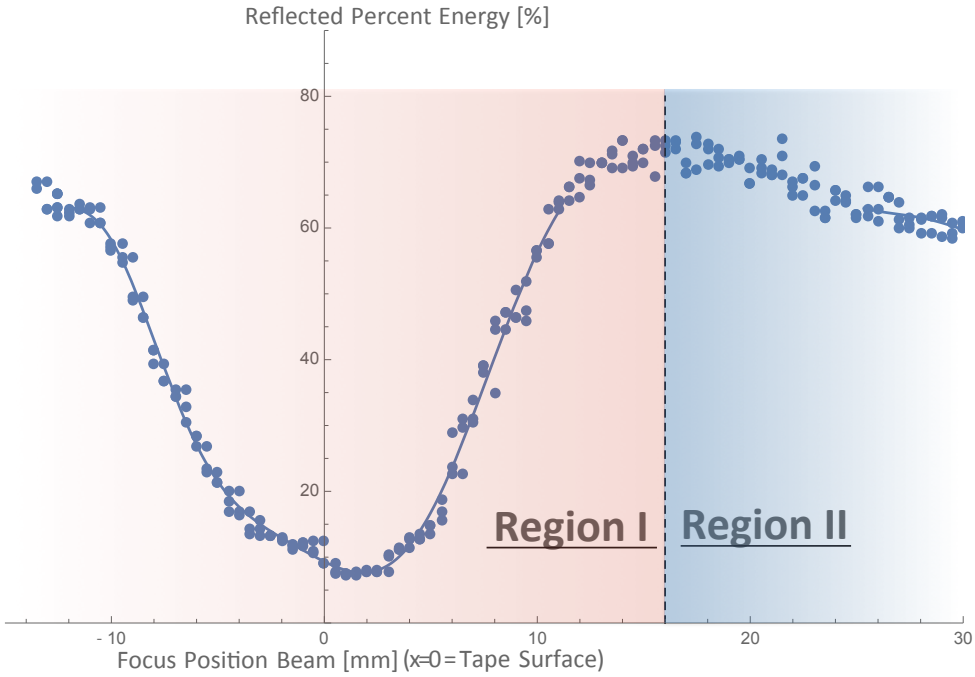

Figure 5.2: A plot showing the reflectance from a PM for different focal locations, x. The tape surface is at x = 0 mm. Two regions are shown which do not provide the ideal pulse reflection due to the triggering time of the plasma mirror. The left region (Region I), shows when the focus of the laser is positioned on or very close to the position of the tape. The right region (Region II), shows when the focus of the laser is positioned far downstream of the tape surface.

earlier in the pulse's shoulder, and the plasma begins expanding. The losses in this region are due to the long plasma gradient lengths. By the time the peak arrives the plasma surface has already expanded enough to shape the plasma into a convex surface, creating a poor reflection.

The right region of Fig. 5.2 (Region II), shows when the focus of the laser is positioned downstream of the tape surface. In this region, the spot size of the laser is large. The low intensity on the tape will not ionize in the pulse's shoulder but rather in the peak of the pulse. Here the pulse sees a flat surface and a high percentage reflection is produced.

The flatness of the ionized surface is the basis of the plasma mirror model discussed in Section. 5.6. The wavefront of the reflected light is distorted due to the shape of the PM surface. This will produce a phase shift of $\delta\psi$ caused by nonuniform critical surface expansion. The maximum phase shift introduced on a surface with a height perturbation of δx with input angle of θ_i, is given by

$$\delta\psi = \frac{2\pi}{\lambda} 2\delta x \cos\theta_i. \tag{5.1}$$

An equation very similar to the Nevot-Croce method [84] used in Section 4.3.1 was used to model the reflectance of the plasma mirror data collected from both sides of the VHS and

computer data tape, as well as a study of reflectances from S-polarized and P-polarized light from both sides of the VHS tape. The equation used to model the reflectance from the PM is a statistical treatment of electromagnetic waves incident on a normally distributed surface given in Refs. [93, 20]:

$$I_{coh} = I_0 \ \exp\left[-\left(\frac{4\pi\sigma_x}{\lambda}\cos\theta_i\right)^2\right]. \tag{5.2}$$

This is the cornerstone of the reflectance model in Sec. 5.6 used to understand and fit the experimental data.

5.3.1 Reflectance of s-polarized light

The reflectivity of the plasma mirror will change, as the polarization of light changes. First, we observe the reflectivity of the plasma mirror when the drive laser is s-polarized. An s-polarized light wave (E perpendicular to the plane normal to the optical surface) is purely transverse, and no coupling occurs between the input light's E-field and the expanding plasma electrons ($\nabla \cdot E = 0$).

5.3.2 Reflectance of p-polarized light

Light of p-polarization has electric field components which are in the same plane as the expanding plasma gradient. The E_z component along the plasma density gradient can drive a electrostatic charge density oscillation at $\omega = \omega_p$. This transfer of energy, known as resonance absorption [75], is a coupling between the laser and plasma electrons. Another interaction, Brunel absorption [23], pulls the electrons from the expanding plasma surface along the electric field lines in the plane normal to the optical surface. Once the electric field lines flip, the electron are accelerated back towards the expanding plasma, traveling through the plasma and creating wakes in the path. These Brunel electrons undergo linear mode conversion [16], and result in harmonic-generation of the drive laser (As discussed in section 4.2.1).

5.3.2.1 Resonance absorption

Resonance absorption [75] occurs when a p-polarized laser pulse interacts with a plasma density gradient at angle $\theta \neq 0$. Since the laser pulse interacts with the plasma at an angle, there is a non-zero portion of the electric field which is perpendicular to the target surface. Typically, laser-plasma interaction restricts light from traveling through a plasma with a density higher than the critical density n_{crit}, because at this point the index of refraction $n = \sqrt{1 - \frac{n_{plasma}}{n_{crit}}}$ becomes imaginary, and a small portion of the light is absorbed.

In the case of light interacting with a plasma gradient at an incidence angle θ, the light is reflected before reaching the critical surface at a density of $n = n_{crit}\cos^2\theta$, as shown in Fig. 5.3. If the scale length L of the plasma is small enough, a portion of light is able to tunnel

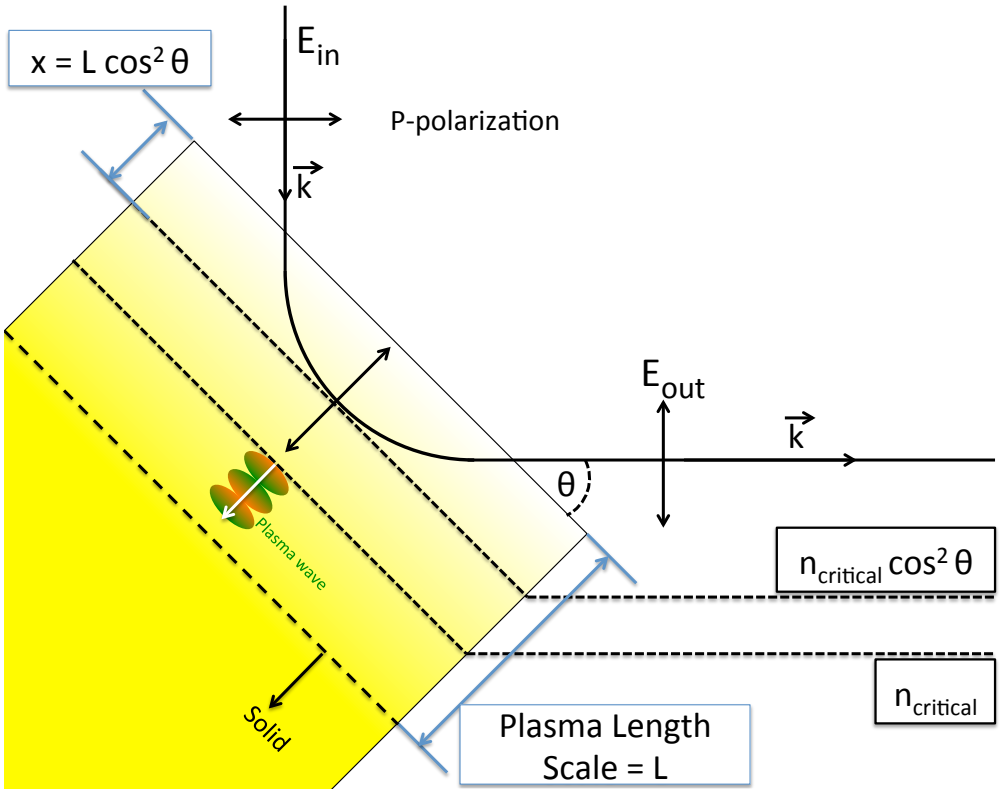

Figure 5.3: A schematic showing the reflection of an incoming linearly polarized laser pulse onto a plasma gradient. The pulse is reflected before reaching the critical surface where the density is $n_e = n_{crit} \cos^2 \theta$. Due to a short plasma length scale L, the p-polarized electric field is able to tunnel beyond the critical surface, and drive a resonant plasma wave into the plasma.

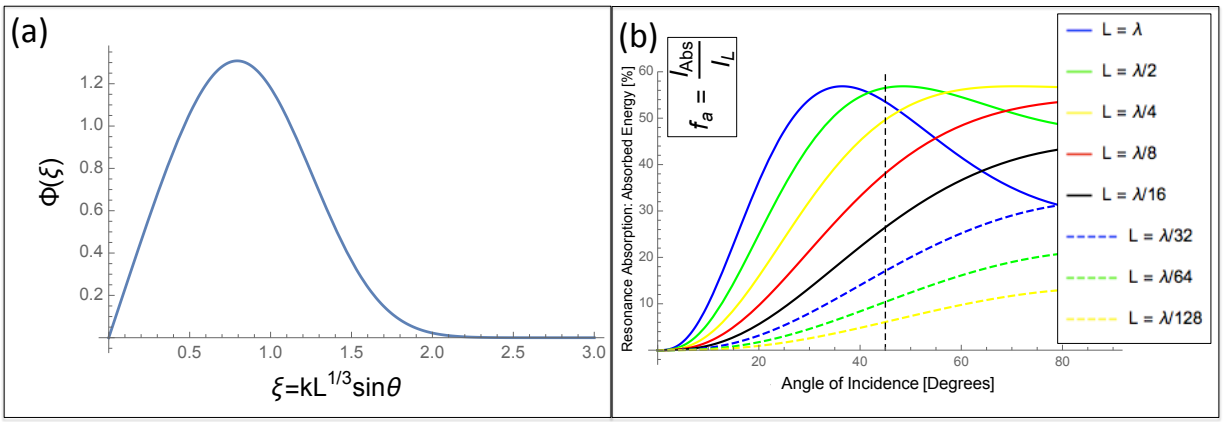

Figure 5.4: Fig. (a) Shows the angular absorption function for resonance absorption for p-polarized light, as given by Eq. 5.3. Fig. (b) Shows the percent of absorbed energy for resonance absorption different plasma scale lengths, as a function of input angle.

through the critical surface, the conversion point where $n = n_{crit}$, and drive a Langmuir oscillation of the plasma. The plasma wave is driven at the frequency $\omega = \omega_p = \omega_{Laser}$, and this energy absorption technique is called resonance absorption [75].

In Fig. 5.3, the expanding density profile, $n_e = n_{crit}x/L$, of the plasma is determined by the scale length L. The scale length depends on the expansion velocity of the plasma electrons, and when the incident surface becomes ionized. In order to ensure that the plasma is not formed too early (expand too much before the peak of the laser pulse arrives) the temporal contrast of the laser pulse is an important factor in the amount of light which experiences resonance absorption. A higher contrast causes a smaller scale length, and small scale lengths allows the light to tunnel through the critical surface where the plasma wave can be driven resonantly. The behavior of the absorption for a given angle is given by $\Phi(\xi)$ where $\xi = (kL)^{1/3}\sin\theta$ [16, 94]:

$$\Phi(\xi) \simeq 2.3\xi e^{\frac{-2\xi^3}{3}}. \tag{5.3}$$

This function is plotted in Fig. 5.4(a).

The amount of absorbed laser energy is estimated as [15]:

$$f_a = \frac{I_{absorbed}}{I_{Laser}} \simeq 36\xi^2 \frac{Ai(\xi)^3}{\frac{dAi(\xi)}{d\xi}}, \tag{5.4}$$

with Ai(x) being the Airy function of x. For our case, the PM is a statistical treatment of electromagnetic waves incident on a normally distributed surface of roughness σ_x, which is discussed and explained in sections 5.3 and 5.6. The percent of absorbed energy from resonance absorption can therefore be calculated for a plasma gradient with a gradient length of σ_x.

5.3.2.2 Brunel absorption

Brunel absorption [23] occurs when p-polarized light interacts with a sharp plasma density gradient. If the oscillating electrons of the density gradient with the amplitude $x_p \sim eE_L/m_e\omega_L^2 = v_{os}/\omega_L$ exceed the density scale length $v_{os}/\omega_L > L$ the resonance is broken [15]. However, electrons close to the edge of a sharp density profile can be accelerated into the vacuum during half of the laser's electric field cycle. When the field reverses, these electrons are re-accelerated into the plasma because the laser field can not penetrate beyond the point of critical density. Thus, electrons are accelerated out of the target, gaining kinetic energy before returning and traveling into the target. The angular dependence of the absorption rate is given in Ref. [15] as:

$$\eta_{Brunel} = \frac{1}{\pi a_0} f[\left(1 + f^2 a_0^2 \sin^2\theta\right)^{1/2} - 1]\frac{\sin\theta}{\cos\theta} \tag{5.5}$$

where θ is the incident angle, $\alpha(\theta) = \sin^3\theta/\cos\theta, f = \left(\sqrt{1+8\beta}-1\right)/(2\beta)$ and $\beta = a_0\alpha(\theta)/2\pi$. The function is plotted in Fig. 5.5.

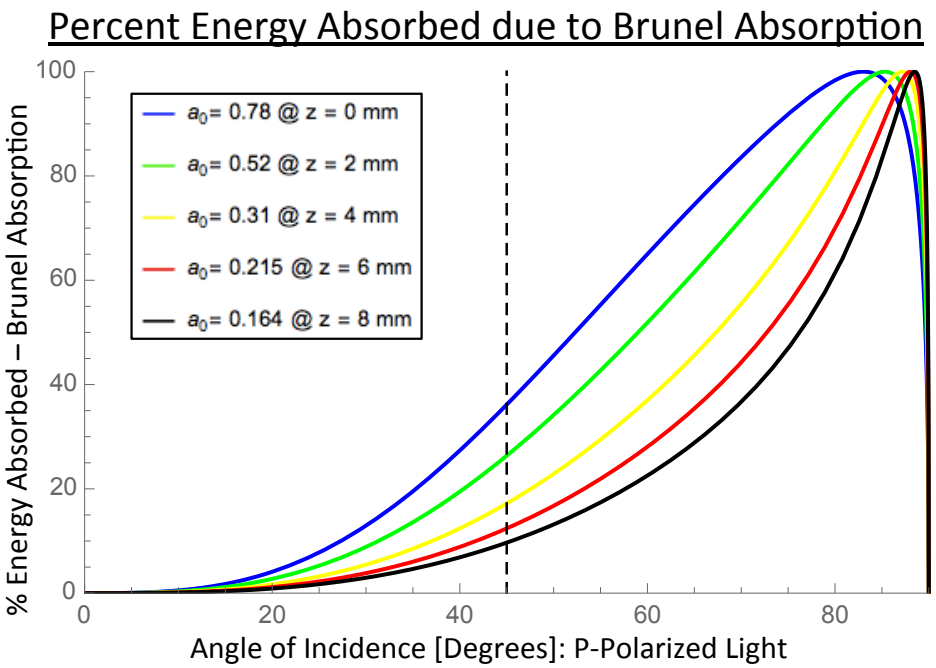

Figure 5.5: Shows the angular dependance of absorption, as given by Eq. 5.5.

Equation 5.5 has a dependence on the intensity of the input laser pulse as well as the angle of incidence. In the plasma mirror characterization, the intensity of light on the tape was scanned by shifting the focal position of the pulse in front of, onto and beyond the tape surface. The intensity changes as the inverse of the spot size $(1/\pi w(z)^2)$. The effect this will have on the percent of absorbed energy due to Brunel absorption at each of the integer $z_{Rayleigh}$ lengths is shown in Fig. 5.5. When the focus is shifted onto the tape, the value of $a_0 = 0.78$, and by moving focus away from the tape the value of a_0 changes to $a_0 = 0.52$ a z = 2 mm (1 Rayleigh range from focus), $a_0 = 0.31$ a z= 4 mm (2 Rayleigh ranges from focus) and $a_0 = 0.215$ at z = 6 mm (3 Rayleigh ranges from focus).

5.3.3 Plasma gradient length effects on absorption in p-polarization

The gradient length of the plasma is the length over which the plasma has expanded. At a given time, the density gradient has decreases exponentially as $n[x] = n_{Max}e^{-x/L}$. We define the plasma gradient length as the length, L, where the density has decrease by on e-folding.

The temperature of the plasma determines the expansion velocity of the electrons after ionization occurs. If the plasma has enough time to expand such that the surface is no longer flat, the reflected energy will decrease. This is seen in region I on the left of Fig. 5.2. In this region, the spot size on the tape is small, resulting in higher intensities, and ionization

occurs up to 1.7 ps before the peak of the pulse arrives. If the expansion of the surface were uniform, the reflectance wouldn't decrease, because the beam would see an expanding flat mirror surface. However, a convex curved surface is created because the intensity and temperature in the center of the pulse is highest, and the intensity drops as a function of e^{-r^2} (assuming the laser spot is a Gaussian on the surface of the tape). This curvature of the PM has been studied and characterized in Reference [20].

5.4 Experimental setup

The plasma mirror characterization experiments were performed on the staging beamline shown in Fig. 5.6. A laser pulse of 2.0 J with a duration of 40 fs is split using a beamsplitter. 70% of the beam is reflected onto beamline 1 (35 TW at 40 fs) and and 30% is transmitted onto beamline 2 (15 TW at 40 fs). Both laser pulses are focused using off-axis parabolic mirrors (OAPs) with f-number f/25, and get focused down to a spot size of $w_0 = 22$ μm. The PM target is positioned at the two beams' crossing point .

The laser pulses following the reflection of the PM (on beamline two of Fig. 5.6) are attenuated and diagnosed using wedged reflective optics in the reflective telescope. The first wedge reflects 1% of the energy into the reflective telescope for diagnosis and the other 99% is transmitted to a laser beam dump. The telescope consisted of a concave mirror (③ in Fig. 5.6), and a convex mirror (④ in Fig. 5.6). The reflective optics are used to focus the laser pulses without significant aberrations. The optical image of the laser at the target was recorded using a 10-bit CCD camera, referred to as a mode imager.

One diagnostic which is not shown in the staging layout in Fig. 5.6 is a diagnostic used to ensure the tape is spooled correctly. The "Tape Monitor" is used as a interlock with the high power laser to ensure the tape spooled correctly before a high powered laser pulse is fired.

5.4.1 Tape monitor diagnostic

The flatness of the tape at focus will affect the direction and angle of the reflected beam off the tape surface. If the tape is held with too much tension in the motors, the tape surface tends to bow or ripple, causing the reflected beam to stray from the desired beampath. If the motors do not provide enough tension, the tape will sag, which will also lead to misalignment in the reflected beam. A proper tension is required for a given tape, and different tapes will require different motor tensions depending on the rigidity of the tape. The rigidity of the tape is determined by the tapes bulk material, as well as the thickness of the tape [88]. Therefore an interlocking feature is employed to ensure the tape at the position of the high power beamline is flat and correctly spooled.

In order to ensure a proper spooling of the tape, the flatness of the tape surface is monitored by a low energy, HeNe beam, reflected off of the tape surface, and imaged to monitor the position of the reflected beam. A cross-hair is used in the HeNe beam as a mask

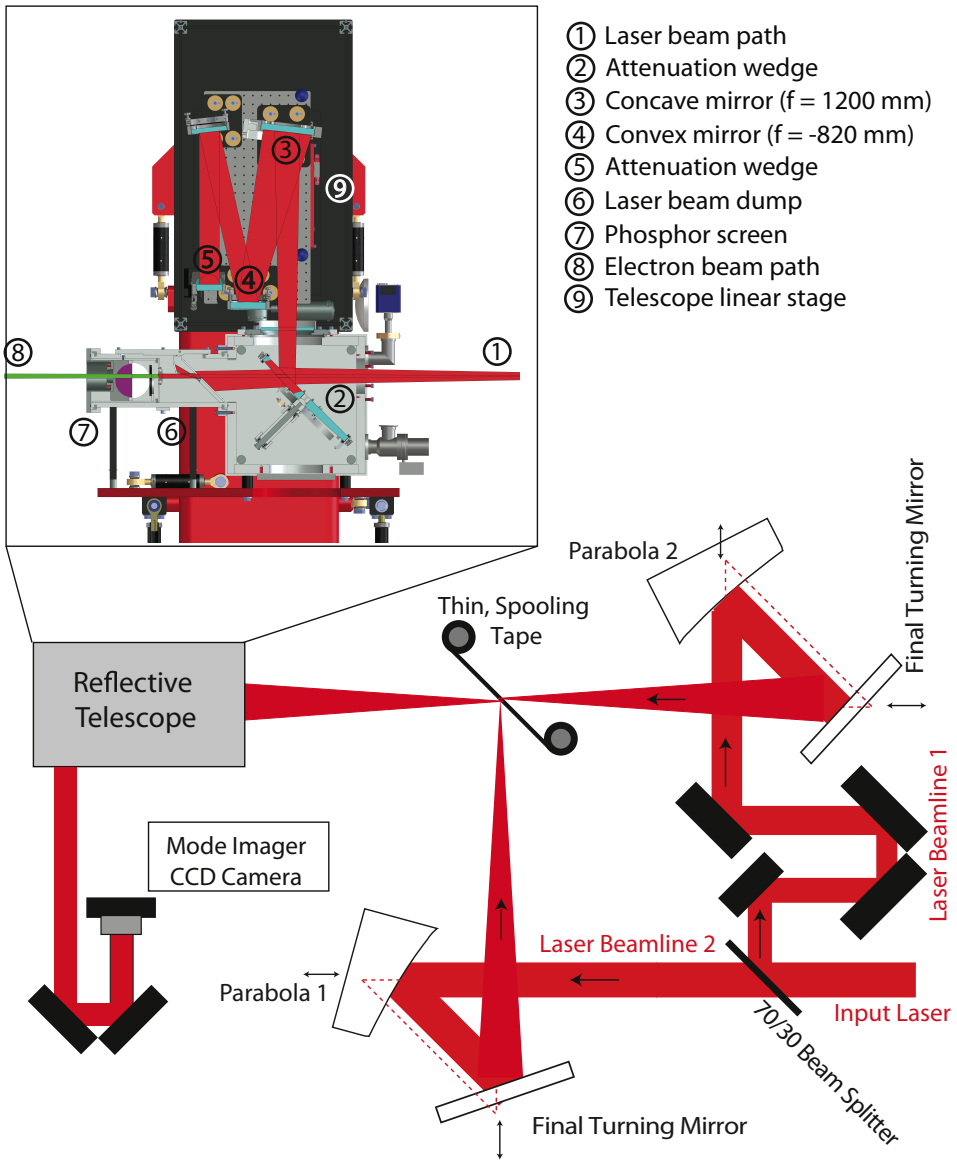

Figure 5.6: A schematic of the staging beamline. The input laser is split using a 70% reflective and 30% transmissive beamsplitter. Laser beamline 1 is used on the staged acceleration experiment to create an electron beam from a gas jet placed at focus of laser beamline 1. The gas jet is placed a centimeter upstream of tape surface, and following the creation of the electron beam, the tape is used as a PM to remove laser beam 1 from the beam line. Laser beamline 2 focuses downstream of the tape drive following a PM reflection from the tape. By tuning the delay stage in beamline 1, the electron beam from beamline 1 and the laser pulse from beamline 2 become overlapped in time and space. The reflective telescope is used to change the location of the imaging plane for the mode imager CCD camera. The schematic of the reflective telescope is from Ref. [18].

to determine how well the reflected mode looks after reflection from the tape (As seen in Fig. 5.7). The tape monitor is used with the tape drive and driver software to provide a

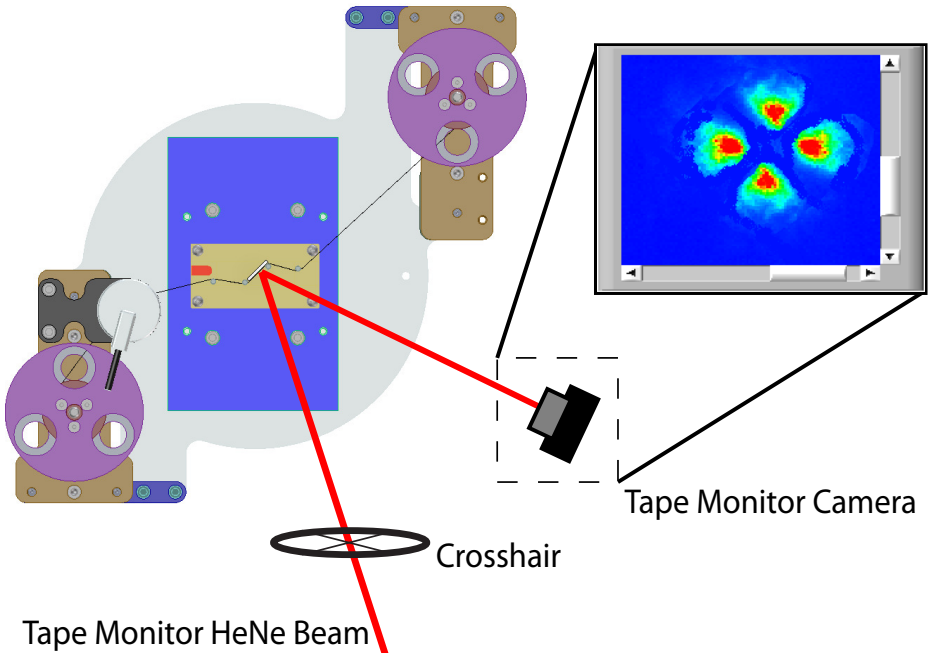

Figure 5.7: A schematic of the tape monitor consisting of a HeNe laser, cross-hair, reflective tape surface, and camera are shown. A cross-hair is used as a mask to determine the quality of the reflected mode. If the image seen on the tape monitor camera has four equally space beamlets, the tape is flat and a shot is allowed.

quantitative way of determining weather the tape moved successfully and smoothly. This ensures that their is a flat surface along the beamline, minimizing fluctuations in pointing. If a poor reflected mode is detected, the tape surface is spooled again, and the laser system inhibits a shot from being taken.

5.4.2 Pointing fluctuation measurement setup

To measure the shot-to-shot fluctuation caused by the PM, two pointing fluctuation measurements were taken and compared. A pointing fluctuation measurement of a low power, HeNe laser was measured from the reflection from the non-ionized tape surface. By not creating a surface plasma, measuring the HeNe reflection allowed for the pointing fluctuation caused by the fluctuations in the flatness of the tape. This measurement was taken for different spooling tensions. The pointing fluctuation setup of the HeNe laser is given in Fig. 5.8. The setup is made up of an input HeNe, the tape drive spooled with VHS tape and a CCD camera to record the pointing fluctuations. The tape is spooled between each acquisition of the CCD camera. Also, a tape monitor (described in section 5.4.1) was used for this measurement to ensure the tape spooled properly, as it would on a high power PM study.

The measurement of the ionizing high-power PM pointing jitter is a convolution of the

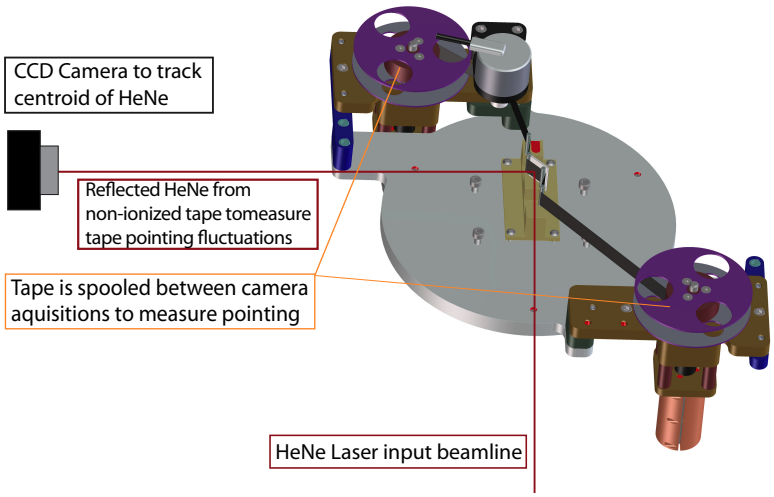

Figure 5.8: The experimental setup used to measure the tape surface pointing stability of a non-ionizing, HeNe laser beam. The HeNe beam is not intense enough to ionized the tape, so the measured pointing fluctuations are a property of the tape material only. If the reflected laser beam's pointing fluctuates it is due to the tape not being flat. This could be due to ripples or slack in the tape which could create a non-flat surface.

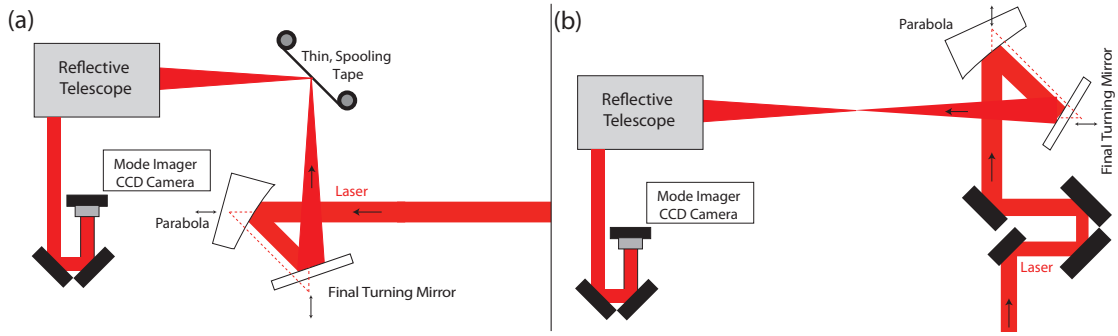

Figure 5.9: (a) A schematic of the setup used to measure the pointing fluctuations seen in beamline two following the PM reflection. This measurement is a convolution of the pointing fluctuations of the PM and the intrinsic laser jitter of the TREX laser pulses. (b) A schematic of the setup used to measure the laser jitter of the TREX laser system as the focus of beamline one. The pointing fluctuations are measured by the mode imager, and the contents of the reflective telescope are given in Fig. 5.6.

pointing fluctuations caused by the dynamics of the PM and the intrinsic laser jitter of the TREX laser pulses. By measuring the two effects separately, the pointing fluctuation of the PM (without including the laser jitter) can be determined. The pointing fluctuation measurement from the PM was performed using only beamline two (shown in Fig. 5.9 (a)). These pointing fluctuations are compared to the pointing jitter from the TREX laser at focus of beamline one (shown in Fig. 5.9 (b)). Beamline one and two are produced from the same input beam, and the focusing geometry of the two beamlines is the same. Therefore, it's assumed that the laser jitter in beamline one is equivalent to the fluctuations expected in

beamline two. Both the pointing fluctuations of the PM and the laser jitter were measured on the mode imager, which was imaging the focal plane of the pulses.

5.4.3 Reflectance measurement setup

The plasma mirror reflectance measurements are also performed using only beamline two. The laser pulses reflected from the tape-based PM are sent into the reflective telescope, and a large area energy meter is placed behind an optically flat wedge (⑤ in Fig. 5.6) for diagnosis. This energy meter is cross-calibrated with an energy meter upstream, which measures the pulse's energy at the compressor. This cross-calibration allows for the reflectance to be calculated for each PM shot.

The input intensity is scanned for the reflectance measurements by scanning the focus of parabola two along the axis of propagation. By translating the parabola and the final turning mirror together, the focus can be shifted upstream and downstream of the tape while maintaining the transverse position of the spot on the tape surface.

5.5 Experimental results

5.5.1 Pointing fluctuations of non-ionized thin tape

The restrictions for the pointing fluctuations of the tape based plasma mirror into a 250 μm diameter capillary are are set by the staged acceleration campaign. The capillary is placed 10 mm downstream of the tape drive, and the laser spot size is $w_0 = 22$ μm. In order to keep the laser pulse such that the input beam does not miss the guiding axis of the channel, the pointing fluctuation of the reflected beams must be < 2.2 mrad. The pointing fluctuation of the tape surface was measured using the standard deviation of the centroid of a reflected HeNe was measure to be 310 μrad.

5.5.2 Pointing fluctuations from ionized plasma mirror

The pointing fluctuations of the reflected laser pulse from the plasma mirror were measured and compared to the input laser jitter without the presence of a plasma mirror. The results of this comparison are given in Fig. 5.10. The input laser jitter is measured by taking the standard deviation of the centroid in x and y of the laser pulses at focus on the mode imager camera (PM removed). The input laser's pointing fluctuations was measure at focus with $\Delta x_{Laser} = 4.1\mu$ and $\Delta y_{Laser} = 10$ μm. These fluctuation values are coupled into the value of the pointing fluctuation measured from the reflected plasma mirror pulses. The reflected pulses off the PM were measured when focusing 10 mm downstream of the tape surface. The PM pointing fluctuations were measured as $\Delta x_{PM+Laser} = 10.3$ μm in x and $\Delta y_{PM+Laser} = 14.2$ μm in y. So we calculate the pointing fluctuations due only to the plasma mirror as $\Delta x^2_{PM} = \Delta x^2_{PM+Laser} - \Delta x^2_{Laser}$. The results for in Δx_{PM} and Δy_{PM} are $\Delta x_{PM} =$

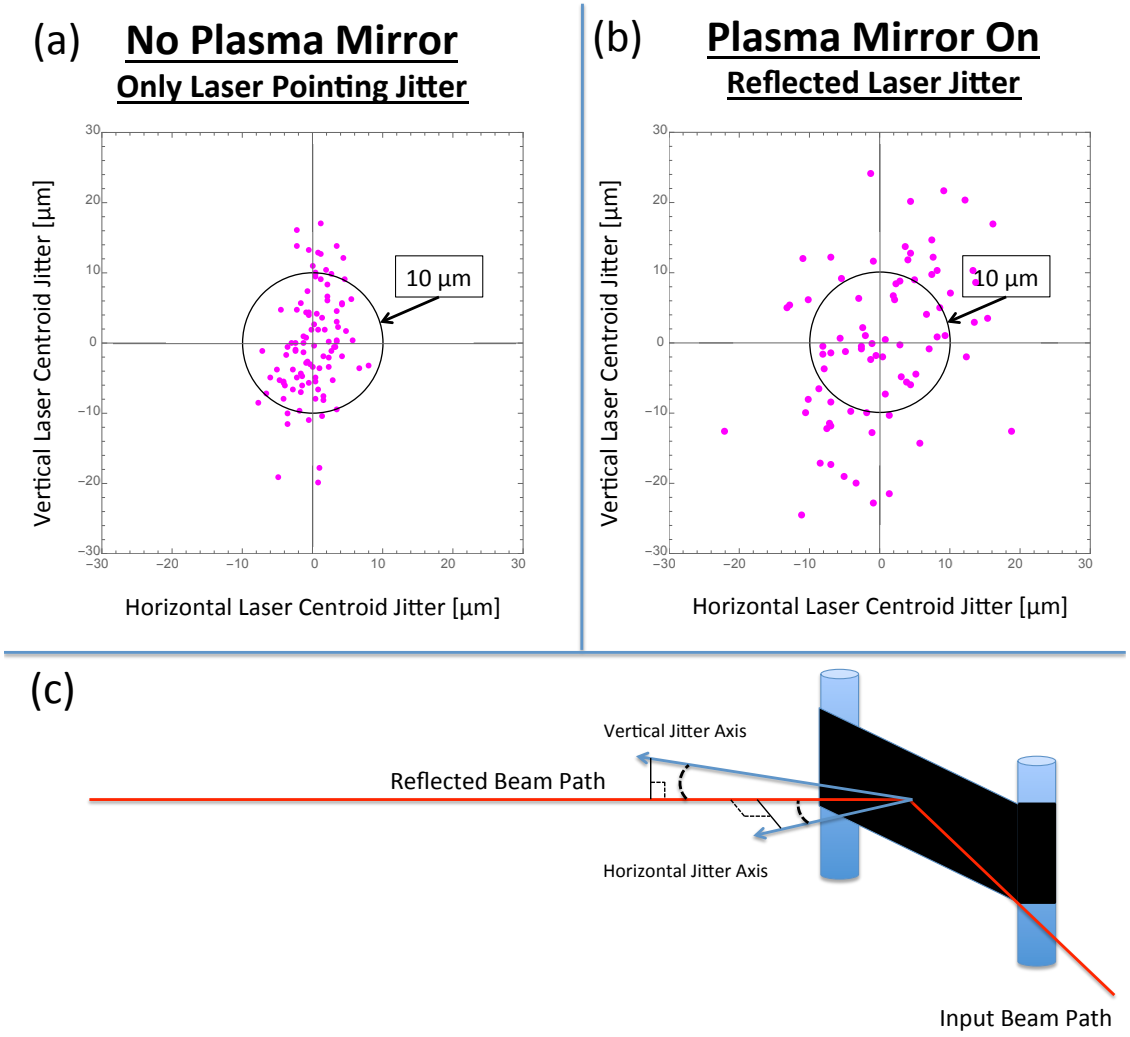

Figure 5.10: Results of high-power laser pointing study. (a) Input Laser jitter $\Delta x_{Laser} = 4.1\mu$m and $\Delta y_{Laser} = 10$ μm. (b) Jitter of laser reflected from tape-based plasma mirror $\Delta x_{PM+Laser} = 10.3$ μm and $\Delta y_{PM+Laser} = 14.2$ μm. (c) Schematic of input laser and tape drive showing the axes of the reflected jitter.

9.4 μm and $\Delta y_{PM} = 10.1$ μm. These values are converted to angular fluctuation from the tape surface 10 mm upstream. The angular fluctuations of the PM are $\theta_{PM+LaserJitter} = 940$ μrad in x and $\theta_{PM+LaserJitter} = 1.0$ mrad in y. These values are roughly 3 times higher than the HeNe reflections from the non-ionized tape surface. The increases in pointing fluctuation from the 310 μrad from HeNe to 940 μrad and 1.0 mrad is due to the dynamics of the expanding plasma.

By placing the focus of the reflected PM pulse 10 mm downstream of the tape, a pointing fluctuation of $\theta_{PM+LaserJitter} = 940$ μrad in x and $\theta_{PM+LaserJitter} = 1$mrad produces an aver-

age pointing error of 13.7 μm at the focal plane. With a second stage 10 mm downstream of the PM, the reflected beam will enter the cap on-axis. This makes this tape drive an instrument with precision high enough to serve as the coupling optic for the staged acceleration experiment.

5.5.3 Reflectance study: s and p-polarization

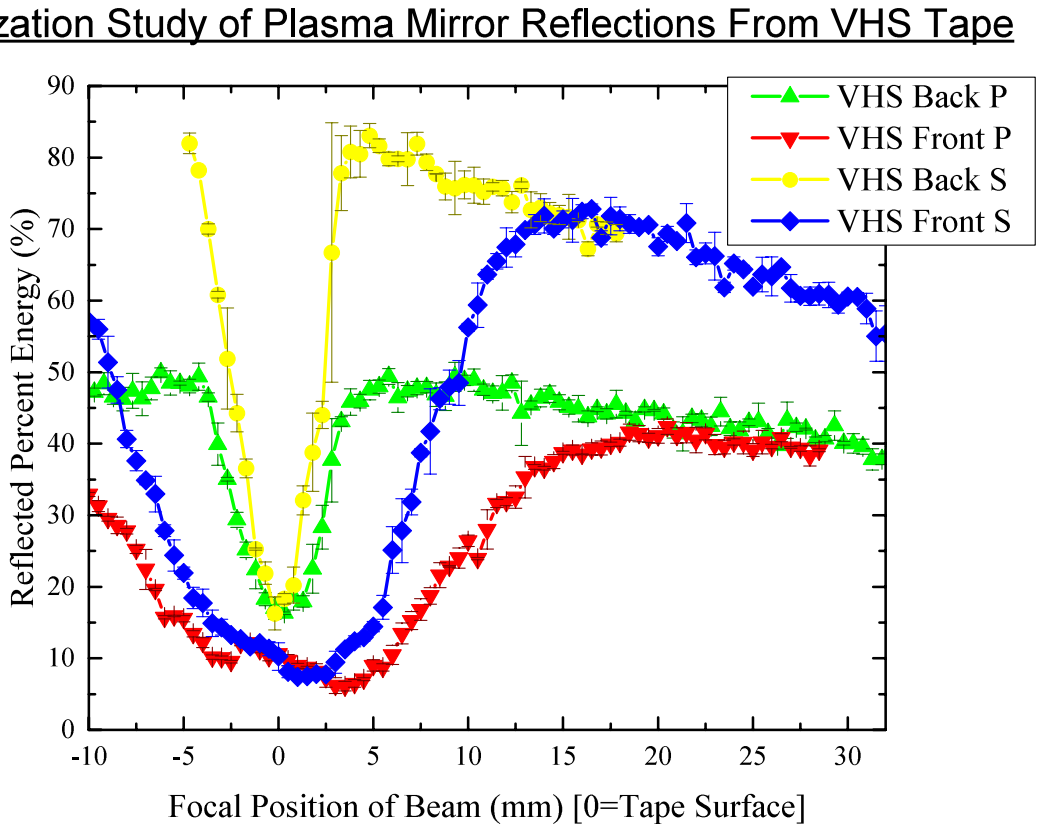

Figure 5.11: Plot showing the reflected energy from each sides of a VHS tape plasma mirror using s and p-polarized light. The side labeled "front" refers to the side of the tape which contains the magnetic Iron(III) oxide particles and the bonding material. The side labeled "back" refers to the mylar structure of the VHS tape which is 13.5 μm thick and is used to support the recording layer during playback of VHS tapes.

The experimental study of the reflectance of s-polarized light and p-polarized light was studied using the the front and back surface of a VHS tape as the plasma mirror. The results of the study are given in Fig. 5.11.

The percent of the input laser pulses energy absorbed from Brunel and resonance ab-

sorption in the cases of p-polarized light is found using

$$A_{B+R}[z] = 1 - \frac{R_{P-pol}[z]}{R_{S-pol}[z]}. \tag{5.6}$$

Here A_{B+R} is the percent of input light which is absorbed and R[z] is the reflectance at a given z location. The function A[z] has a z dependence because of the dependence on the normalized vector potential a_0 in Eq. 5.5 and the different plasma gradient lengths at each focal location. By changing the focal location with respect to the position of the tape, the intensity of the pulse on the tape is changed and the amount of absorption from resonance and Brunel absorption is changed (as discussed in Section 5.3.2.1 and 5.3.2.2).

Table 5.1: Experimental Reflectance of S and P Polarization on VHS Tape During Focal Scan

Tape Surface	Z-Location	S/P Pol.	Reflectance	$Absorption_{Brunel+Resonance}$
VHS Back	2 mm	S	44%	
VHS Back	2 mm	P	28%	35%
VHS Back	4 mm	S	80%	
VHS Back	4 mm	P	46%	43%
VHS Back	6 mm	S	80%	
VHS Back	6 mm	P	48%	40%
VHS Back	8 mm	S	79%	
VHS Back	8 mm	P	48%	39%

5.5.4 Reflectance study: tape material comparison

A comparison of materials was studied based on the chemical make up of the tape. As discussed in Section 5.2.2, the magnetic recording tapes has a surface of plastic and a surface of Iron(III) oxide particles mixed with a bonder. By studying the PM reflectance from both sides of the tape, we were able to characterize the reflectance of a PM produced from a plastic and from a metal (Iron). The different materials have different ionization states required to produce a surface plasma. The reflectances caused by an ionization of mylar requires a higher ionization intensity that the reflectances from the Iron(III) oxide particles. The model's fitting parameters are in agreement with this as well.

It will be discussed in more detail when describing the analytic model used to fit the data (in Sec. 5.6.2), but the shape of the computer data tape's back surface reflection resembles the shape of a curve with a lower ionization intensity. So it is thought that the computer data tape either has a back coating which contains parties with a lower ionization intensity, or the light is transmitted through the 5.1 μm PEN substrate and interacts with the Iron(III) particles on the magnetic layer.

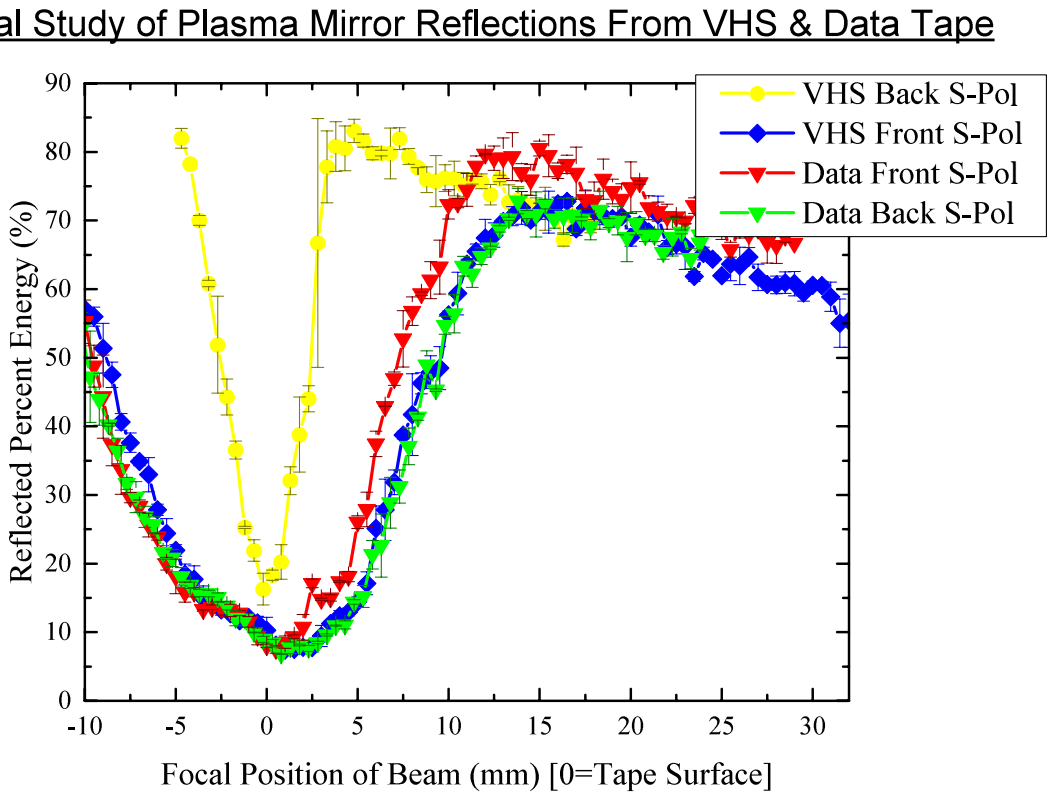

Figure 5.12: Plot showing the reflected energy from a plasma mirror reflected off both sides of a VHS tape and both sides of a computer storage tape.

5.6 Plasma mirror model

5.6.1 Laser pulse's temporal shape and focal characteristics

The laser pulse's temporal profile is made up of three regions. The 40 femtosecond peak of the pulse determines the maximum intensity on target. The coherent picosecond shoulder is created from scattering events which occur due to scattering interactions with the laser pulse and transmission through optics. The pedestal which reaches out beyond 10's of picoseconds is due to amplified spontaneous emission (ASE) within the many amplifiers. To fully characterize the laser pulse, three Gaussian functions were added together which represent each of the three regions. Each Gaussian take the form:

$$I[t] = A * e^{\frac{-(t-\mu)^2}{2\sigma^2}}. \tag{5.7}$$

The coefficients for A, μ, and σ of each of the three regions are given in Table 5.2.

The complete temporal profile of the laser pulse's intensity over the three regions was measured by a third order cross-correlating diagnostic made by Sequoia Amplified Technolo-

gies. The pulse's intensity profile in time is:

$$I[t] = I_{Tape} \times \sum_{i=1}^{3} A_i e^{\frac{-(t-\mu_i)^2}{2\sigma_i^2}}. \tag{5.8}$$

I_{Tape} is the peak intensity seen by the tape, given by

$$I_{Tape} = \frac{2W}{\pi w(z)^2 \tau}, \tag{5.9}$$

where W is the energy of the pulse in Joules, $\pi w(z)^2$ gives the area of the beam at the position of the tape, and τ is the duration of the pulse in time. For τ we use the duration of the peak of the pulse (measured by a GRENOUILLE), of 40 fs full-width half maximum (FWHM). The energy in the beam at the point of the tape is 650 mJ. These laser pulse characteristics give a peak intensity of $2 \times 10^{18} W/cm^2$.

Table 5.2: Normalized Coefficients of the three regions of the third-order cross correlator Measurement

Region of Laser Temporal Footprint	Peak	Shoulder	Pedestal
Normalized Amplitude (A)	1	3.27×10^{-4}	5.4×10^{-8}
Temporal Offset (μ)[ps]	0	3.0×10^{-1}	5.57×10^{-1}
Gaussian Width (σ)[ps]	0.017[1]	1.1	6.47

The size of the beam through focus is used to determine the intensity of the beam when it interacts with the tape. The beam waist of the TREX beam was measured to be $w_0 = 22\ \mu$m. The dependance of the beam radius through focus is given by Gaussian beam propagation as

$$w(z) = w_0 \times \sqrt{1 + \left(\frac{z}{z_R}\right)^2}. \tag{5.10}$$

Where the Rayleigh length, z_R, is found using Gaussian optics as $z_R = \frac{\pi w_0^2}{\lambda}$. The variable λ is the wavelength of light ($\lambda = 800$ nm).

5.6.2 Model's fitting parameters

The model uses three fit parameters to match the data. The first fit parameter is the ionization intensity (I_{Ionize}) needed to produce the surface plasma. Our values for ionization intensity are in agreement with previous publications of femtosecond-class laser ionization of solids [95, 96, 36]. Following ionization, the collisional electron avalanche mechanism [97, 98], discussed by G. Doumy in the creating of a PM [99], rapidly increases the plasma density above the critical density. The final two fit parameters are the expansion velocity (c_s) of the plasma electrons and the absorption percentage (α) of the input signal. The expansion velocity of the plasma is given by the ion sound speed, $c_s = \sqrt{Zk_BT_e/m_i}$. We used the ion

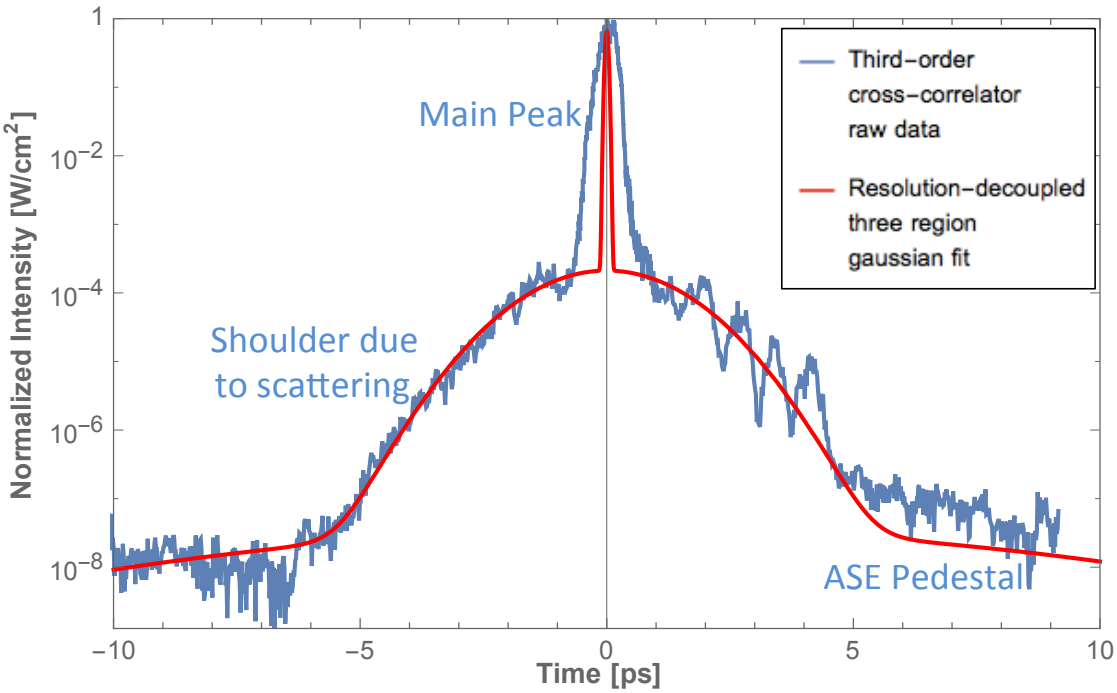

Figure 5.13: Normalized third-order cross-correlation measurement used to characterize the temporal shape of the pulse's intensity. The three regions of the cross-correlation (blue) are shown and labeled. A fit is shown of the sum of three Gaussians. The width of the main peak in our resolution-decoupled fit was 40 fs FWHM measured by a GRENOUILLE. At focus the peak intensity of the pulse was 2×10^{18} W/cm^2.

sound speed as a fitting parameter and used velocities which are in agreement with previous PM publications [99, 100, 36, 37]. The expansion velocities used to fit our experimental data are given in Table 5.3.

The ionization intensity is used to fit the width of the drop in reflectance seen when focusing within a few Rayleigh ranges from the tape (region I of Fig. 5.2), as well as the slope that the reflectance drops off, as focus is moved beyond optimal reflectance and further from the tape. The width of the drop in reflectance when focusing near the tape is due to the plasma being ionized picoseconds before the peak of the pulse arrives, and expanding into vacuum to lengths up to 300-350 nm. Since the ionization time is the cause for the change in reflectance seen between the two regions of the PM, changing the ionization level has a dramatic affect on the width of region I. This is seen in the material study of the VHS tape. The mylar side of the tape has a higher ionization intensity than Iron(III) and has a much narrower drop in reflectance. The magnetic iron(III) oxide layer requires a lower ionization intensity, which can be reached on the tape surface further from focus, and therefore produces a wider drop in reflectance around z = 0 mm.

As the focus of the laser is moved further from the tape, the intensity in the far wings of the pulse eventually drops below the ionization intensity. This results in the gradual fall off seen when focus is moved beyond the optimal reflectance position, and is explained in

Section 5.6.3 as the Spatial Reflectance term (S[z] given by Eq. 5.12); which is also dependent on the ionization intensity.

The final fit parameter is the absorption percentage (α). This parameter was taken from the experimental data as the amount of energy loss seen at the point of highest reflectance within the scan. The absorption levels seen in the study of s-polarized light (on the both sides of the VHS tape and data tape) are in agreement with the values seen in previous publications from a self-triggered PM such as Ref. [99, 20, 37]. Absorption for scans with $\alpha > 45\%$ have been addressed as p-polarization dependent Brunel and resonance absorption mechanisms.

It should also be noted that the experimental data for both surfaces of the computer data tape have a similar shape and width as the VHS front surface. The computer storage tapes have a sub-micron coating on the back of the plastic substrate s described in section 5.2.2. Due to the shape of the reflectance curve, it is thought that the ionized PM when the laser is interacting with the "back" of the computer storage tape is due to a lower ionization level such as that in the Iron surface. As suggested by some LTO tape manufactures [90], the experimental data trends (width of the reflectance dip around x = 0 mm) resemble an ionization state lower than that seen in the mylar VHS back surface. So we have chosen to use the lower ionization state for both sides of the computer storage tape.

5.6.3 Spatial reflectance term

This spatial dependence of the beam compares the radial intensity distribution of the laser spot to the ionization intensity needed to create a surface plasma. Assuming the laser spot as a Gaussian distribution of intensity, regions further from the center of the spot contain less signal than regions near the center of the spot. The spatial reflectance term, S[z], in the model calculates what percent of the beam's full spot size is above the ionization intensity needed to trigger the plasma mirror, and restricts reflection to only these regions. This term is included to match the data as the focal position z increases beyond the point of maximum reflectance and there is a slight drop in the reflectance of the beam.

To calculate the radius which ionization occurs, solve for R_{Ionize} in the equation

$$I_{Tape} * e^{-2R^2_{Ionize}/w(z)^2} = I_{Ionization}. \tag{5.11}$$

Then we calculate the percent of the laser's spatial mode which is above the ionization level, by taking the integral

$$S[z] = \frac{\int_0^{R_{Ionize}} (I_{Tape} * e^{-2r^2/w(z)^2}) r \; dr}{\int_0^{\infty} (I_{Tape} * e^{-2r^2/w(z)^2}) r \; dr}. \tag{5.12}$$

Here the numerator solves for only the ionized portion of the spot size, and the denominator calculates the entire intensity within the full spot.

5.6.4 Reflectance algorithm

The algorithm used in the analytic model to fit the reflectance data draws from the analytic model used by G. G. Scott *et al.* in Reference [20]. The intensity reflected is calculated from

$$I_{Reflected} = I_0 \ \exp\left[-\left(\frac{4\pi\sigma_x}{\lambda}\cos\theta_i\right)^2\right] \tag{5.13}$$

at each focal position z. In order to find the roughness σ_x of the PM surface, the algorithm goes as follows:

- The time at which ionization occurs (t_0) must be solved for at each radial position (r) within the spot size on the tape. This is done by assuming a Gaussian spot on the tape of the form $e^{-2r^2/w(z)^2}$ and the temporal intensity profile I[t] given in Sec. 5.6.1 at a given z location[2]. The ionization time is given by the time which the function $I[z_{Focus}, t] * e^{-2r^2/w(z)^2} = I_{Ionization}$. This gives an array for the ionization time t_0 at each radial position (r) within the spot size on the tape. The results of this step are seen for a focal scan from VHS back in Fig. 5.14.

- By taking the ionization time at each radial position, r, and assuming the expansion velocity using the fitting parameter c_s, the position of the PM surface when the peak of the laser pulse arrives (at time t=0) is solved for at each radial position, r. The results of this step are seen for a focal scan from VHS back in Fig. 5.15.

- Once the shape of the PM surface is found, the roughness is calculated by taking the standard deviation of the PM surface positions. The standard deviation is taken only for the points where the PM has ionized the surface and the PM has expanded by $> 0\ nm$. This gives the surface roughness (σ_x), which will be used to find the reflectance.

- This process is repeated for each value of z within the focal scan; resulting in a value of σ_x at each z-location. We call this $\sigma_x[z]$.

Once the plasma surface roughness σ_x is found for the ionized PM, we recall the equation for the reflected intensity (Eq. 5.13). Lastly, solving for $I_{Reflected}$ at each z-location within the focal scan.

The value of $I_{Reflected}[z]/I_0$ gives the value of the reflected intensity for the reflection of the entire 2D spot size. However, we calculated (in section 5.6.3) the amount of the mode which reaches ionization as S[z]. Therefore we calculate the reflectance as

$$R = (1-\alpha)\frac{I_{Reflected}[z]}{I_0}S[z]. \tag{5.14}$$

[2]To scale the time-resolved intensity function (I[t]) for the focus positioned at a given z location $I[z_{Focus}, t] = I[t] \times \frac{w(0)^2}{w(z)^2}$

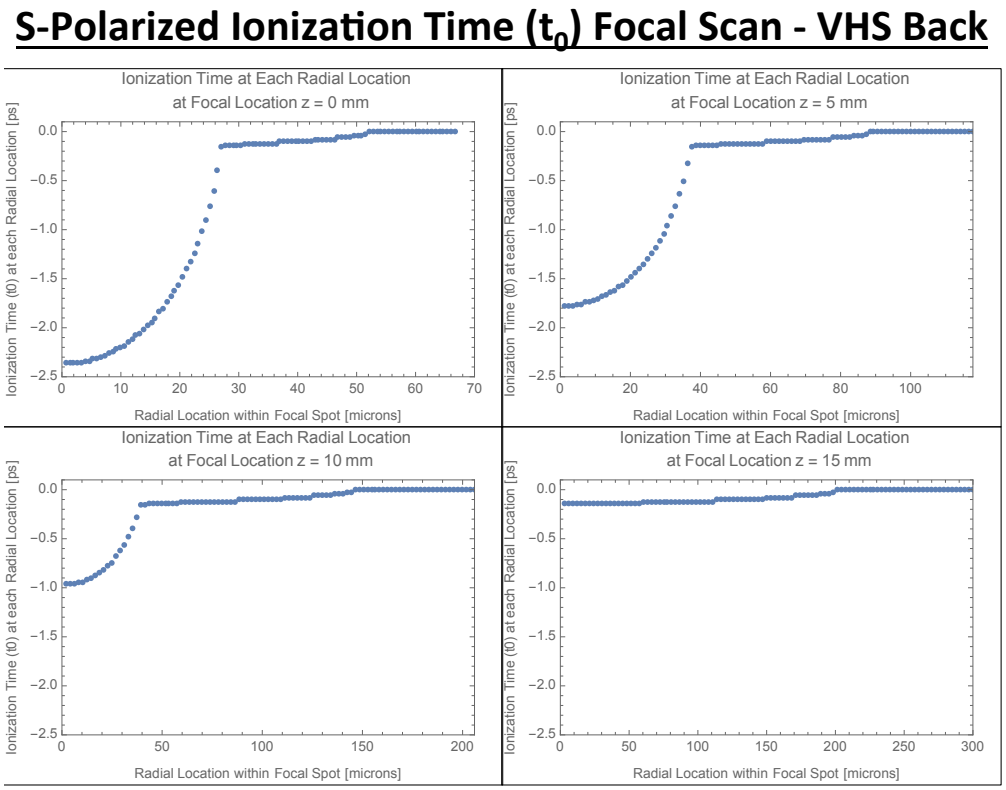

Figure 5.14: Plots showing the ionization time at each radius (R) within the spot size on the tape using s-polarized light from the VHS back surface. Each plot is at a different focal position with respect to the tape surface (at z = 0 mm). The ionization intensity in this case is 6.4×10^{13} W/cm^2

5.6.5 Model fit parameter results

The results for each of the fitting parameters used to fit the PM experimental data are given in Table 5.3. The resulting plots for each of the reflectance model using the fit parameters from Table 5.3 are given in Fig 5.16 for the VHS tape polarization study and in Fig. 5.17 for the study of the different tape materials.

The higher ionization intensity for the VHS back is responsible for the narrow dip in reflectance when the focus is positioned on or near the tape surface (tape surface at x=0). The maximum reflectance of the VHS back is produced when the focus is 4 mm (2 Rayleigh lengths) from the tape surface. The other materials have a lower ionization intensity, which allows for the solid to be ionized at the ideal time when the focus is positioned further from tape surface. The maximum reflectance of the VHS front and the computer data tape is produced when the focus is 14 mm from the tape surface.

The higher ionization intensity of the VHS back also produces a higher electron expansion velocity. However, since the surface is ionized at a higher intensity than the VHS front and computer tape, the electrons have less time to expand, because they become ionized later in time and closer to the peak of the laser pulse. This results in the electrons expanding

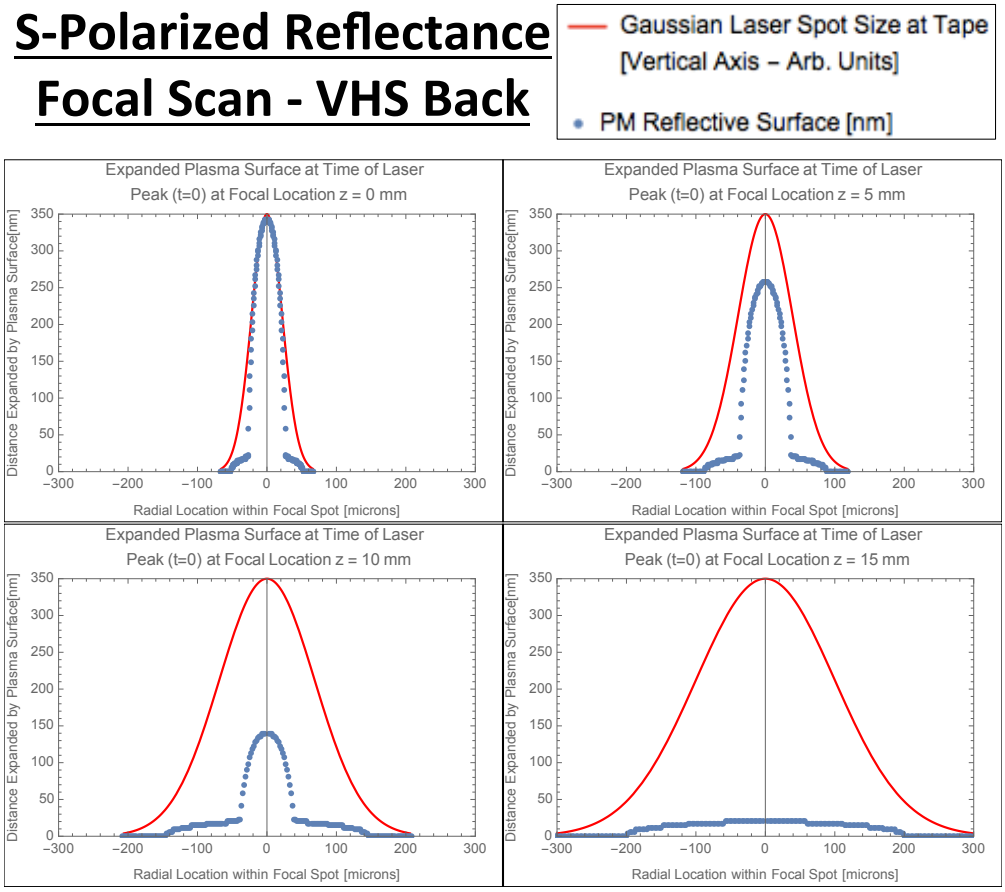

Figure 5.15: Plots showing the shape of the PM reflective surface for a focal scan using s-polarized light from the VHS back surface. The expansion velocity in this case is 1.8×10^7 cm/s (or equivalently 180 nm/ps).

Table 5.3: Fit parameters to each of the material surfaces studied during plasma mirror characterization

PM Surface	Pol.	Ionization Intensity $[W/cm^2]$	Expansion Velocity [cm/s]	Absorption [%]
VHS Back	S	6.4×10^{13}	1.8×10^7	18
VHS Back	P	6.4×10^{13}	1.8×10^7	48
VHS Front	S	1.6×10^{13}	1.5×10^7	19
VHS Front	P	1.6×10^{13}	1.5×10^7	46
Data Tape Back[3]	S	1.6×10^{13}	1.5×10^7	24
Data Tape Front	S	1.6×10^{13}	1.5×10^7	18

a shorter distance in case of the VHS back, and the minimum reflectance of $18 - 20\%$ is seen when the focus is positioned at the surface of the VHS back tape. The VHS front and computer storage tapes have more time to expand following ionization and result in a

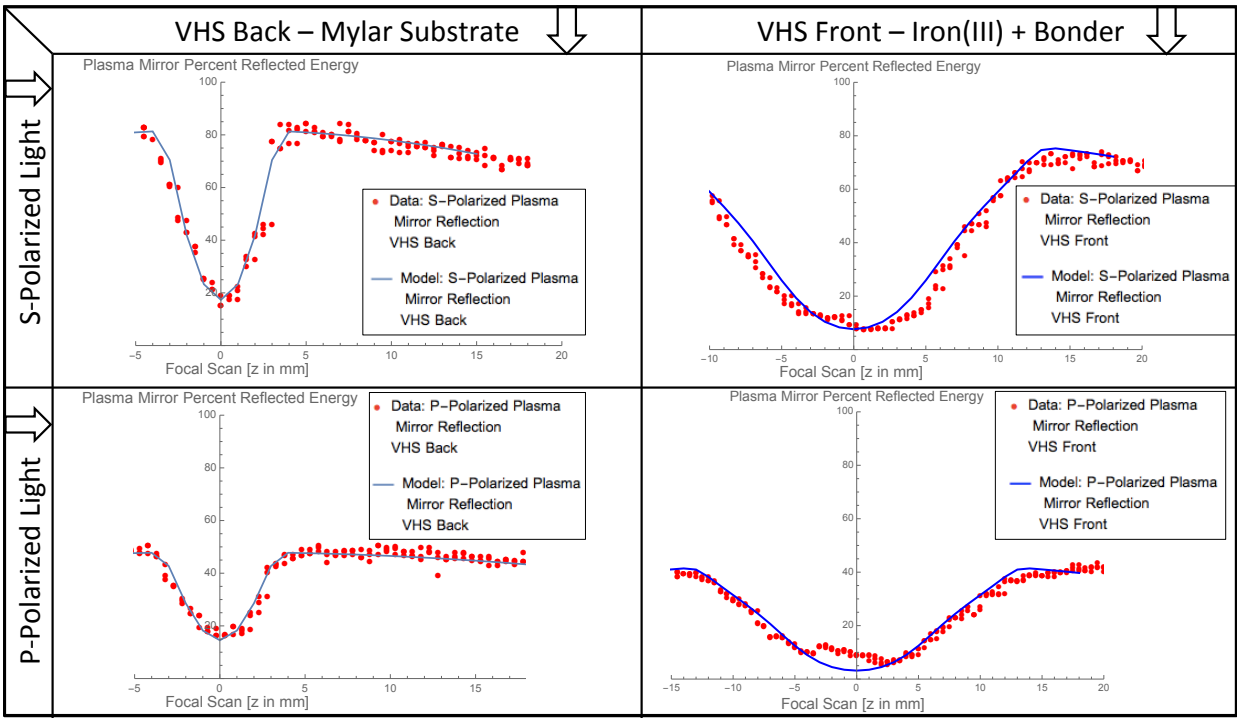

Figure 5.16: Plots showing the match between the PM Model and the experimental data of VHS tape front and back surfaces, using S and P-polarized light.

minimum reflectance of $5-10\%$ when the focus is positioned at the surface of the tape.

The absorbed energy values are used to fit the vertical range of the experimental data. Our maximum reflectance of 82% is a result of the picosecond contrast of the laser and the high ionization intensity needed to ionize the VHS back surface. This reflectance matches the values previously published with a single pulse triggering and reflecting from a PM.

A plot showing the published reflectance values from different PM studies and the year they were published is given in Fig. 5.18. There is a clear trend that the published values of reflectance has increased continually over the past 10 to 15 years. The maximum reflectance seen from a PM is 96% which was published by G. G. Scott *et al.* in Ref. [20]. This record PM reflectance was produced by preionizing the PM surface using a controlled prepulse up to 3 picoseconds before the peak of the laser arrives.

5.7 Summary

The tape drive that has been developed within the BELLA Center at the Lawrence Berkeley National Lab was designed to be implemented on the staged acceleration experiment. The tape is able to spool a new, undamaged surface into the beamline following each successive laser shot. This helps overcome the challenge that is created for PM experiments, which is that the laser damages the surface, significantly reducing the lifetime of an optic.

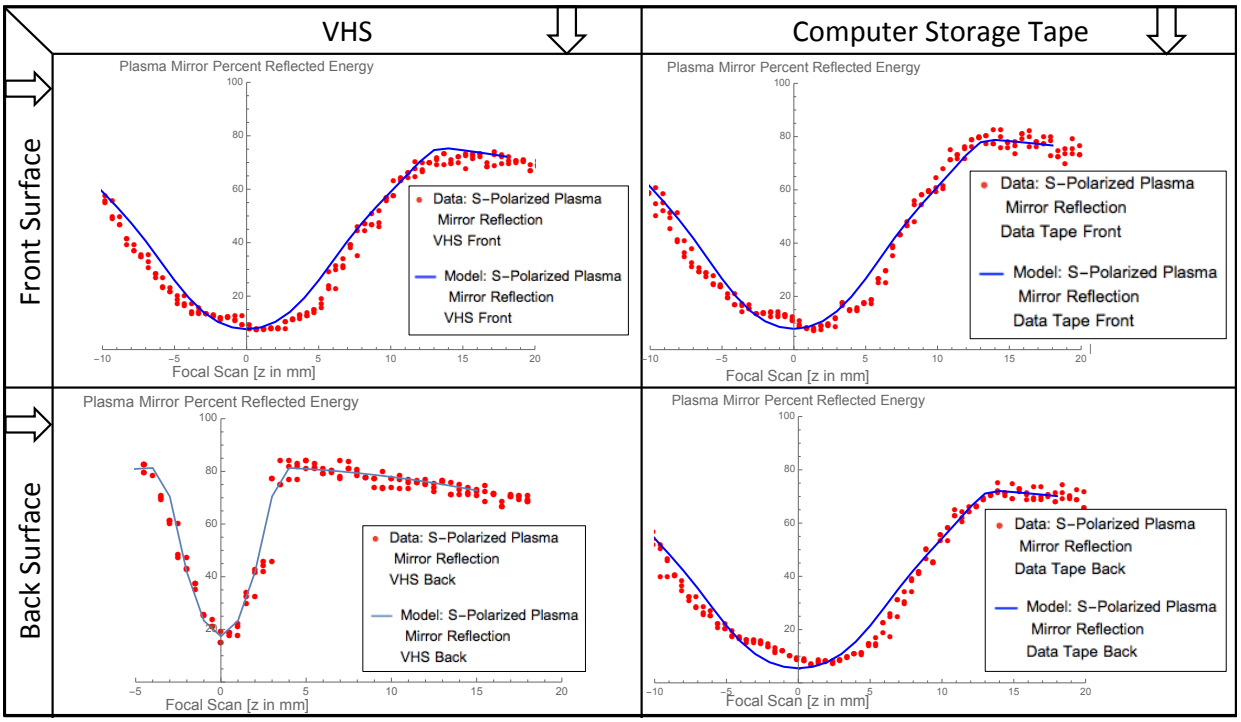

Figure 5.17: Plots showing the match between the PM Model and the experimental data of S-polarized light on the front and back surfaces of the VHS and computer data storage tape.

The tape can be spooled so that 10's of thousands of shots can be fired before needing to replace the PM target.

The pointing study showed that the pointing fluctuations caused by the PM are $\leq$1 mrad ($\theta_{PM} = 940$ μrad in x and $\theta_{PM} = 1.0$ mrad in y). Nearly a third of this pointing fluctuation is attributed to the spooling mechanics of the tape drive. This value was measured to be $\theta_{TapeMotion} = 310$ μrad by measuring a non-ionizing HeNe beam reflected from the solid tape.

The reflectance polarization study of the PM gave a direct comparison to s and p-polarized light from the front and back surface of the VHS tape. Since Brunel and resonance absorption are dependent on the p-polarized laser intensity and the plasma gradient length, the value of absorbed light from Brunel and resonance absorption can be found at each z location by solving $A_{B+R}[z] = 1 - \frac{R_{P-pol}[z]}{R_{S-pol}[z]}$. When the laser beam was focused more than 1 Rayleigh length from the tape surface, the experimental data gives an absorption of $A_{B+R}[z] = 39$+/- 4%. This experimental data also showed a peak in reflectance from the VHS Back surface at +/- 4 mm from the tape surface. So a VHS Back surface should be placed 4 mm from the final focus location. This makes the tape based plasma mirror a novel optic for experiments which require beams to be pointed near their final focus.

The reflectance material study showed similar reflectance curved for both sides of the computer storage tape and the front surface of the VHS tape. These curves are each characterized with a peak in reflectance when focusing 14 mm from the tape surface. Since

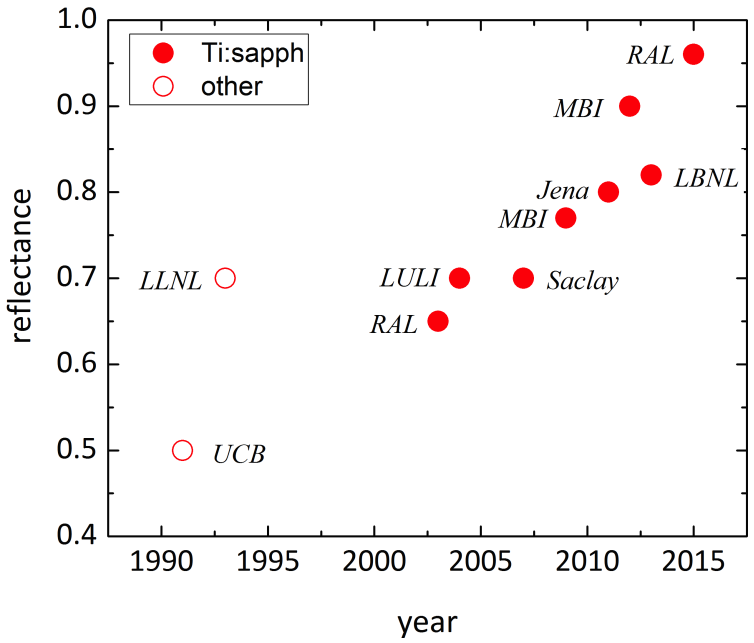

Figure 5.18: Plots showing the published values of reflectances in a given year since the first experimental PM results in 1991. The publications in the figure refer to: 1991 UCB Ref. [19], 1993 LLNL Ref. [21], 2003 RAL Ref. [37], 2004 LULI Ref. [99], 2007 Saclay Ref. [101], 2009 MBI Ref. [102], 2011 Jena Ref. [103], 2013 MBI Ref. [104], 2014 LBNL refers to data from this chapter, and 2015 RAL Ref. [20].

the beam is much larger on the tape at these locations, this indicates that the ionization intensity for these materials is lower than that of the VHS Back surface.

The plasma mirror model provided a match between the experimental data and a statistical treatment of electromagnetic waves incident on a normally distributed surface. The model's three fit parameters (I_{Ionize}, c_s, and α) each affect the reflectance curve in unique ways. The Ionization intensity determines the wide of the dip around x = 0 mm, and the rolloff of reflectance observed at focal locations beyond that of maximum reflectance. The expansion velocity determines the shape/depth of the dip around x = 0 mm, with a sharper and deeper drop in intensity for higher expansion velocities and a slower and shallow dip for lower expansion velocities. The numbers used to fit the data matched the numbers used in previous publications of PM reflectance studies. Lastly, the absorption values were taken from the experimental data as the loss in energy from the point of maximum reflectance. Our values of $\alpha = 18 - 24\%$ agree with the values published previously.

Chapter 6

Summary and Conclusion

The major results described in this thesis are from experimental campaigns that investigated laser interactions with tape. These efforts were focused towards two future applications for LPAs:

- Surface high-harmonic generated (SHHG) source for seeding an LPA-based free-electron laser (FEL)
- Tape based plasma mirror (PM) reflector, placed within centimeters of focus, for a two staged LPA accelerator.

6.1 Summary

The processes of stimulated emission and amplification were described in Chapter 2 to understand the components that make up the 50 TW TREX laser system at the BELLA Center. Chirped pulse amplification was described as the way the BELLA Center's laser systems are able to reach up to 40 J of energy with pulse lengths as short as 40 fs; producing powers up to 10^{15} J/s. The TREX 50 TW laser system, and the two beamlines which it feeds (the staging and undulator beamlines) were described. Finally, the process of laser plasma acceleration (LPA) [or laser wakefield acceleration (LWFA)] was described by focusing the laser pulse to produce a strong ponderomotive force. The ponderomotive of an ultra-intense laser able to push free plasma electron off the propagation axis, creating a wakefield behind the laser pulse. Next, one of the many injection mechanisms is used to trap plasma electron in the wakefield of the pulse. This process of LPA is discussed throughout this thesis as the mechanism used to produce relativistic electron bunches.

Next, it was shown in Chapter 3 that the THUNDER undulator has successfully produced extreme ultra-violet radiation by oscillating LPA electron bunches. The spectrum of spontaneous radiation at photon energies from 15 eV to beyond 100 eV produced from a broad energy spread bunch was measured. A discussion of other undulator properties were

also outlined. A calculation was carried out to show how the undulator harmonics are created, with even harmonics emitted off-axis and odd harmonics on-axis. Lastly, a theoretical approach of inferring the energy spread and emittance of the electron bunch from the spectrum of the spontaneous emmission was described. To carry this experiment out, the energy spread of the bunch should decrease significantly from what was reported here.

Tape-based SHHG was discussed in Chapter 4 as a novel seed source for an FEL which removes the need for transport optics of seed photons and optics needed to overlap the seed beam and the electron bunch. This is achieved by producing the SHHG signal at the undulator entrance and in the electron beamline, rather than producing the $\lambda = 53$ nm signal upstream and coupling the light into the undulator with grazing-incidence reflective UV optics. The ideal tape-based FEL seed source would be as thin as possible to minimize the growth of the electron bunch's emittance, produce the highest efficiency of IR light to the seed photons ($\lambda = 53$ nm), and minimize the seed pulse's divergence. These properties were studied to find the best tape material which is capable of seeding an LPA-based free-electron laser.

The results of the tape-based SHHG campaign led to the measurement of the surface roughness of each of the tape materials used in the study. A clear correlation between the surface roughness at spatial wavelengths smaller than 50 μm (the spot size on the tape) and SHHG divergence was found. The maximum 15th-order conversion efficiency is needed, because this wavelength ($\lambda = 53$ nm) is resonant with the first order of undulator radiation when an electron beam of 310 MeV is sent through the THUNDER Undulator. The highest efficiency produced from a tape material was 6.5×10^{-7} from the IR-drive laser to the $\lambda = 53$ nm. This efficiency was found using the magnetic "front" surface of a VHS tape, which produced an SHHG beam divergence of 11 mrad. Lastly, the results of a microbunching model were used to show that the CWE signal which was produced from VHS tape was powerful enough to enhance microbunching in the current length of the THUNDER undulator.

The second laser-tape application which was experimentally studied was the tape based plasma mirror (PM) reflections. This PM design of using thin tape as the replenishing reflectic optic is used on the staged acceleration campaign to couple laser pulses into and out of the staging beamlines near focus. Although a more conventional use for a plasma mirror is to enhance the contrast of a laser pulse using a polished glass substrate, the tape-based plasma mirror is a thin, reflective, steering optic with a lifetime of 1000's of shots. Similar to the SHHG study, the thin spooling tape is used because it is able to propagate an electron beam though the materials of tape.

Both VHS tape and computer storage tape were experimentally studied in Chapter 5. Focal scans were made to change the intensity of the laser pulses on the tape while keeping the pulse power constant. The reflectance measurements from both sides of the two tapes were taken with input light of s-polarization. This measurement showed that maximum reflectance of 82% was produced from the VHS front surface. This was achieved when focusing 4 mm from the tape, and therefore the VHS front surface should be placed 4 mm from the final focus using the current laser properties. A characterization of the tape-based

PM was also studied for different input laser polarizations. As expected, p-polarized light had a lower reflectance from the PM due to the additional absorption mechanisms of Brunel and resonance absorption, which only occur for p-polarized light input on a plasma density gradient. A discussion of this was given in Section 5.6.2. Lastly, A model of the PM was developed and used to quantify the each of the parameter studies. Using fit parameters of the ionization intensity (I_{Ionize}) needed to produce the surface plasma, the expansion velocity (c_s) of the plasma electrons, and the absorption percentage (α) of the input signal, each of the reflectance curves is understood and fit well to the model. The model shows the importance of the ionization time of the surface plasma within the coherent shoulder of the femtosecond pulses.

6.2 Future Research

The future research which is needed to producing a seeded LPA-based FEL should focus on producing electron bunches with a narrower energy spread or engineering ways to manipulate the bunch such that the slice energy spread is reduced. Few-percent energy spread beams have been produced on the undulator beamline by tailoring the density of the plasma longitudinally within a discharged capillary [40]. Producing beams of this quality and sending them through the undulator should produce an spectrum of spontaneous undulator emission which has resolvable harmonics of the undulator's fundamental wavelength. If producing stable beams of this quality is a greater challenge than increasing the charge of a beam, engineering methods could be used to reduce the effective slice energy spread of the electron bunch. For example, a magnetic chicane is a device that works much like an optical stretcher. The chicane can separate the energies within an electron bunch in either time or space by creating different path lengths for different energy electrons. Once the electron bunch is stretched, the energy spread within a longitudinal slice of the bunch will effectively decrease. This stretching of the electron bunch will, however, requires an increase in the charge of the overall bunch.

The future research of the tape based plasma mirror is currently very optimistic. The results of the plasma mirror experiment have been implemented on the current staging experimental setup. Recent results have shown successful post acceleration of the electron beam in the second stage of the experiment [28]. This experimental success opens the door for a few different ways to proceed. First, the capability to decelerate an electron beam is also very interesting, as this could be a way to reduce the energy of a bunch to the few-MeV level, reducing the shielding requirements needed to contain the radiation. Deceleration occurs when the electron bunch interacts with the decelerating region of the wakefield in the second stage. Deceleration was shown in the staging experiments, however the broad energy spread of the electron bunches prevents a deceleration of the entire bunch. A narrower energy spread would help to produce a visible drop in maximum energy of an electron bunch.

Another experiment that should follow the success of staging is producing a 3+ stage accelerator. Staging was an experiment designed to overcome one of the basic principle

drawbacks of laser plasma acceleration, which is laser depletion. Since dephasing can be overcome by longitudinal plasma density tailoring and diffraction can be overcome by laser guiding, if laser depletion is overcome, then there seems to be no upper limit to the electron energy an LPA can produce. Going from a two staged accelerator to a three staged accelerator seems to be a natural progression, however there were many challenges faced and overcame in an effort to produce a successful two staged accelerator. Adding a third stage will not be trivial. First, simulations should run to find the optimum conditions (the laser intensities, plasma densities, etc.) of running a three stage LPA. Simulations will be much simpler than the experimental campaign, due to the reduced number of engineering challenges of running a simulation. Following simulations, an extensive design should be made that allows the scientists to control the maximum amount of degrees of freedom, including the time delay of each beamline, the compression of the pulse driving each stage separately, and full 3-directional and 3-angle positioning of each of the three stages. Further implementation of the experiment has no major differences than the original staging experiment's task of adding an extra acceleration stage, but the lessons learned by the experimentalists in the BELLA Center will be crucial knowledge in moving to a 3+ staged accelerator.

The third experiment which should be explored following the staging on the 50 TW TREX beamline is to carry out a staging experiment on the BELLA PW laser system. The BELLA laser is capable of producing petawatt level pulses at 1 Hz. This system set the record for LPA electron energy with a maximum energy of 4.25 GeV [2]. If an experiment were carried out on BELLA such that a two stage accelerator reached near the 10 GeV level ($\sim$ 5 GeV from each stage), and experiments were carried out to show the success of a 3+ staged-LPA, the potential for high energy, multi-staged LPA systems could create applications within high energy density (HED) physics.

Bibliography

[1] C. G. R. Geddes et al. "High quality electron beams from a plasma channel guided laser wakefield accelerator". In: *Nature* 431.7008 (2004), pp. 538–541.

[2] W. P. Leemans et al. "Multi-GeV Electron Beams from Capillary-Discharge-Guided Subpetawatt Laser Pulses in the Self-Trapping Regime". In: *Physical review letters* 113.24 (2014), p. 245002.

[3] E. Esarey, C. B. Schroeder, and W. P. Leemans. "Physics of laser-driven plasma-based electron accelerators". In: *Rev. Mod. Phys.* 81 (2009), pp. 1229–1285.

[4] MS Bakeman et al. "Undulator-Based Laser Wakefield Accelerator Electron Beam Energy Spread and Emittance Diagnostic". In: *ADVANCED ACCELERATOR CONCEPTS: 14th Advanced Accelerator Concepts Workshop*. Vol. 1299. 1. AIP Publishing. 2010, pp. 133–138.

[5] B. Shaw et al. "Undulator radiation from laser-plasma-accelerated electron beams". In: *Advanced Accelerator Concepts Proceedings*. Vol. 1507. New York: AIP, 2012, pp. 310–314. DOI: 10.1063/1.4773713.

[6] James Brau, Yasuhiro Okada, and Nicholas Walker. "Ilc reference design report volume 1-executive summary". In: *arXiv preprint arXiv:0712.1950* (2007).

[7] Gerald Aarons et al. *International Linear Collider reference design report. Volume 2: Physics at the ILC*. Tech. rep. SLAC National Accelerator Laboratory (United States). Funding organisation: US DOE Office of Science (United States), 2011.

[8] Nan Phinney, Nobukasu Toge, and Nicholas Walker. "ILC reference design report volume 3-accelerator". In: *arXiv preprint arXiv:0712.2361* (2007).

[9] Ties Behnke et al. "Ilc reference design report volume 4-detectors". In: *arXiv preprint arXiv:0712.2356* (2007).

[10] M. Aicheler. *A Multi-TeV linear collider based on CLIC technology: CLIC Conceptual Design Report*. CERN Geneva, Switzerland, 2012.

[11] R Tomas. "Overview of the compact linear collider". In: *Physical Review Special Topics-Accelerators and Beams* 13.1 (2010), p. 014801.

[12] W. P. Leemans et al. "GeV electron beams from a centimetre-scale accelerator". In: *Nature Physics* 2 (2006), pp. 696–699.

[13] SY Kalmykov et al. "Laser wakefield electron acceleration on Texas petawatt facility: Towards multi-GeV electron energy in a single self-guided stage". In: *High Energy Density Physics* 6.2 (2010), pp. 200–206.

[14] J. Faure et al. "A laser plasma accelerator producing monoenergetic electron beams". In: *Nature* 431.7008 (2004), pp. 541–544.

[15] Paul Gibbon. *Short pulse laser interactions with matter*. World Scientific Publishing Company, 2004.

[16] William L. Kruer. *The Physics of Laser Plasma Interactions*. Redwood City, CA: Addison-Wesley, 1988.

[17] W. P. Leemans et al. "Plasma guiding and wakefield generation for second-generation experiments". In: *IEEE Trans. Plasma Sci.* 24 (1996), pp. 331–342.

[18] Satomi Shiraishi. *Investigation of Staged Laser-plasma Acceleration*. Springer, 2014.

[19] Henry C Kapteyn et al. "Prepulse energy suppression for high-energy ultrashort pulses using self-induced plasma shuttering". In: *Optics letters* 16.7 (1991), pp. 490–492.

[20] GG Scott et al. "Optimization of plasma mirror reflectivity and optical quality using double laser pulses". In: *New Journal of Physics* 17.3 (2015), p. 033027.

[21] Sterling Backus et al. "Prepulse suppression for high-energy ultrashort pulses using self-induced plasma shuttering from a fluid target". In: *Optics letters* 18.2 (1993), pp. 134–136.

[22] Dmitriy Panasenko et al. "Demonstration of a plasma mirror based on a laminar flow water film". In: *J. Appl. Phys.* 108.4 (2010), p. 044913.

[23] F. Brunel. "Not-so-resonant, resonant absorption". In: *Phys. Rev. Lett.* 59 (1987), pp. 52–55. URL: http://dx.doi.org/10.1103/PhysRevLett.59.52.

[24] M. S. Bakeman et al. "Undulator-Based Laser Wakefield Accelerator Electron Beam Energy Spread and Emittance Diagnostic". In: *AIP Conference Proceedings* 1299 (2010), p. 133.

[25] B. H. Shaw et al. "High-peak-power surface high-harmonic generation at extreme ultra-violet wavelengths from a tape". In: *Journal of Applied Physics* 114.4, 043106 (2013), pp. –. DOI: http://dx.doi.org/10.1063/1.4816574.

[26] J van Tilborg et al. "Spectral characterization of laser-driven solid-based high harmonics in the coherent wake emission regime". In: *Optics letters* 38.20 (2013), pp. 4026–4029.

[27] C. B. Schroeder. Private Communications. 2013.

[28] S. Steinke et al. "Multistage coupling of independent laser plasma accelerators". In: *Nature Physics* (2015), Submitted.

[29] J. van Tilborg et al. "Active Plasma Lensing for Relativistic Laser-Plasma-Accelerated Electron Beams". In: *Phys. Rev. Lett.* 115 (18 2015), p. 184802. DOI: 10.1103/PhysRevLett.115.184802. URL: http://link.aps.org/doi/10.1103/PhysRevLett.115.184802.

[30] B. H. Shaw et al. "Reflectance characterization of tape-based plasma mirrors". In: *Physics of Plasmas* (2015), In Preparation.

[31] Donna Strickland and Gerard Mourou. "Compression of amplified chirped optical pulses". In: *Optics communications* 55.6 (1985), pp. 447–449.

[32] GI Petrov et al. "Cross-polarized wave generation by effective cubic nonlinear optical interaction". In: *Optics letters* 26.6 (2001), pp. 355–357.

[33] N Minkovski et al. "Nonlinear polarization rotation and orthogonal polarization generation experienced in a single-beam configuration". In: *JOSA B* 21.9 (2004), pp. 1659–1664.

[34] A. Jullien et al. "10^{-10} temporal contrast for femtosecond ultra-intense lasers by cross-polarized wave generation". In: *Opt. Lett.* 30.8 (2005), pp. 920–922.

[35] F Quéré et al. "Coherent wake emission of high-order harmonics from overdense plasmas". In: *Phys. Rev. Lett.* 96.12 (2006), p. 125004.

[36] B-TV Vu, A Szoke, and OL Landen. "Time-resolved probing of electron thermal transport in plasma produced by femtosecond laser pulses". In: *Physical review letters* 72.24 (1994), p. 3823.

[37] Ch Ziener et al. "Specular reflectivity of plasma mirrors as a function of intensity, pulse duration, and angle of incidence". In: *Journal of applied physics* 93.1 (2003), pp. 768–770.

[38] K. Nakamura et al. "Broadband single-shot electron spectrometer for GeV-class laser-plasma-based accelerators". In: *Rev. Sci. Instrum.* 79 (2008), p. 053301.

[39] T. Tajima and J. M. Dawson. "Laser Electron Accelerator". In: *Phys. Rev. Lett.* 43.4 (1979), pp. 267–270.

[40] AJ Gonsalves et al. "Tunable laser plasma accelerator based on longitudinal density tailoring". In: *Nature Physics* 7.11 (2011), pp. 862–866.

[41] Carlo Benedetti et al. "Quasi-matched propagation of ultra-short, intense laser pulses in plasma channels". In: *Physics of Plasmas (1994-present)* 19.5 (2012), p. 053101.

[42] David T. Attwood. *Soft x-rays and extreme ultraviolet radiation: principles and applications*. Cambridge, UK: Cambridge University Press, 1999.

[43] V. Ayvazyan et al. "First operation of a free-electron laser generating GW power radiation at 32 nm wavelength". In: *Eur. Phys. J. D* 37 (2006), p. 297.

[44] M Zepf et al. "Bright quasi-phase-matched soft-X-ray harmonic radiation from argon ions". In: *Phys. Rev. Lett.* 99.14 (2007), p. 143901.

[45] A McPherson et al. "Studies of multiphoton production of vacuum-ultraviolet radiation in the rare gases". In: *JOSA B* 4.4 (1987), pp. 595–601.

[46] D. Von der Linde et al. "Generation of high-order harmonics from solid surfaces by intense femtosecond laser pulses". In: *Physical Review A* 52.1 (1995), pp. 25–27.

[47] A. Tarasevitch et al. "Generation of high order spatially coherent harmonics from solid targets by femtosecond laser pulses". In: *Technical Digest. Summaries of Papers Presented at the Quantum Electronics and Laser Science Conference, 1999. QELS'99.* IEEE. 1999, pp. 93–94.

[48] A. Tarasevitch et al. "Generation of high-order spatially coherent harmonics from solid targets by femtosecond laser pulses". In: *Phys. Rev. A* 62 (2000), p. 023816.

[49] B. Dromey et al. "Bright Multi-keV Harmonic Generation from Relativistically Oscillating Plasma Surfaces". In: *Phys. Rev. Lett.* 99.8, 085001 (2007), p. 085001. DOI: 10.1103/PhysRevLett.99.085001. URL: http://link.aps.org/abstract/PRL/v99/e085001.

[50] Y. Nomura et al. "Attosecond phase locking of harmonics emitted from laser-produced plasmas". In: *Nature Physics* 5 (2009), pp. 124 –128.

[51] K Eidmann et al. "Fundamental and harmonic emission from the rear side of a thin overdense foil irradiated by an intense ultrashort laser pulse". In: *Physical Review E* 72.3 (2005), p. 036413.

[52] U. Teubner et al. "Anomalies in high-order harmonic generation at relativistic intensities". In: *Physical Review A* 67.1 (2003), p. 013816.

[53] U Teubner et al. "Harmonic emission from the rear side of thin overdense foils irradiated with intense ultrashort laser pulses". In: *Phys. Rev. Lett.* 92.18 (2004), p. 185001.

[54] M. Zepf et al. "Role of the plasma scale length in the harmonic generation from solid targets". In: *Physical Review E* 58.5 (1998), pp. 5253–5256.

[55] P. Monot et al. "High-order harmonic generation by nonlinear reflection of an intense high-contrast laser pulse on a plasma". In: *Optics letters* 29.8 (2004), pp. 893–895.

[56] PA Norreys et al. "Efficient extreme UV harmonics generated from picosecond laser pulse interactions with solid targets". In: *Phys. Rev. Lett.* 76.11 (1996), pp. 1832–1835.

[57] W. P. Leemans. Private Communications. 2011.

[58] C. Huang et al. "Hosing Instability in the Blow-Out Regime for Plasma-Wakefield Acceleration". In: *Phys. Rev. Lett.* 99.25 (2007), p. 255001.

[59] G. Lambert et al. "Injection of harmonics generated in gas in a free-electron laser providing intense and coherent extreme-ultraviolet light". In: *Nature Physics* 4 (2008), pp. 296–300.

[60] Z. Huang, Y. Ding, and C. B. Schroeder. "Compact X-ray Free-Electron Laser from a Laser-Plasma Accelerator Using a Transverse-Gradient Undulator". In: *Phys. Rev. Lett.* 109 (2012), p. 204801.

[61] J. Bödewadt et al. "sFLASH - first results of direct seeding at Flash". In: *Proceedings of FEL 2010*. www.JACoW.org: JACoW, 2010.

[62] Eiji Takahashi et al. "Generation of highly coherent submicrojoule soft x rays by high-order harmonics". In: *Phys. Rev. A* 66 (2002), 021802(R).

[63] A. Borot et al. "High-harmonic generation from plasma mirrors at kilohertz repetition rate". In: *Opt. Lett.* 36.8 (2011), p. 1461.

[64] AR Maier et al. "Demonstration Scheme for a Laser-Plasma-Driven Free-Electron Laser". In: *Physical Review X* 2.3 (2012), p. 031019.

[65] C. B. Schroeder et al. "Application of laser-plasma accelerator beams to free-electron lasers". In: *Proceedings of FEL 2012*. www.JACoW.org: JACoW, 2012.

[66] H.-P. Schlenvoigt et al. "A compact synchrotron radiation source driven by a laser-plasma wakefield accelerator". In: *Nature Physics* 4 (2008), pp. 130–133.

[67] M. Fuchs et al. "Laser-driven soft-X-ray undulator source". In: *Nature Physics* 5 (2009), pp. 826–829.

[68] C. B. Schroeder et al. "Free-electron laser driven by the LBNL laser-plasma accelerator". In: *Advanced Accelerator Concepts*. Ed. by C. B. Schroeder, E. Esarey, and W. Leemans. Vol. 1086. New York: AIP, 2009, pp. 637–642.

[69] C Thaury and F Quéré. "High-order harmonic and attosecond pulse generation on plasma mirrors: basic mechanisms". In: *J. Phys. B: At. Mol. Opt. Phys.* 43.21 (2010), p. 213001.

[70] So V Bulanov, NM Naumova, and F Pegoraro. "Interaction of an ultrashort, relativistically strong laser pulse with an overdense plasma". In: *Physics of Plasmas* 1 (1994), p. 745.

[71] J Bierbach et al. "Generation of 10 W relativistic surface high-harmonic radiation at a repetition rate of 10 Hz". In: *New Journal of Physics* 14.065005 (2012), p. 065005.

[72] Z.M. Sheng, K. Mima, and J. Zhang. "Powerful terahertz emission from laser wake fields excited in inhomogeneous plasmas". In: *Physics of plasmas* 12 (2005), p. 123103.

[73] C. Grebogi, V. K. Tripathi, and H. Chen. "Harmonic generation of radiation in a steep density profile". In: *Phys. Fluids* 26 (1983), pp. 1904–1908. URL: `http://dx.doi.org/10.1063/1.864337`.

[74] F. Quéré et al. "Phase Properties of Laser High-Order Harmonics Generated on Plasma Mirrors". In: *Phys. Rev. Lett.* 100 (2008), p. 095004.

[75] JP Freidberg et al. "Resonant absorption of laser light by plasma targets". In: *Physical Review Letters* 28.13 (1972), p. 795.

[76] C. Thaury et al. "Plasma mirrors for ultrahigh-intensity optics". In: *Nature Physics* 3 (2007), pp. 424–429.

[77] R Hörlein et al. "High harmonics from solid surfaces as a source of ultra-bright XUV radiation for experiments". In: *Plasma Physics and Controlled Fusion* 50.12 (2008), p. 124002.

[78] T. A. Savas et al. "Large-area achromatic interferometric lithography for 100 nm period gratings and grids". In: *Journal of Vacuum Science Technology B: Microelectronics and Nanometer Structures* 14.6 (1996), pp. 4167 –4170. ISSN: 1071-1023. DOI: 10.1116/1.588613.

[79] SG Rykovanov et al. "Plasma surface dynamics and smoothing in the relativistic few-cycle regime". In: *New Journal of Physics* 13.2 (2011), p. 023008.

[80] B. Dromey et al. "Diffraction-limited performance and focusing of high harmonics from relativistic plasmas". In: *Nature Physics* 5 (2009), pp. 146–152.

[81] Valeriy V. Yashchuk et al. "Surface roughness of stainless-steel mirrors for focusing soft x rays". In: *Appl. Opt.* 45.20 (2006), p. 4833.

[82] Valeriy V Yashchuk, Wayne R McKinney, and Peter Z Takacs. "Binary pseudorandom grating standard for calibration of surface profilometers". In: *Optical Engineering* 47.7 (2008), pp. 073602–073602.

[83] Samuel K Barber et al. "Binary pseudo-random gratings and arrays for calibration of modulation transfer functions of surface profilometers". In: *Nuclear Instruments and Methods in Physics Research Section A: Accelerators, Spectrometers, Detectors and Associated Equipment* 616.2 (2010), pp. 172–182.

[84] L. Nevot and P. Croce. "Characterization of surfaces by grazing X-ray reflection–application to the study of polishing of some silicate glasses."". In: *Revue de Physique Applique* 15 (1980), pp. 761–80.

[85] O. Kornilov, R. Wilcox, and O. Gessner. "Nanograting-based compact vacuum ultraviolet spectrometer and beam profiler for in situ characterization of high-order harmonic generation light sources". In: *Rev. Sci. Instrum.* 81 (2010), p. 063109.

[86] J. H. Easter et al. "High-order harmonic generation from solid targets with 2 mJ pulses". In: *Opt. Lett.* 35.19 (2010), p. 3186.

[87] Katsumi Midorikawa. "High-Order Harmonic Generation and Attosecond Science". In: *Japanese Journal of Applied Physics* 50.9 (2011), p. 0001.

[88] Eric D Daniel, C Denis Mee, and Mark H Clark. *Magnetic recording: the first 100 years*. John Wiley & Sons, 1999.

[89] Sony Electronics Inc. *LTO Ultrium 4: Specifications Sheet @ONLINE*. 2010. URL: https://pro.sony.com/bbsccms/assets/files/cat/datastorage/brochures/LTO4_Spec_Sheet.pdf.

[90] Sony Electronics Inc. *Sony LTO Data Media Storage Tapes @ONLINE*. 2010. URL: `http://pro.sony.com/bbsccms/assets/files/cat/datastorage/brochures/25723_LTO_Brochure_FRb_3.pdf`.

[91] Sony Electronics Inc. *LTO Ultrium 3: Specifications Sheet @ONLINE*. 2007. URL: `https://pro.sony.com/bbsccms/assets/files/cat/datastorage/brochures/LTO3_Spec_Sheet.pdf`.

[92] Sony Electronics Inc. *LTO Ultrium 5: Specifications Sheet @ONLINE*. 2010. URL: `https://pro.sony.com/bbsccms/assets/files/cat/datastorage/brochures/LTO5_Spec_Sheet.pdf`.

[93] André Spizzichino and Petr Beckmann. *The Scattering of Electromagnetic Waves from Rough Surfaces*. New York, Paris, 1963.

[94] Shalom Eliezer. *The interaction of high-power lasers with plasmas*. CRC Press, 2002.

[95] XY Wang and MC Downer. "Femtosecond time-resolved reflectivity of hydrodynamically expanding metal surfaces". In: *Optics letters* 17.20 (1992), pp. 1450–1452.

[96] Brian-Tinh V Vu, Otto L Landen, and Abraham Szoke. "Time-resolved backside optical probing of picosecond-laser-pulse-produced plasma in solid materials". In: *Physical Review E* 47.4 (1993), p. 2768.

[97] M Sparks et al. "Theory of electron-avalanche breakdown in solids". In: *Physical Review B* 24.6 (1981), p. 3519.

[98] B Rethfeld. "Unified model for the free-electron avalanche in laser-irradiated dielectrics". In: *Physical review letters* 92.18 (2004), p. 187401.

[99] G Doumy et al. "Complete characterization of a plasma mirror for the production of high-contrast ultraintense laser pulses". In: *Physical Review E* 69.2 (2004), p. 026402.

[100] B. Dromey et al. "The plasma mirror—A subpicosecond optical switch for ultrahigh power lasers". In: *Rev. Sci. Instrum.* 75 (2004), pp. 645–649.

[101] Anna Lévy et al. "Double plasma mirror for ultrahigh temporal contrast ultraintense laser pulses". In: *Optics letters* 32.3 (2007), pp. 310–312.

[102] Andreas Henig et al. "Radiation-pressure acceleration of ion beams driven by circularly polarized laser pulses". In: *Physical Review Letters* 103.24 (2009), p. 245003.

[103] C Rödel et al. "High repetition rate plasma mirror for temporal contrast enhancement of terawatt femtosecond laser pulses by three orders of magnitude". In: *Applied Physics B* 103.2 (2011), pp. 295–302.

[104] S. Steinke. Private Communications. 2013.